

**Kinetics of Phase Separation and Thin Film  
Formation of Multiresponsive Polymers**

**Dissertation**

Zur Erlangung des akademischen Grades doctor rerum naturalium

(Dr. rer. nat)

vorgelegt dem Rat der Chemisch-Geowissenschaftlichen Fakultät der  
Friedrich-Schiller Universität Jena

von M.Sc. Aziz Ben-Miled

geboren am 09.07.1991 in Hammam Lif/Tunesien

Gutachter:

1. Prof. Dr. Lothar Wondraczek, Otto Schott Institute for Materials Research
2. Prof. Dr. Felix Schacher, Institute for Organic Chemistry and Macromolecular Chemistry

Tag der Verteidigung: 31.08.2022

*“Le désordre est simplement l’ordre que nous ne cherchons pas.”*

Henri Bergson, French philosopher

*I dedicate this manuscript to my parents,*

*my late grandmother (19.01.2022)*

*∞*

*my little brother*

# Acknowledgements

First of all, I would like to thank Prof. Dr. Lothar Wondraczek for giving me the chance to carry out my PhD thesis under the scope of the ERC project "UTOPES" in the historical university of Jena. I thank him again for the trust and autonomy he granted me in the last three years and five months, in addition to the logistical support and interesting discussions in the fascinating field of glasses.

Second, I would also like to express my gratitude towards Dr. Katrin Wondraczek for her time and for the fruitful exchanges that we had relative to the experimental work and revision of my scientific written contributions. A special thanks to Prof. Dr. Felix H. Schacher and his former PhD candidates Dr. Oliver Grimm and Dr. Afshine Nabyian for their collaboration and their generosity when it comes to materials supply.

Third, I am grateful to Dr. Ute Böttger and Mrs. Janett Grosser for facilitating the administrative paperwork before and during my stay in Jena. I am also thankful to Mrs. Nadja Buchert for her technical help and for ensuring a good dose of enthusiasm among people working in the CEEC building.

I cannot write an acknowledgment without mentioning my colleagues and friends who shared the doctoral adventure with me. Thank you Vahid, Guilherme, Ayda, Paulina, Bruno, Aaron, Ferdinand, Michael and Thien for all the joyful moments that we spent together. Our one-beer events and international dinners were always an occasion for me to learn about new cultures and to feel a part of a big family. I also had a good time as a tutor of inorganic and general chemistry with Dr. René Limbach. It was a good opportunity for me to be part of a teaching team and to see the students doing their experimental work in good conditions. Special thanks go to Roman Sajzew for reviewing the German version of the final summary of this manuscript.

Finally, I would like to thank my family for their support and patience during my university studies. I owe everything to my parents for motivating me to pursue a scientific career despite being born in a sports-oriented family. I also thank my friends in France, Germany and the Czech Republic for being always encouraging and keeping me updated about life outside the university.

## Abstract

Glasses constitute a class of materials characterized by non-crystalline microstructure and absence of long range order. Despite their local disorder, glasses show striking homogeneity over intermediate and longer distances. This feature provides glasses with an optical transparency which makes them good candidates for many cutting-edge applications in energy, life sciences and telecommunication.

Traditional glasses (inorganic non-metallic oxide glasses) are also characterized by mid-range structural heterogeneities and low atomic packing density. Together these properties are believed to reduce the strength of glasses due to brittle fracture behavior.

Thus, a challenge in the glass industry is currently working on circumventing this limiting mechanical property through an in-depth understanding of structural evolution and thermo-kinetic investigation of new types of glasses synthesized via novel deposition methods.

This thesis was dedicated to investigating the isothermal deposition of soft layers from liquid phase under near-ambient temperature conditions by way of substitution to the traditional melt-quenching method.

The main studied materials in this work are colloidal suspensions based on stimuli-responsive polymer particles. These materials were chosen for three considerations.

- First, their glass forming properties at low temperatures compared to conventional silicate glasses (generally produced at  $T > 1000^\circ\text{C}$ )
- Second, the possibility of controlling their interaction with solvent by external stimuli (temperature, pH, light or combination thereof)
- Third, their deformability. The deformation of soft particles opens the way to studying the effect of high particle volume fraction on the elastic properties of glassy thin films formed at constant temperature.

Thermoresponsive polymers are an emergent class of soft materials which form colloidal suspensions when polymer particles are dispersed in liquid.

Poly(triethylenglycol monomethyl methacrylate) P(TEGA) and poly(N-isopropylacrylamide) P(NIPAAm) are two thermoresponsive polymers belonging to the polyacrylate and polyamide polymer groups, respectively.

Despite their different chemical structures, both polymers show hydrophilic character in water at room temperature but turn hydrophobic when the temperature increases toward their lower critical solubility temperature (LCST). Due to their amphiphilic character, it is possible to control their particle packing density when deposited on a surface, as the interactions between the particles and the solvent are temperature-adjustable.

However, the deposition kinetics of these films seen from a glass perspective and the concomitant effect of stimuli (temperature and light) on their structural complexity using high-frequency spectroscopy methods have not been yet addressed in the literature.

In this thesis, we are interested in studying the deposition of layers formed by stimuli-responsive colloidal soft particles using a surface acoustic wave method: “Quartz Crystal Microbalance with Dissipation Monitoring, (QCM-D)”.

Chapter 1 gives an introduction to the structural properties of polymers and glasses in solution and at interfaces.

Chapter 2 presents the principles of the QCM-D monitoring technique in terms of the physical meaning of its main output (the normalized resonance frequency shift  $\Delta f_n/n$  and dissipation factor shift  $\Delta D_n$ ) and important parameters to consider while carrying out our study (temperature and light control).

Chapter 3 is dedicated to deposition control of soft layers formed out of dual stimuli-responsive colloidal particles of Poly (triethylene glycol acrylate-co-Spiropyran acrylate) (P(TEGA-co-SPA)). In this chapter, we examine the concomitant effect of light and temperature in order to manipulate the formation process of soft glassy films and their subsequent structural response.

Chapter 4 presents the kinetics of the deposition of Poly(N-isopropylacrylamide) P(NIPAAm) soft glassy layers. In this chapter, we focus on the effect of temperature and concentration on the isothermal glass formation below and above the phase separation temperature using a two-step kinetic model. We also provide a subsequent analysis of the viscoelastic properties of the deposited layers in non-isothermal mode and compare it with their properties in isothermal mode.

Chapter 5 gives a summary of this manuscript and perspectives for subsequent research work.



# Table of contents

ACKNOWLEDGEMENTS .....	I
ABSTRACT .....	II
TABLE OF CONTENTS .....	V
LIST OF ABBREVIATIONS AND SYMBOLS.....	VIII
LIST OF FIGURES.....	XIV
LIST OF TABLES .....	XX
1. INTRODUCTION.....	1
<b>1.1 Polymers.....</b>	<b>1</b>
1.1.1 Basics of polymer chemistry.....	1
1.1.2 Polymers in solution .....	2
1.1.3 Polymer interfaces .....	10
<b>1.2 Glasses .....</b>	<b>13</b>
1.2.1 Basics of glass chemistry .....	13
1.2.2 Fragility of glass formers .....	15
1.2.3 Colloidal glasses .....	18
1.2.4 Glass interfaces .....	21
2. FUNDAMENTALS .....	23
<b>2.1 Quartz Crystal Microbalance with Dissipation monitoring (QCM-D).....</b>	<b>23</b>
2.1.1 Overview.....	23
2.1.2 Quartz Crystal.....	24
2.1.3 Impedance analysis and ring down .....	25
2.1.4 Rigid and soft thin films .....	28
2.1.5 Temperature.....	30
2.1.6 Light.....	31

<b>2.2 Dynamic Light Scattering (DLS)</b> .....	<b>32</b>
2.2.1 Overview.....	32
2.2.2 DLS instrument.....	32
2.2.3 Brownian motion .....	32
2.2.4 The dynamic light scattering principle.....	33
2.2.5 Data analysis.....	34
<b>3. DEPOSITION STUDY OF DUAL LIGHT- AND TEMPERATURE-RESPONSIVE SOFT LAYERS</b> .....	<b>36</b>
<b>3.1 Summary</b> .....	<b>36</b>
<b>3.2 Introduction</b> .....	<b>36</b>
<b>3.3 Materials and Methods</b> .....	<b>38</b>
3.3.1 Copolymer synthesis.....	38
3.3.2 Dynamic Light Scattering DLS.....	41
3.3.3 QCM-D .....	41
<b>3.4 Results and Discussions</b> .....	<b>44</b>
3.4.1 Phase Separation of P(TEGA-co-SPA) in Dilute Aqueous Solution .....	44
3.4.2 Effect of UV-Irradiation on the Hydration of P (TEGA-co-SPA) Films below and above the LCST.....	45
3.4.3 Dual Temperature and Light Effect on the Build-Up of P (TEGA-Co-SPA) Layers on Silica Surfaces..	49
<b>3.5 Conclusion</b> .....	<b>57</b>
<b>4. KINETIC STUDY OF POLY(N-ISOPROPYLACRYLAMIDE) GLASSY LAYERS</b> .....	<b>58</b>
<b>4.1 Summary</b> .....	<b>58</b>
<b>4.2 Introduction</b> .....	<b>59</b>
<b>4.3 Materials and Methods</b> .....	<b>62</b>
4.3.1 Materials .....	62
4.3.2 X-Ray Diffraction .....	62
4.3.3 Differential Scanning Calorimetry.....	63
4.3.4 Dynamic Light Scattering .....	63
4.3.5 QCM-D Experiment .....	63
<b>4.4 Results and discussions</b> .....	<b>64</b>
4.4.1 P(NIPAAm) characterization in powder and in solution .....	64
4.4.2 Isothermal kinetic study of glassy wet layers on P(NIPAAm) on silica surface.....	67

## Table of contents

---

4.4.3 Two-Step Model Hypothesis .....	71
4.4.4 Variation of viscoelastic properties of P(NIPAAm) layers upon isothermal deposition.....	78
4.4.5 Non-isothermal kinetic study of glassy wet layers on P(NIPAAm) on silica surface.....	80
<b>4.5 Conclusion.....</b>	<b>83</b>
CONCLUSION OF THE MANUSCRIPT.....	85
ZUSAMMENFASSUNG DER ARBEIT .....	89
BIBLIOGRAPHY .....	94
SELBSTSTÄNDIGKEITSERKLÄRUNG .....	114
.....	114
CURRICULUM VITAE .....	115
LIST OF PUBLICATIONS AND POSTERS.....	116

## List of abbreviations and symbols

$\mathcal{D}$	Polydispersity index
$M_w$	Weight-average molar mass
$M_n$	Number-average molar mass
$X_w$	Weight-average degree of polymerization
$X_n$	Number-average degree of polymerization
ATRP	Atom Transfer Radical Polymerization
RAFT	Reversible Addition–Fragmentation Chain-Transfer
NMP	Nitroxide Mediated Polymerization
$T$	Temperature
$P$	Pressure
$\Delta G_{\text{mixture}}$	Gibbs free energy variation of polymer-solvent mixture
$\Delta H_{\text{mixture}}$	Enthalpy variation of polymer-solvent mixture
$\Delta S_{\text{mixture}}$	Entropy variation of polymer-solvent mixture
$k_b$	Boltzmann constant
$\chi$	Flory-Huggins parameter
$\varphi$	Volume fraction of monomers (chapter 1)
$1 - \varphi$	Volume fraction of solvent molecules (chapter 1)
$N$	Polymer chain length
$T_\theta$	Theta temperature
$T_{\text{DEM}}$	Demixion temperature

$T_{BP}$	Berghmans' point temperature
C	Polymer concentration
UCST	Upper Critical Solubility Temperature
LCST	Lower Critical Solubility Temperature
$T_g$	Glass transition temperature
P(NIPAAm)	Poly-(N-isopropylacrylamide)
P(iPMAAm)	Poly(N-isopropylmethacrylamide)
P(EAAm)	Poly(N-ethylacrylamide)
P(MEO2MA)	Poly[2-(2-methoxyethoxy)ethylmethacrylate]
P(OEGMA)	Poly (oligo ethylene glycol (meth-) acrylates)
$\varphi_c$	Volume fraction of monomers at the critical state (chapter 1)
$T_{cp}$	Cloud point temperature
P(TEGA)	Poly (triethylenglycol monomethyl methacrylate)
TEGA	2-(2-(2-methoxyethoxy) ethoxy) ethyl acrylate
SPA	Spiropyran acrylate
PEG	Polyethylene glycol
SAM	Self-Assembled Monolayer
PDMS	Poly(dimethylsiloxane)
SP	Spiropyran
MC	Merocyanine
$\lambda$	Wavelength (light or sound)
$V_{sp}$	Specific volume
$T_k$	Kauzmann temperature

$T_m$	Melting Temperature
$\eta$	Shear viscosity
$G_\infty$	High frequency shear modulus
$\tau$	Relaxation time
$E$	Effective activation energy
$T_0$	Finite temperature
$\eta_0$	Pre-exponential factor in Vogel-Fulcher-Tamman equation
$D$	Parameter indicating the deviation from Arrhenius law
$\varphi_{RCP}$	Random Close Packing fraction (chapter 1)
$\varphi_g$	Colloidal glass transition packing fraction (chapter 1)
$\beta$	Stretching exponent in Kohlrausch-Williams-Watt function
$t$	Time
$n$	Overtone order
$\Delta f_n$	Resonance frequency shift
$\Delta D_n$	Dissipation factor shift
$\Gamma$	Bandwidth
$f_n^*$	Complex resonance frequency
$f_n$	Resonance frequency (real part of $f_n^*$ )
$\Gamma_n$	Bandwidth (imaginary part of $f_n^*$ )
$\Delta f_n^*$	Complex resonance frequency shift
$\Delta \Gamma_n$	Bandwidth shift (imaginary part of $\Delta f_n^*$ )
$d_q$	Thickness of the quartz crystal
$d_f$	Thickness of film

$c_q$	Speed of the sound wave
$D_n$	Dissipation factor
FT	Fourier Transformation
$\frac{\Delta f_n}{n}$	Normalized resonance frequency shift
$\Delta D_n$	Dissipation factor shift
$m_f$	Areal mass
$f_1$	Fundamental frequency
$Z_q$	Acoustic impedance of the quartz
$\omega$	Angular speed
$Z_{liq}$	Acoustic impedance of the bulk liquid
$Z_{film}$	Acoustic impedance of the film
$\rho_{liq}$	Density of the bulk liquid
$\eta_{liq}$	Dynamic viscosity of the bulk liquid
$\rho_{film}$	Density of the film
$G_{film}$	Shear modulus of the film
$\delta$	Penetration depth
RMS	Root Mean Square (surface roughness)
UV-VIS	Ultra Violet-Visible (light)
DLS	Dynamic Light Scattering
$\theta$	Scattering angle in Chapter 2, Diffraction angle in Chapter 4
MSD	Mean Square Displacement
$D_t$	Transitional diffusion coefficient
$r_h$	Hydrodynamic radius

$G(\tau)$	Autocorrelation function
$I$	Scattered light intensity
$\tau_{lag}$	Lag time in DLS measurement
$A_{DLS}$	Baseline of the autocorrelation function
$B_{DLS}$	Intercept of the autocorrelation function
$\Gamma_{DLS}$	Decay constant related to the diffusion
$q$	Bragg Wave Vector
$n_{refr}$	Refractive index of the solvent
$\lambda_{beam}$	Wavelength of the incident light beam
$g_1$	Sum of exponential decays in $G(\tau)$
NNLS	Non-Negative Least Squares
CONTIN	Constrained Regularization Method for Inverting Data
SPR	Surface Plasmon Resonance
PolyDADMAC	Poly (diallyl dimethyl ammonium chloride)
PAH	Poly (allyl amine hydro-chloride)
PSS	Poly (styrene sulfonate)
PLL	Poly-(L-lysine)
SDS	Sodium Dodecyl Sulfate
DLS	Dynamic Light Scattering
PAAc	Poly(acrylic acid) PAAc
VPT	Volume Phase Transition
$D_2O$	Deuterated water
XPCS	X-ray photon correlation spectroscopy



iCVD	Initiated Chemical Vapor Deposition
XRD	X-Ray Diffraction
DSC	Dynamic Scanning Calorimetry
$\varphi$	Film formation progress (chapter 4)
$\varphi_1$	Fraction of particles forming the intermediate phase
$\varphi_{\text{coils}}$	Fraction of polymer coils on the surface
$\tau_1$	Diffusion time scale associated with the first process
$\tau_2$	Diffusion time scale associated with the second process
$\tau_{\text{off}}$	Characteristic time related to viscoelastic relaxation of polymer

## List of Figures

- Figure 1.1 The lattice model in two dimensions. Grey circles represent solvent molecules, and black circles represent monomers forming polymer chains.....2
- Figure 1.2 Phase diagrams for polymer-solvent mixtures showing either (a) UCST or (b) LCST type II phase separation.  $T_{dem}$  is the demixing temperature.  $T_{\theta}$  is the theta temperature and TBP corresponding to Berghmans' point at which there is intersection of the glass transition curve with the coexistence curve.  $T_g$  is the glass transition temperature of polymers. Reprinted by permission from Ref<sup>30</sup> : Springer Nature, Non-ionic Thermoresponsive Polymers in Water by V. Aseyev, H. Tenhu, F.M. Winnik, Copyright (2010).....4
- Figure 1.3 Coil to globule transition of a thermo-responsive polymer in aqueous solution. Reprinted from Ref<sup>16</sup> with permission from Elsevier.....6
- Figure 1.4 Chemical structure of thermosensitive monomers used to synthesize Poly(N-isopropylacrylamide) P(NIPAAm) (a) and Poly (triethylglycol monomethyl methacrylate) (PTEGA) (b).....7
- Figure 1.5 Photoswitching between the Spiropyran (SP) (a) and Merocyanine (MC) form (b).....12
- Figure 1.6 Schematic phase diagram of a glass former in the vicinity of the glass transition. The specific volume VSP is shown at constant pressure as a function of temperature. Depending on the cooling rate, the cooling of the glass former below its melting temperature  $T_m$  can lead to a crystalline or supercooled state. Below  $T_{g1}$  and  $T_{g2}$ , the supercooled liquid is in the glassy state (glass 1 and glass 2). Reprinted with permission from Ref<sup>85</sup>. Copyright 1996, American Chemical Society.....14

Figure 1.7 Angell-plot ( $T_g$ -scaled Arrhenius representation of liquid viscosities) where  $T_g$  value is associated with a viscosity  $\sim 10^{13}$  Poise. p, strong glass formers are characterized by a straight line while fragile glass formers are characterized by deviation from linearity. Insert shows pattern generated by modified Vogel-Fulcher equation with variations of parameter D only. Reprinted from Journal of Physics and Chemistry of Solids Vol 49, No. 8, pp 863-871, Copyright (1988), with permission from Elsevier.....17

Figure 1.8 Density autocorrelation functions as a function of log (time) of simple liquid exhibiting a simple exponential decay (a) and supercooled liquid with multi-steps decay (b). The  $\beta$ -relaxation decay represents the short-time relaxation processes in a cage, while the  $\alpha$ -relaxation decay time represents the diffusion of the molecules out of the cage for long time. Reprinted and adapted from Reichman, D. R. and Charbonneau, P. J. Stat. Mech. 2005, P05013. © IOP Publishing Ltd and SISSA Medialab srl. Reproduced by permission of IOP Publishing. All rights reserved.....20

Figure 2.1 Schematic representation of electrode patterns from the front (a) and from the back (b). Outer circles correspond to the quartz crystal size. The yellow filled area is the evaporated gold electrode. The front electrode is exposed to the sample. The back electrode is smaller than the front electrode to ensure the confinement of oscillations to the central region of the crystal. The quartz crystal has two electrode connections to electronics: the top connects to back electrode and the bottom to front electrode.....24

Figure 2.2 Impedance analysis based on the electrical conductance curves. The blue curve represents the resonance peak of an unloaded quartz crystal while the green curve represents the resonance peak of a loaded quartz crystal.  $\Gamma$  represents the bandwidth (half width at half height of the resonance peak) and  $\Delta f$  the resonance frequency shift which is the difference between the resonance frequency of the loaded and the unloaded quartz crystals. Reproduced/Adapted from reference<sup>143</sup> with permission from the PCCP Owner Societies.....25

Figure 2.3 Ring down of voltage oscillation in the time domain. This signal can result from Fourier transform of the acquired data in the frequency domain. The main extracted parameter is the dissipation factor  $D_n$ . Reproduced/Adapted from reference<sup>143</sup> with permission with permission from the PCCP Owner Societies.....27

Figure 3.1 Synthetic route for 2-(3',3'-Dimethyl-6-nitrospiro[chromene-2,2'-indolin]-1'-yl) ethyl Acrylate (SPA).....39

Figure 3.2 QCM-D temperature water sweep background used as a calibration curve to be subtracted from the data obtained in the presence of the dissolved copolymer to correct temperature dependency on the system for frequency shift (a) and dissipation shift (b).....42

Figure 3.3 Effect of UV LED illumination at 20°C on bare silicon coated quartz crystal (a) and on the same quartz crystal totally wet with a water layer (b).....43

Figure 3.4 Hydrodynamic radius of a P(TEGA-co-SPA) copolymer in aqueous solution upon heating as determined from DLS measurements.....44

Figure 3.5 Photos taken by a normal camera of the experimental set-up where the P (TEGA-co-SPA) solution is flowing on the SiO<sub>2</sub> sensor and UV light is applied through the QCM window module (top) Effect of illumination on the P(TEGA-co-SPA) liquid film color (bottom)..... 45

Figure 3.6 Variation of  $\Delta f_3/3$  (a) and  $\Delta D_3$  (b) versus time of P(TEGA-co-SPA) at the silica-water interface at a constant temperature..... 46

- Figure 3.7 Variation of  $\Delta f_3/3$  (a) and  $\Delta D_3$  (b) versus time of P(TEGA-co-SPA) at the silica-water interface at 19 and 35°C. This figure is a zoom at  $\Delta f_3/3$  in the range of 19 °C to 35 °C shown in Figure 3.6.....47
- Figure 3.8 Effect of continuous visible and UV light irradiation on the resonance frequency shift  $\Delta f_3/3$  (a,b) and dissipation shift  $\Delta D_3$  (c,d) on the copolymer liquid film at 19 and 50°C, respectively. Blue curves: continuous visible illumination for 25 min then UV-light switching, black curves: continuous visible illumination during the whole experiment.....48
- Figure 3.9 Variation of normalized  $\Delta f_3/3$  as a function of temperature upon irradiation of P(TEGA-co-SPA) copolymers at the silica –water interface, the copolymer was introduced at T=20°C (a), variation of  $\Delta f_3/3$  as a function of temperature of the same solution. Blue curves, upon illumination with visible light (b). The labels (I-III) mark the regimes of adsorption and film response discussed in the text.....50
- Figure 3.10 Variation of  $\Delta D_3$  as a function of  $-\Delta f_3/3$  when the sensor is continuously exposed to visible light (a), (b) variation of  $\Delta D_3$  as a function of  $-\Delta f_3/3$  when the sensor is irradiated with UV light (b). Blue curves: upon UV illumination, black curves: upon visible illumination.....53
- Figure 3.11 Schematic description of dual-responsive copolymer behavior of P(TEGA-co-SP/MC) at the silica-water interface during in-situ observation of adsorption with QCM-D. Four possible states can be obtained under the effect of switching from visible light illumination to UV light illumination below LCST (top side) and above LCST (bottom side) .....56
- Figure 4.1 XRD diffractogram of P(NIPAAm) powder at room temperature (a). DSC curve of P(NIPAAm) powder of heating scan between 100 °C and 370 °C at 1K/min (b). DLS measurement of 0.04 wt% P(NIPAAm) aqueous solution during temperature increase between 20 °C and 65 °C (c).....65

Figure 4.2 Evolution of the negative frequency shift as a function of time upon injecting P(NIPAAm) aqueous solution on SiO<sub>2</sub> surface.....68

Figure 4.3 Normalization of the polymeric film formation progress  $\phi$  as a function of time for different temperatures below and above the critical transition temperature (a). Plot of the extracted observed time as a function of time (b).....69

Figure 4.4 Normalized evolution of P(NIPAAm) film formation progress as a function of time at 30 °C as observed during isothermal formation of P(NIPAAm) film. Black: Normalized QCM-data, see text for details. Colored lines: KWW fit curves using different values for  $\beta$  (a). Fit of normalized data at 30°C according to two-step kinetic model. Black: Normalized data. Colored lines: fractions of polymer species during the film formation process as given by equation 4.3 (b).....70

Figure 4.5 Arrhenius plot of characteristic transformation times extracted from the two-step model at 0.04 wt% P(NIPAAm) aqueous solution (a), at 0.0004 wt% P(NIPAAm) aqueous solution..... 73

Figure 4.6 Quality fit of KWW equation applied to P(NIPAAm) film formation normalized data as a function of temperature at three different concentrations: at 0.04 wt% P(NIPAAm) aqueous solution (a) at 0.009 wt% P(NIPAAm) aqueous solution (b) at 0.004 wt% P(NIPAAm) aqueous solution (c).....76

Figure 4.7 The evolution of the negative frequency shifts as a function of time upon injection 0.04wt% P(NIPAAm) aqueous solution on SiO<sub>2</sub> surface. Data from third -, fifth- and seventh – order harmonics are included and are scaled according to equation 2 for direct comp comparison at different isothermal conditions below LCST (a), at LCST (b) and above LCST (c). Dissipation changes were plotted against the negative frequency shift for the same polymer solution below, during and above LCST (d).....79

Figure 4.8 Non-isothermal scan of P(NIPAAm) flowing solution of 0.04wt% on silica surface at 0.05K/min heating and 0.05K/mn cooling (a), negative frequency shifts as a function of temperature as different cooling rates as indicated (b), normalization upon cooling the solution between 39 and the dissolution temperature (inflection point) at different scanning rates (c). The investigated solution is 0.04 wt% P(NIPAAm) in water.....82

Figure 4.9 Construction of a non-isothermal heating scan at an imaginary heating rate 0 K/min. The data points of the resonance frequency and dissipation shifts were retrieved at 200s from P(NIPAAm) isotherms at the previously studied temperatures and overtone (a), Non-isothermal scan of P(NIPAAm) flowing solution of 0.04wt% on silica surface at heating rate 0.05 K/mn (b). In this figure the resonance frequency and dissipation shifts at different overtones are represented.....83

## List of Tables

Table 3.1 Fit parameters for the temperature correction as indicated in Figure 3.2.....	43
Table 4.1 Comparison between the size dependence reported in literature of mesoglobules with heating rate, temperature, concentration and our own results of P(NIPAAm) aqueous solutions measured with DLS.....	66
Table 4.2 Comparison between different relaxation times extracted from the normalized and modeled data at (0.04 wt% and 0.0004 wt%).....	74



# 1. Introduction

## 1.1 Polymers

### 1.1.1 Basics of polymer chemistry

A polymer is a chemical compound consisting of many individual repeating units called “monomers”. Polymers can be classified according to the number of basic monomers. However, it is important that at least one type of monomer builds up the chain.

Homopolymers are formed when the chain results from the polymerization of one type of monomer (e.g., polyethylene, polypropylene, polyvinyl chloride, polycaprolactam) whilst copolymers are made up of two or more monomers.

Prominent examples of copolymers are polyesters, polyurethanes and some polyamides. Polymers can be described by their molecular mass distribution or degree of polymerization using the “polydispersity index”  $\bar{D}$ .<sup>1</sup>

This polydispersity index can be estimated using the ratio of  $M_w$  (the weight-average molar mass) to  $M_n$  (the number-average molar mass). It can also be calculated according to degree of polymerization using the ratio of  $X_w$  (the weight-average degree of polymerization) to  $X_n$  (the number-average degree of polymerization).

Most polymerization techniques result in chains with a very broad distribution of molecular masses and  $\bar{D} > 1$ . Obtaining narrower distributions of molecular masses is made possible by special polymerization techniques such as anionic polymerization<sup>2</sup> as well as the following controlled radical polymerization methodologies:

- Atom Transfer Radical Polymerization (ATRP)<sup>3</sup>
- Reversible Addition–Fragmentation chain-Transfer (RAFT) Polymerization<sup>4</sup>
- Nitroxide Mediated Polymerization (NMP)<sup>5</sup>

In general, the chemical structure, polarity and molecular mass affect the dissolution of polymers in a solvent. Thus, knowing the chemistry of polymers is very important to predict their behavior in solution; particularly for applications relevant to industry.

## 1.1.2 Polymers in solution

### 1.1.2.1 Flory-Huggins Theory

Polymer chains adopt different conformations when they are in contact with solvent molecules. The simplest conformation is when polymers are constituted of monomers in a random walk without interactions between each other. In this case, polymer chains are called “ideal chains”, in contrast to “real chains” where monomers interact due to the excluded volume effect.

This excluded volume effect causes polymers to adopt a coil conformation. In addition to monomer-monomer interactions, polymer conformation in solution also depends on monomer-solvent and solvent-solvent interactions. These interaction effects are generally described in the framework of Flory-Huggins theory using the lattice model to arrange the polymers and solvents.<sup>6,7</sup>

Figure 1.1 shows a two dimensional version of this model where the black circles represent the monomers forming polymer chains and the grey circles represent the solvent molecules. The mixing of a polymer in a solvent at constant temperature  $T$  and external pressure  $P$  results in variation of the Gibbs free energy according to equation (1.1)

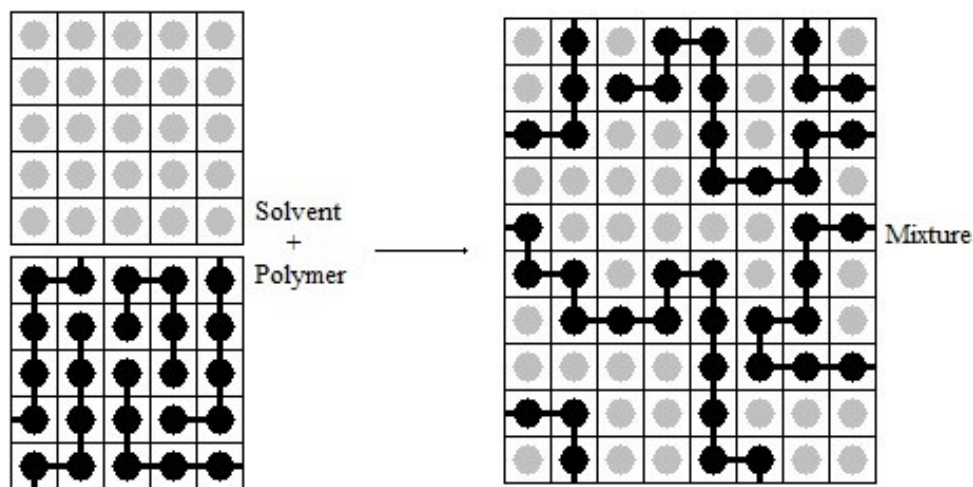


Figure 1.1 The lattice model in two dimensions. Grey circles represent solvent molecules, and black circles represent monomers forming polymer chains.

$$\Delta G_{\text{mixture}} = \Delta H_{\text{mixture}} - T\Delta S_{\text{mixture}} \quad (1.1)$$

The mixture (polymer-solvent) is only possible when  $\Delta G_{\text{mixture}}$  is negative. This implies that either the enthalpy of mixing  $\Delta H_{\text{mixture}}$  decreases by dissolution or the product of the temperature and the entropy of mixing  $T\Delta S_{\text{mixture}}$  is higher than  $\Delta H_{\text{mixture}}$ . In order to determine the Gibbs free energy based on statistical thermodynamics, Flory derived  $\Delta G_{\text{mixture}}$  for a non-ideal polymer solution assuming the same molar volume for monomers and solvent molecules inside a lattice according to equation (1.2)

$$\Delta G_{\text{mixture}} = k_b T \chi \varphi (1 - \varphi) + k_b T \left( \frac{\varphi}{N} \ln(\varphi) + (1 - \varphi) \ln(1 - \varphi) \right) \quad (1.2)$$

Where  $k_b$  is the Boltzmann constant,  $T$  is temperature,  $\chi$  is the Flory-Huggins parameter,  $\varphi$  is the volume fraction of monomers occupying the lattice sites,  $1 - \varphi$  the volume fraction of solvent molecules occupying the lattice sites and  $N$  the number of monomers constituting the polymer chain.

We notice in equation (1.2) that the first term of the mixing entropy is divided by the chain length  $N$ . For polymer-solvent system,  $\Delta S_{\text{mixture}}$  is small when polymer chains are long ( $N \rightarrow \infty$ ). This indicates that the mixing entropy is determined mainly by the solvent molecules.

However, the mixing enthalpy is dependent on the Flory-Huggins parameter  $\chi$ . This parameter characterizes the interactions between neighboring molecules (monomer-monomer, solvent-solvent and monomer-solvent) upon mixing solvent and monomers inside the lattice.

When  $\chi$  is negative, polymer-solvent interactions are more favored and the solvent is considered a good solvent. A positive  $\chi$  reveals that monomer-solvent interaction is less favored compared with monomer-monomer and solvent-solvent interactions. This is the case of a poor solvent.

If a solvent is poor enough to suppress the excluded volume effect, the solution reaches the theta condition (meaning the polymer behaves as ideal chains in solution) with  $\chi = \frac{1}{2}$  at a characteristic temperature commonly called “theta temperature”  $T_\theta$ .

### 1.1.2.2 Phase Diagram

The change of the Flory-Huggins parameter from  $\chi < \frac{1}{2}$  to  $\chi > \frac{1}{2}$  upon temperature increase indicates in general the change of the solvent quality from good to poor in ideal solutions. Based on this

change and replacing  $\chi$  by temperature, we can draw the polymer-solvent phase diagram by representing the coexistence curve on a temperature-composition plane.

Figure 1.2 shows the two most common types of phase diagrams of polymer-solvent mixtures found in literature. In these diagrams the composition is expressed in polymer concentration  $c$  on the x-axis.

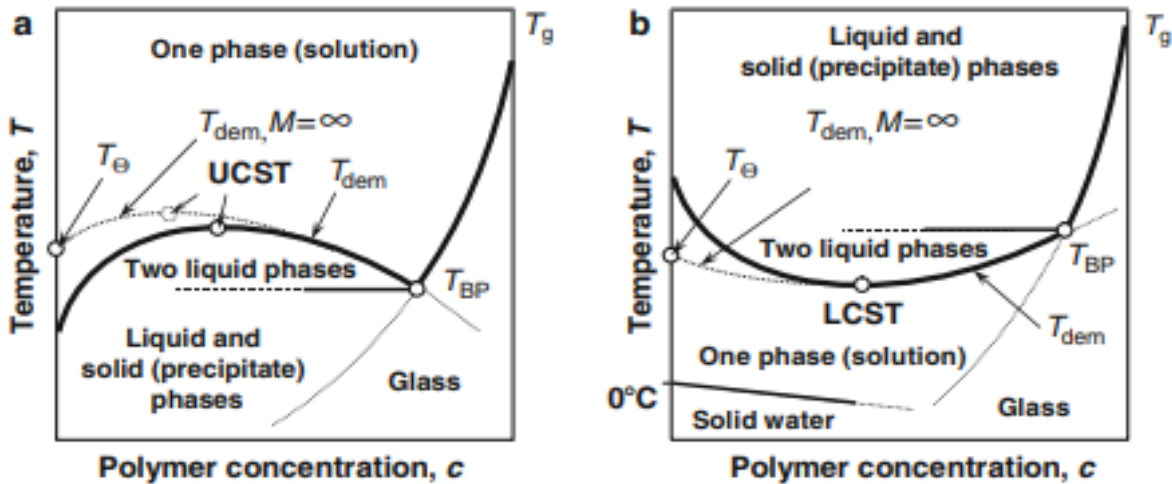


Figure 1.2 Phase diagrams for polymer-solvent mixtures showing either (a) UCST or (b) LCST type II phase separation.  $T_{dem}$  is the demixing temperature.  $T_{\theta}$  is the theta temperature and  $T_{BP}$  corresponding to Berghmans' point at which there is intersection of the glass transition curve with the coexistence curve.  $T_g$  is the glass transition temperature of polymers. Reprinted by permission from Ref<sup>29</sup> : Springer Nature, *Non-ionic Thermoresponsive Polymers in Water* by V. Aseyev, H. Tenhu, F.M. Winnik, Copyright (2010).

Some polymer-solvent mixtures reach the critical state at the upper point of their coexistence curve as depicted in Figure 1.2a. The critical temperature associated with this point is called Upper Critical Solubility Temperature (UCST): above this point, the polymer and solvent are miscible in all proportions. For other polymer-solvent mixtures, the critical temperature is situated at the lowest point of their coexistence curve as displayed in Figure 1.2b. This critical temperature is commonly known as Lower Critical Solubility Temperature (LCST).

When  $T < LCST$ , the polymer is totally miscible in solution but when  $T > LCST$ , the polymer-solvent mixture undergoes a phase separation into a polymer-poor phase and polymer-rich phase. Both

diagrams in Figure 1.2 manifest a possible formation of glass by the vitrification of polymer concentrated domains.<sup>8</sup>

Each polymer–solvent composition has its own glass transition temperature  $T_g$  that can be estimated by applying the modified Fox-Flory relation.<sup>9</sup> The intersection between the glass transition curve constructed from this relation with the coexistence curve corresponds to Berghmans' temperature  $T_{BP}$ . For polymer-solvent mixtures showing a phase diagram with UCST, when  $T < T_{BP}$ , there is a phase separation into a polymer-poor liquid and polymer-rich solid, whereas for  $T > T_{BP}$ , the mixture phase separates into two liquid phases as shown in the diagram in Figure 1.2a. For polymer-solvent mixtures showing LCST, the behavior is the inverse. Polymers which display miscibility gaps in their phase diagrams such as UCST and LCST are called temperature-responsive polymers or thermoresponsive polymers.

### *1.1.2.3 Thermoresponsive polymers in solution*

Thermoresponsive polymers are the most common stimuli-responsive polymers reported in literature. Thermoresponsive polymers demonstrate UCST or LCST in organic solvents and in water. For instance, polystyrene displays miscibility gaps in different solvents: an UCST in cyclohexane<sup>10</sup> and a LCST in butylacetate.<sup>11</sup>

The research in the field of thermoresponsive polymers has been extensively devoted to water-soluble polymers. The great interest in these materials ostensibly stems from their potential applications in the biomedical field such as drug delivery,<sup>12</sup> tissue engineering<sup>13</sup> and separation of proteins.<sup>14</sup>

Water-soluble polymers with a LCST are generally characterized by their coil to globule transition upon crossing the critical temperature. This transition originates from breakage of intermolecular and intramolecular hydrogen bonds between water molecules and polymer coils. Additionally, an increase in temperature changes the quality of the solvent (water) from good to poor solvent, leading to favorable hydrophobic interactions between polymer segments as shown in Figure 1.3 taken from reference.<sup>15</sup>

The LCST associated with the coil-to-globule transition depends not only on the temperature but on several other parameters including the concentration of polymer in solution and in some cases the molar mass.<sup>16</sup>

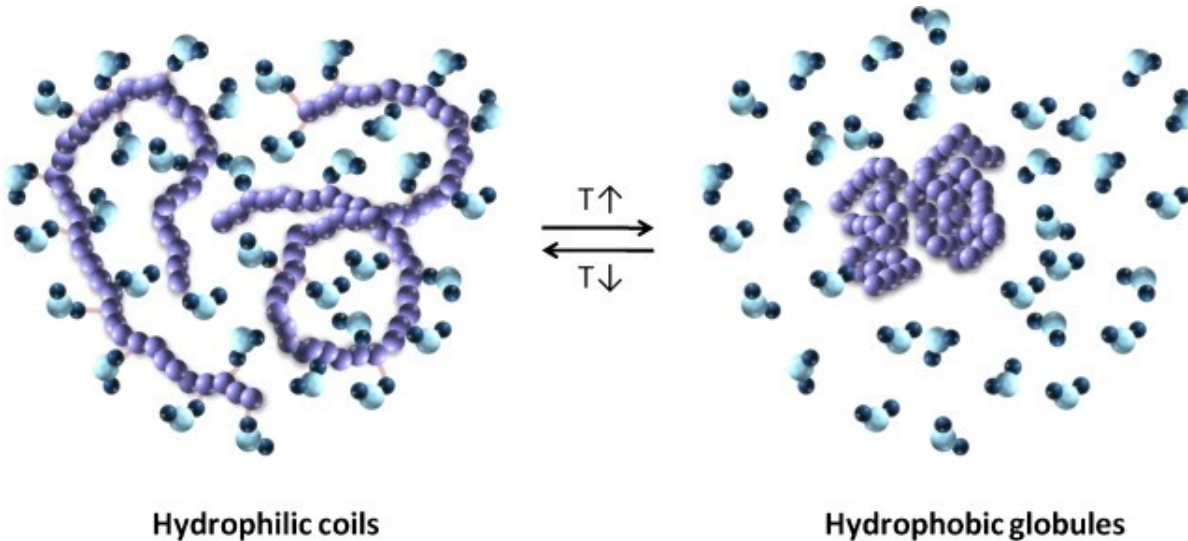


*Figure 1.3 Coil to globule transition of a thermo-responsive polymer in aqueous solution.*

*Reprinted from Ref<sup>15</sup>, with permission from Elsevier*

A classification of water-soluble thermoresponsive polymers based on their miscibility with water was proposed by Berghmans and Van Mele.<sup>17</sup>

In fact, there are Type I thermoresponsive polymers whose LCST follows the previously described Flory-Huggins theory. The LCST in this case shifts from its value, previously defined as the lowest point of the coexistence curve, when the molar mass of polymers tends to infinity and the concentration of polymer in solution tends to zero.

This dependence between the LCST value and molar mass has been observed for Poly(N-vinylcaprolactam)<sup>18</sup> PVCL and Poly (2-oxazoline) analogues.<sup>19</sup>

Conversely, Type II polymers hardly display any dependence between the LCST value and the length or architecture of the chain. Prominent examples of this polymer type are polyacrylamides

such as Poly-(N-isopropylacrylamide) P(NIPAAm),<sup>16</sup> Poly(N-isopropylmethacrylamide) P(iPMAAm),<sup>20</sup> Poly(N-ethylacrylamide) P(EAAm)<sup>21</sup> and Polyacrylates-based polymers such as Poly[2-(2-methoxyethoxy)ethylmethacrylate] P(MEO2MA)<sup>22</sup> and Poly(oligo ethylene glycol (meth-) acrylates) P(EOGMA).<sup>23</sup>

The experimental work in this thesis was dedicated to studying the solution and soft layer behavior of the thermoreponsive homopolymer (Poly-(N-isopropylacrylamide) and a dual temperature- and light-sensitive copolymer containing ethylene glycol (meth-) acrylate segments: Poly (triethylenglycol monomethyl methacrylate) PTEGA. A short insight about the state-of-the-art of these materials will be described in the following subsections.

### 1.1.2.3.1 Poly(N-isopropylacrylamide) P(NIPAAm)

Poly(N-isopropylacrylamide) P(NIPAAm) is the most commonly known thermoresponsive polymer in the research community. This polymer results from the polymerization of N-isopropylacrylamide (NIPAAm) represented on the left side of Figure 1.4.

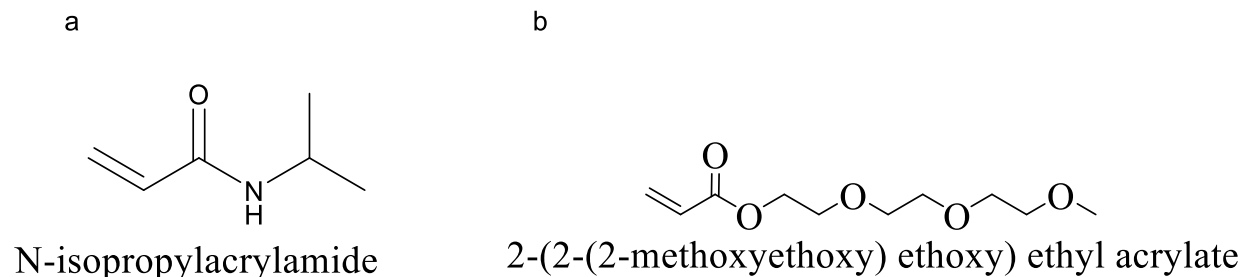


Figure 1.4 Chemical structure of thermosensitive monomers used to synthesize Poly(N-isopropylacrylamide) P(NIPAAm) (a) and Poly (triethylenglycol monomethyl methacrylate) (PTEGA) (b).

The LCST of this material is generally detected at  $T \sim 32^\circ\text{C}$  (referring to the 1968 article of Heskins and Guillet.<sup>24</sup>) At the time, the LCST was determined to be at  $T \sim 31^\circ\text{C}$  with a volume fraction of P(NIPAAm) monomers in the critical state  $\phi_c = 0.16$ .

This LCST value makes P(NIPAAm) a good candidate for drug delivery applications<sup>25</sup> as hydrosoluble drug molecules interacting with this material could be released at a temperature near that of the human body. The LCST of P(NIPAAm) can be tuned by copolymerizing the NIPAAm

monomer with a chosen co-monomer to affect the macromolecule's hydrophilicity/hydrophobicity. Thus, the drug release temperature can be tailored up to  $T \sim 37^\circ\text{C}$ .

Depending on the synthesis method, P(NIPAAm) displays different architectures including linear chains, microgels and macrogels. Several publications report that the LCST of P(NIPAAm) is affected by adding organic salts, surfactants or cosolvents.<sup>26-28</sup>

Raising an aqueous solution of P(NIPAAm) above the phase separation temperature (called the demixion temperature  $T_{\text{dem}}$  or the cloud point temperature  $T_{\text{cp}}$  depending on the experimental technique used) leads to a change in the optical properties of the solution (turbidity) due to the collapse of P(NIPAAm) chains and precipitation of the material due to phase separation.<sup>29</sup>

Experimentally,  $T_{\text{dem}}$  is generally determined using microcalorimetry while  $T_{\text{cp}}$  is detected by turbidity techniques such as UV-VIS spectroscopy. These techniques are also useful to investigate the kinetics of demixion and remixion processes of P(NIPAAm) in aqueous solution upon heating and cooling.<sup>17,30</sup> Interestingly, the demixion and remixion processes of this material are dependent on the heating and cooling rates, respectively. This kinetic dependence is expressed by a thermal hysteresis which is still debated and suggests a possible glass-like behavior of P(NIPAAm) in water.

### **1.1.2.3.2 Poly (triethylenglycol monomethyl methacrylate) P(TEGA)**

The oligo ethylene glycol (meth-)acrylates are non-linear polyethylene glycol (PEG) analogues composed of polymerizable monomers connected to short oligo(ethylene) glycol chains.<sup>31</sup> These monomers were first polymerized by Rempp<sup>32</sup> and his coworkers in 1982.

At the time, they were constituted of 2 to 10 repetition units of ethylene glycol in the side chain. Various novel macromolecular architectures based on these innovative materials were reported in the last years.<sup>33-35</sup> The incorporation of a hydrophobic co-monomer to oligo ethylene glycol (meth-) acrylates is a good way to precisely adjust the LCST of these materials between 26 and 90°C in aqueous solutions.<sup>36</sup>

Unlike the coil-to-globule transition of P(NIPAAm), which is controlled by intramolecular and intermolecular  $\text{NH}\dots\text{O}=\text{C}$  hydrogen bonding interactions, the ether oxygens of polyethylene glycol form stabilizing hydrogen bonds between oligo ethylene glycol (meth-)acrylate and water.<sup>31</sup>



Poly (triethylenglycol monomethyl methacrylate) PTEGA is a newly engineered form of oligo ethylene glycol (meth-)acrylate OEGMA and constituted of three repetition units of oligo ethylene glycol in the side chain also called 2-(2-(2-methoxyethoxy) ethoxy) ethyl acrylate (TEGA) as displayed on the right side of Figure 1.4.

PTEGA is generally characterized by an LCST above 50°C which is reported to have a lower LCST value compared to its linear counterpart.<sup>37</sup> Due to this relatively high LCST compared to LCST values of polyacrylamides in general and P(NIPAAm) in particular, it is possible to copolymerize triethylene glycol methacrylate (TEGA) monomer with a hydrophobic monomer in order to decrease its LCST.

Lowering the LCST of PTEGA should theoretically be convenient for biomedical applications. Consequently, PTEGA copolymers may combine the properties of both PEG and P(NIPAAm) in a single macromolecule.<sup>31</sup> Recently, the Schacher group (University of Jena, Germany) reported the synthesis of a dual light- and temperature-responsive copolymer based on the polymerization of TEGA monomers with a hydrophobic photochromic monomer, Spiropyran, linked to an acrylate group, SPA.<sup>38</sup> Both stimuli (temperature and light) can be applied to this material independently without interfering with each other due to the orthogonal synthesis of this copolymer via nitroxide-mediated polymerization.

The cloud point temperature of this material decreases from 65 °C (0% SPA) to 35 °C (16% SPA) with increasing amounts of incorporated SPA moieties. Based on these results, the P (TEGA-co-SPA) copolymer containing 12–14% SPA was chosen to be investigated under the scope of this thesis.

There are two reasons for this choice:

- First, the cloud point of the copolymer with this proportion of SPA is conveniently located within the optimal working temperature range of the instrument used in this thesis.
- Secondly, this temperature range is ideally suited for research in relevant applications such as biomedical and microfluidic research.

## 1.1.3 Polymer interfaces

### *1.1.3.1 Introduction to polymer coatings*

Polymer coating is an ideal surface modification of many solid substrates. They can be applied for many purposes such as anticorrosion protection,<sup>39</sup> lubrication (by reducing friction),<sup>40</sup> anti-fogging,<sup>41</sup> self-healing,<sup>42</sup> and self-cleaning properties.<sup>43</sup>

Deposition of surface coatings can either be based on chemical bonds or physical interaction.

In the first case, surface functionalization is achieved when polymers attach to a solid surface through a covalent bond. Prominent techniques based on covalently bonded polymers are polymer brushes<sup>44</sup> and self-assembled monolayers (SAMs).<sup>45</sup>

In the second case, the deposition is carried out from solution and generally the solvent evaporates during the process. The coating can be obtained via different available techniques such as spin coating, dip coating, blade coating, etc.<sup>46</sup> Other coating techniques based on physical interaction are Langmuir-Blodgett films,<sup>47</sup> layer-by-layer deposition<sup>48</sup> and physical adsorption of polymers.<sup>49</sup>

This latter technique is called "physisorption" and takes place as result of attractive physical forces between polymer segments and the surface.<sup>50</sup> Adsorbed polymer molecules have only part of their segments on the surface (called "trains"), while a considerable fraction of the segments extend into the solution.<sup>51</sup> The protruding parts are called "loops" with both ends in contact with the surface as well as "tails" at the end of the adsorbed molecule.

Generally speaking, physisorption of polymers from a bulk liquid onto a solid surface can be either reversible or irreversible.<sup>52</sup>

Physisorption from a solution is reversible when the polymer binds weakly to the surface and has only few conformational restrictions.

Irreversibility is usually achieved using hydrogen bonding or other dipolar forces, dispersive forces, or attraction between charged groups along the polymer backbone and the surface.<sup>53</sup> It typically occurs on metals, semiconductors, inorganic glasses, or sol-gel layers such as polydimethylsiloxane (PDMS) when surface oxygens of the substrate form strong hydrogen bonds with the polymer.<sup>52</sup>

Similarly, various macromolecules (polymers, proteins, DNA, etc.) are prone to adsorb strongly on oxide glass surfaces through hydrogen bonds or other physical forces (electrostatic attraction, hydrophobic interaction).<sup>54,55</sup>

### *1.1.3.2 Stimuli-responsive polymers at interfaces*

In order to tailor surface adhesion, stimuli-responsive polymers have attracted great attention in the last decades due to their ability to respond to external triggers. Layers formed from such polymers are expected to enable switchable surfaces which may change their properties in controllable and programmable ways.<sup>56</sup>

External stimuli include temperature,<sup>57</sup> light,<sup>58</sup> pH,<sup>59</sup> ionic strength,<sup>60</sup> or a combination thereof, which enables logic gate operations.<sup>61,62</sup> Thermo- and pH-sensitive polymers at interfaces are commonly used in the research community. This is most likely due to the temperature- and pH-adjustment methods which are more often than not low-energy and environmentally friendly.

However, scientific articles about light-responsive polymers at interfaces are rather scarce.

This is presumably due to commercial unavailability of photoresponsive monomers. Light is a remote trigger which has advantages compared to the aforementioned stimuli: contactless, easily dosed to tune the strength of the response, allows accurate temporal and spatial resolution of the response.<sup>63</sup> The most reported photochromic monomers are Spiropyran,<sup>64</sup> Azobenzene,<sup>65</sup> and Diarylethene.<sup>66</sup> These compounds are responsive to light irradiation through reversible or irreversible isomerization between two states of variable polarity. Isomerization reactions can be detected through observation of color changes due to photon absorption.

Spiropyran (SP) is a “spiro” compound, which means that it has at least two molecular rings linked with only one common atom. Its chemical structure consists of a heterocycle and a chromene moiety orthogonally linked with a carbon atom.

SP is one of the few chromophores that is not only photoswitchable but also responds to other stimuli such as temperature, solvent, metal ions, and pH.<sup>67</sup>

In response to UV light ( $\lambda = 365$  nm), the closed nonpolar and colorless Spiro form “SP” is transformed into the open, polar, colored and zwitterionic Merocyanine form ”MC”. Irradiation with visible light ( $\lambda = 550$  nm) causes ring closure and return to the initial state, (see the expected isomerization in Figure 1.5).

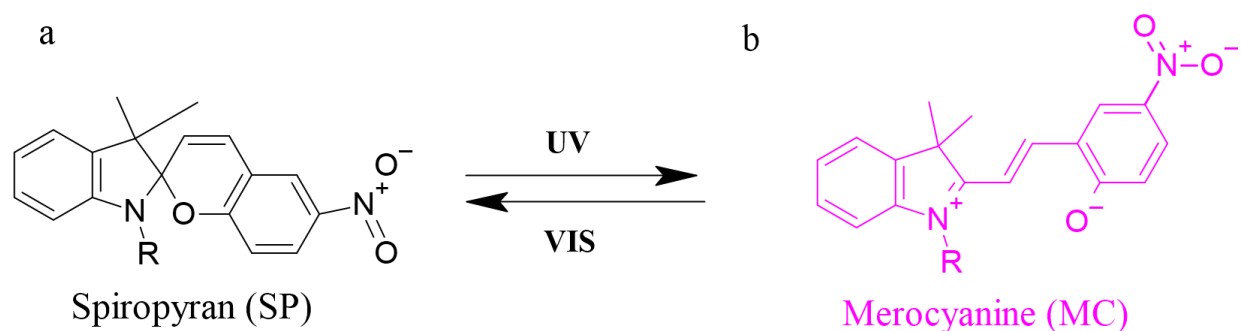


Figure 1.5 Photoswitching between the Spiropyran (SP)(a) and Merocyanine (MC) form (b).

Interestingly, Spiropyran is known to display the largest response in dipole moment due to the formation of Merocyanine, when compared to other photochromic molecules.<sup>68</sup> The UV-light induced reversible isomerization of SP between nonpolar and polar states can be used to tune interfacial properties such as wettability,<sup>69</sup> swelling properties<sup>70</sup> and color changes<sup>71</sup>, as the (UV-induced) polarity change affects the interaction between the polymer and the solid-liquid interface.

## 1.2 Glasses

### 1.2.1 Basics of glass chemistry

Glasses are non-equilibrium non-crystalline materials which are omnipresent in everyday applications such as packaging, housing, automotive, optical fibers, etc. The most common definition of glasses is the one given by Zachariasen, who defined them as extended three-dimensional networks lacking periodicity with an energy content comparable to that of the corresponding crystal.<sup>72</sup> Categories of glassy materials include inorganic glasses,<sup>73</sup> polymer glasses,<sup>74</sup> metallic glasses,<sup>75</sup> and recently hybrid organic-inorganic glasses.<sup>76</sup>

The best-known method for glass formation is fast cooling a viscous liquid (also called the melting-quenching method), other methods including physical vapor deposition,<sup>77</sup> hydrolysis of organic precursors followed by drying (sol-gel),<sup>78</sup> heavy ion bombardment of crystalline forms,<sup>79</sup> amorphization of porous materials<sup>80</sup> and recently 3D printing.<sup>81</sup>

It is not uncommon to confuse glasses with amorphous materials in literature due to the lack of a clear basis with which to distinguish between these two types of materials.<sup>82</sup> However, a structural basis can be agreed upon according to Zachariasen's concept of a topologically disordered network with uniform short range order.<sup>83</sup> Therefore, a glass is defined as a non-crystalline solid which shows structural relaxation upon heating to the liquid state and consequently shows a glass transition.

In contrast, an amorphous material can relax to another solid state, undergo a first order transition to the supercooled liquid state, or crystallize (as shown in Figure 1.6).

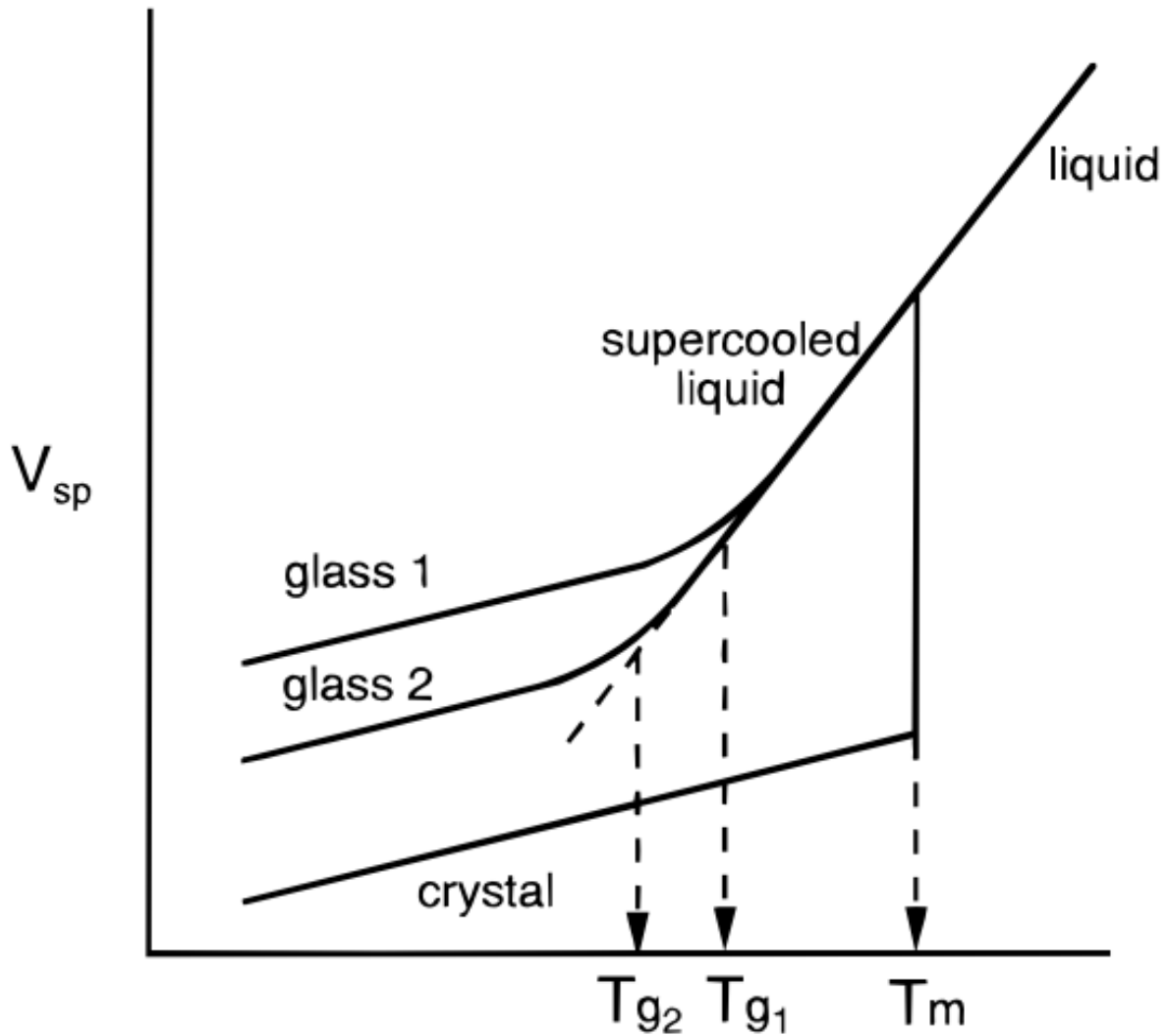


Figure 1.6 Schematic phase diagram of a glass former in the vicinity of the glass transition. The specific volume  $V_{SP}$  is shown at constant pressure as a function of temperature. Depending on the cooling rate, the cooling of the glass former below its melting temperature  $T_m$  can lead to a crystalline or supercooled state. Below  $T_{g1}$  and  $T_{g2}$ , the supercooled liquid is in the glassy state (glass 1 and glass 2). Reprinted with permission from Ref.<sup>85</sup> Copyright 1996, American Chemical Society.

The glass transition temperature  $T_g$  defines the point of intersection of the extrapolation of the specific volume  $V_{sp}$  in the glassy state with that of the supercooled liquid line, assuming infinitely small cooling rates.<sup>84</sup> It is worth noting that  $T_g$  is also defined as the temperature at which the viscosity is equal to  $10^{13}$  Poise (or  $10^{12}$  Pa.s).<sup>85</sup>

Kauzmann proposed that infinitely slow cooling would result in a vanishing entropy difference between the liquid and crystalline solid states at a finite temperature, called the Kauzmann temperature  $T_k$ .<sup>86</sup>

In contrast to the crystallization process, the transition from the supercooled liquid and the glassy state is not instantaneous due the slow dynamics of the supercooled liquid close to  $T_g$ .

From the dynamic point view, a “glassy” material is obtained when its typical relaxation time scale is of the same order or larger than the typical duration of an experiment or a numerical simulation.<sup>87</sup> The increase of relaxation time is generally coupled with an increase of the shear viscosity  $\eta$ .

Using basic hydrodynamic calculations, the shear viscosity of a liquid can be described by the product of the high frequency shear modulus,  $G_\infty$ (which does not noticeably vary for supercooled liquids) and the relaxation time,  $\tau$ , as shown by the Maxwell model expressed in equation (1.3)

$$\eta = G_\infty \times \tau \quad (1.3)$$

## 1.2.2 Fragility of glass formers

The increase of the relaxation time scale of supercooled liquids is notable because of its temperature dependence covers a timescale range of multiple orders of magnitude. This relaxation time-temperature dependence helps distinguish between two main types of glass formers. The first type is when the evolution of the structural relaxation time as a function of temperature follows an Arrhenius law according to equation (1.4)

$$\eta \propto \exp\left(\frac{E}{k_b \times T}\right) \quad (1.4)$$

where  $\eta$  is the viscosity,  $E$  is the effective activation energy (defined as the energy barrier required to break a chemical bond). In this case, the glass former is called “strong”.

The second type is when the relaxation time is characterized by a super-Arrhenius dependence as given in equation (1.5)

$$\eta \propto \exp\left(\frac{E}{k_b \times (T - T_0)}\right) \quad (1.5)$$

where  $T_0$  is a finite temperature. In this case, the glass former is called “fragile”.

Note that the terms “strong” and “fragile” are not correlated with the mechanical properties of the glass but were introduced in relation to the evolution of the short range order close to  $T_g$ .<sup>87</sup>

To classify supercooled liquids into strong and fragile glass formers, it is possible to plot the logarithm of the viscosity (or the relaxation time) as a function of  $\frac{T}{T_g}$  as in Figure 1.7. This is called the Angell plot.<sup>85</sup>

From a structural point of view, strong glass formers display a covalently bonded (e.g.  $\text{SiO}_2$ ) three-dimensional network structure whereas fragile glass formers typically consist of molecules interacting through nondirectional, noncovalent interactions such as dispersion forces, Van der Waals interactions (e.g. o-terphenyl).<sup>84</sup>



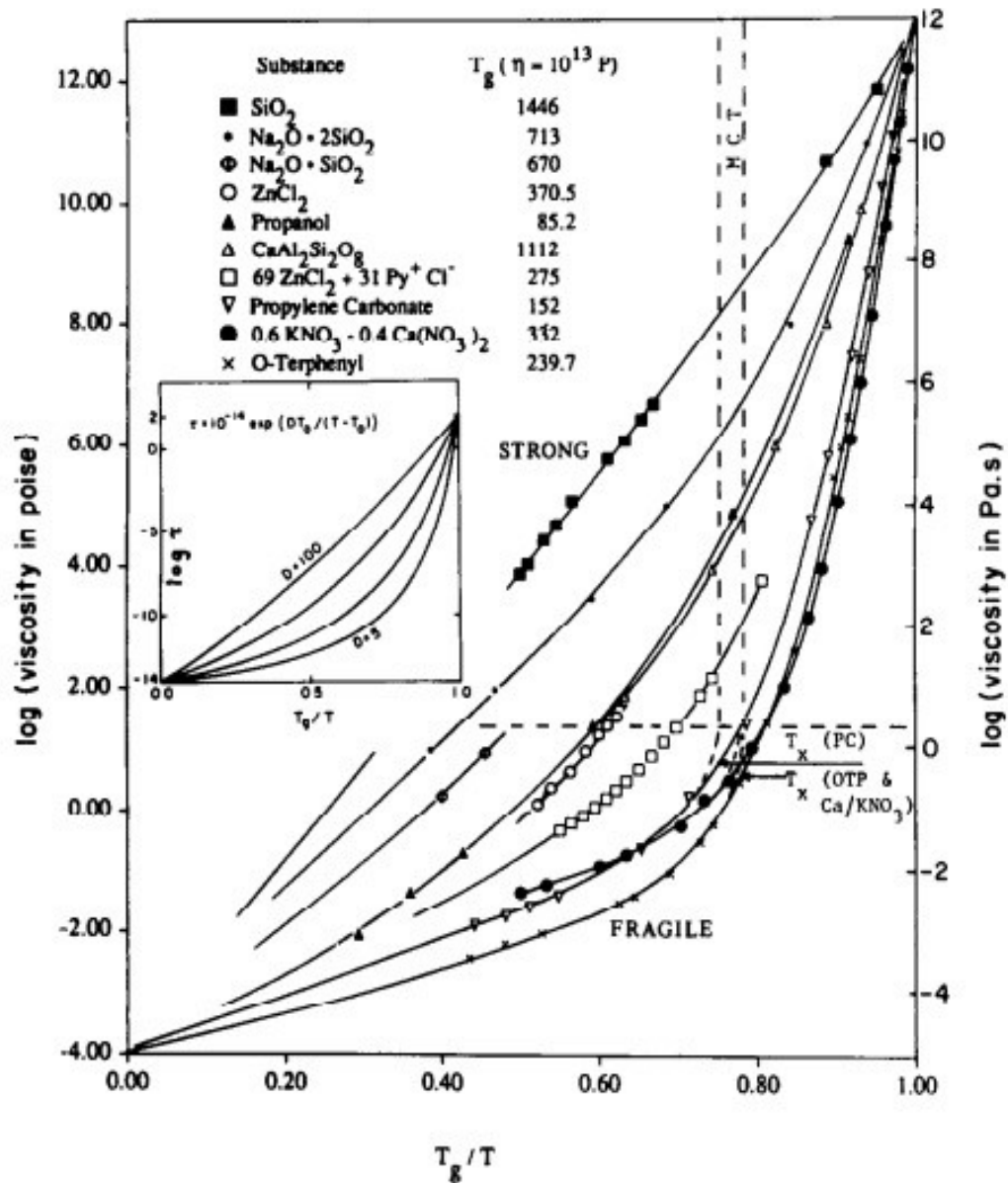


Figure 1.7 Angell-plot ( $T_g$ -scaled Arrhenius representation of liquid viscosities) where  $T_g$  value is associated with a viscosity of  $\sim 10^{13}$  Poise. In this illustration, strong glass formers are characterized by a straight line, while fragile glass formers are characterized by deviation from linearity. Insert shows the pattern generated by the modified Vogel-Fulcher equation with variations of parameter  $D$  only. Reprinted from *Journal of Physics and Chemistry of Solids* Vol 49, No. 8, pp 863-871, Copyright (1988), with permission from Elsevier.

Fragile glass formers are mostly polymeric materials and organic liquids and so they cannot be introduced into the Angell plot without taking into account the effect of their molecular mass distribution on their viscosity.<sup>85</sup> As displayed in Figure 1.7, fragile glass formers are characterized by a divergence of the logarithm of their viscosities (or relaxation times) upon increase of temperature towards  $T_g$ .

This divergence from linearity can be expressed by the Vogel-Fulcher-Tamman equation (VFT)

$$\eta \propto \eta_0 \exp^{DT_0/(T-T_0)} \quad (1.6)$$

where  $\eta_0$  is a pre-exponent factor,  $D$  is the parameter which controls how closely the system obeys the Arrhenius law (ideally  $D = \infty$ ). The effect of changing  $D$  from 5 to 100 is displayed in the insert of Figure 1.7.

Similarly, fragility has also been observed in colloidal glasses<sup>88</sup> and confined colloidal liquids<sup>89</sup>, which opens up the possibility of studying the glass transition phenomenon by varying parameters other than temperature. In this case, suitable parameters can be repulsive to attractive molecular interactions and spatial confinement.<sup>90</sup>

### 1.2.3 Colloidal glasses

In the 1980s, colloidal systems were introduced as model systems that display a glass transition.<sup>91</sup> Colloidal suspensions are composed of small to intermediate (1 nm to 1  $\mu$ m radius) solid particles in a liquid and include polymer suspensions, foams, emulsions, slurries and pastes.

If we focus on the particle size criterion in this definition, what is called polymer solution in this thesis can also be considered as a colloidal system given that the size of the polymer particle can exceed 1 nm. For this reason, the use of “polymer particles/solution” and “colloidal particles/suspension” is interchangeable in the text of this thesis.

By analogy to molecular glasses, colloidal suspensions exhibit a slowing down of their structural relaxation process when the particle volume fraction (concentration) reaches a critical value, usually leading to a dramatic increase of the viscosity of the system.<sup>92</sup> This phenomenon is described as the colloidal glass transition and shows some similarities with temperature-dependent glass transition such as cooperative particle motions<sup>93</sup> and anomalies in the vibrational density of

states<sup>94</sup>. A supercooled or a colloidal glassy state is reached when the packing volume fraction of colloidal particles is increased toward  $\phi \sim 0.494$  fast enough to avoid crystallization.<sup>95</sup>

Although the effective volume fraction of the most concentrated colloidal glass is expected to reach the universal random close packing density (RCP;  $\phi_{RCP}$ )  $\phi_{RCP} \sim 0.636$  for hard sphere colloids (lacking attractive and long-range interactions),<sup>96</sup> the packing density reported at the colloidal glass transition<sup>97</sup> is  $\phi_g \sim 0.58$ . This makes colloidal glasses far from being ideal glasses, especially as the RCP cannot be reached when the system gets out of equilibrium.

As colloidal glasses are in a non-equilibrium state, they generally need a relaxation time ( $\tau$ ) to rearrange their structure toward a more stable configuration. A two-step relaxation for colloidal glassy systems has been identified in the framework of mode coupling theory (MCT).<sup>98</sup> MCT describes the temporal density fluctuations in supercooled liquids through density autocorrelation functions.<sup>99</sup>

A comparison between the decay of density autocorrelation functions as a function of  $\log(\text{time})$  of a simple liquid and a supercooled liquid are depicted in Figure 1.8. The simple liquid shows only a single exponential decay and enables the determination of one characteristic relaxation time.

However, supercooled liquids exhibit multi steps decay associated with more than one relaxation time:

- First, an initial microscopic short-time relaxation related to the vibrations of the colloidal particles around their initial configurations or intermolecular collision, named  $\beta$ -relaxation.
- Second, at intermediate times, particles appear to be trapped in cages formed by their nearest neighbors. This region is characterized by a plateau whose length increases with the packing density of particles  $\phi$ .
- Finally, when the particles break free from their cages, a final relaxation is observed during long periods of time, known as the  $\alpha$ -relaxation.

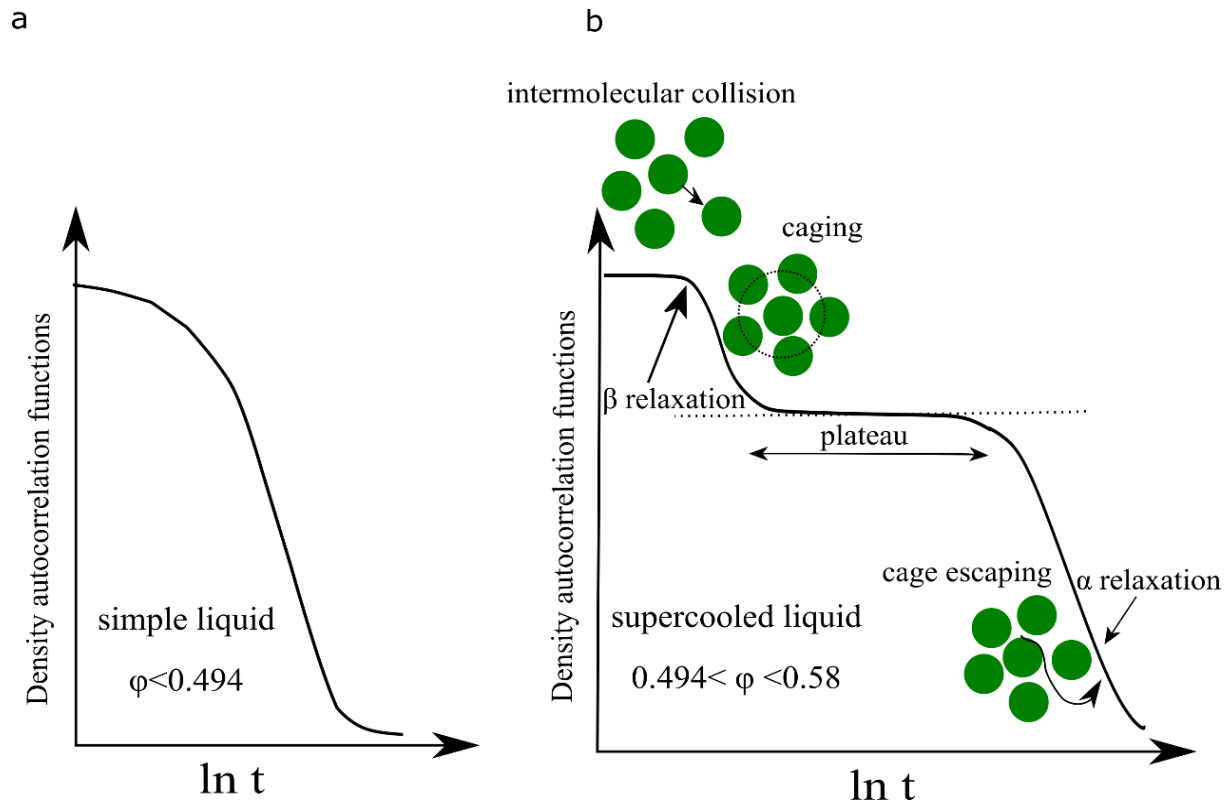


Figure 1.8 Density autocorrelation functions as a function of log (time) of a simple liquid exhibiting a simple exponential decay (a) and a supercooled liquid with multi-step decay (b). The  $\beta$ -relaxation decay represents the short-time relaxation processes in a cage, while the  $\alpha$ -relaxation decay time represents the diffusion of the molecules out of the cage at longer time scales. Reprinted and adapted from Reichman, D. R. and Charbonneau, P. J. *Stat. Mech.* 2005, P05013. © IOP Publishing Ltd and SISSA Medialab srl. Reproduced by permission of IOP Publishing. All rights reserved

Analyzing the decay autocorrelation functions related to supercooled liquids shows the non-exponential nature of the  $\alpha$  and  $\beta$  relaxations. While the  $\beta$ -relaxation decay can be described by a

simple power law, the  $\alpha$ -relaxation decay is described typically by a stretched exponential fitting a Kohlrausch-Williams – Watt (KWW) function:  $\exp\left(-\frac{t}{\tau}\right)^\beta$ .<sup>100,101</sup>

The KWW function is a description of relaxations in disordered systems where  $\tau$  is the relaxation time and  $\beta$  the stretching coefficient. The stretching coefficient indicates whether the density autocorrelation function decays slower than a simple exponential when  $\beta < 1$  (also called stretched exponential function) or faster ( $\beta > 1$ ), also named compressed exponential function.

The stretched exponential function has been found empirically in various amorphous materials, such as polymers,<sup>74</sup> glasses,<sup>102</sup> and glass-forming liquids near the glass transition temperature.<sup>103</sup> The physical meaning of this function is assumed to be linked to dynamical heterogeneities due to the coexistence of different particle populations having different relaxation times which range from fast to slow (from picoseconds to seconds, minutes or more). The stretching exponent  $\beta$  decreases with temperature, marking a larger and larger deviation from a simple exponential relaxation. Direct access to dynamical heterogeneities in dense supercooled colloidal liquids is possible through the use of microscopic methods such as wide-field microscopy and confocal microscopy.<sup>104,105</sup>

However, compressed exponential behavior is rather rare and was attributed to the dynamics of “soft glassy materials” such as colloidal glasses,<sup>106</sup> colloidal gels,<sup>107</sup> and concentrated emulsions.<sup>108</sup> The physical origin of this behavior is nevertheless far from being understood, although the most commonly accepted scenario is the random appearances of “micro collapses”, which lead to stress-induced rearrangements within the glass network.<sup>109</sup>

## 1.2.4 Glass interfaces

The use of glassy materials confined to the nanometer scale is interesting for nanotechnological applications including ultrathin membranes for gas separation,<sup>110</sup> nanoimprint lithography<sup>111</sup> and novel nanocomposites.<sup>112</sup> Understanding how confinement changes the properties of confined glasses is interesting from both a fundamental and technological point of view: First, it provides better insight into the changes in dynamics and mechanical properties of glassy thin films as compared to properties of bulk glass, and secondly it enables the production of better nanoscale materials.

Most studies of confined glasses were dedicated to polymer free-standing thin films using several experimental techniques such as ellipsometry,<sup>113</sup> dielectric spectroscopy,<sup>114</sup> X-ray reflectivity,<sup>115</sup> probe fluorescence intensity,<sup>116</sup> etc. Some have showed that the geometrical restriction of polymeric films leads to deviation of  $T_g$  values compared to their respective bulk values.<sup>113,117,118</sup> However, most of these investigations are contradictory as  $T_g$  can increase, decrease or remain the same compared to the bulk value.

Other studies have determined that the glass transition of a polymer film depends on its thickness and can either decrease or increase depending on the interaction between the film and its substrate.<sup>114,119,120</sup>

In contrast to polymer glasses, the behavior of colloidal glasses was rarely investigated under spatial confinement. The few published works in this research area were dedicated to studying the growth of dynamic heterogeneity or hindered diffusion of hard sphere colloids between two solid plates or cylindrical cavities using confocal scanning laser microscopy.<sup>89,121,122</sup>

The confinement of soft colloidal particles has been less studied compared to hard colloidal particles despite their interesting features. First, these particles can be packed above  $\phi_{RCP} \sim 0.636$  due to their compressibility. Second, their size can be controlled by external stimuli including temperature, pH and light.

This second feature allows for the same particles to be tested *in situ* how their softness affects the kinetics of colloidal glass formation in addition to the inherent evolution of the elastic properties. To the best of the author's knowledge, only thermoresponsive P(NIPAAm) microgel particles were studied in confinement between two solid surfaces using a micron gap rheometer and confocal microscope.<sup>123</sup> By controlling the temperature, it has been shown that the formed layers share many striking similarities with molecular glass formers in terms of structure, viscoelasticity and single particle dynamics.

As part of this thesis, we studied and extrapolated some of these properties of confined colloidal glasses using another technique: The Quartz Crystal Microbalance with Dissipation Monitoring.

## 2. Fundamentals

### 2.1 Quartz Crystal Microbalance with Dissipation monitoring (QCM-D)

#### 2.1.1 Overview

An interesting way to measure mechanical properties of thin films is the propagation of acoustic waves within them and the reflection of these waves at the interface of the substrate and the thin film/air.<sup>124,125</sup> Quartz resonators have become popular for the determination of the properties of thin films that cover quartz crystal surfaces and interfaces.<sup>126–128</sup> This is mainly due to their usefulness in weighing very small masses and evaluating time-dependent mechanical changes faster than other characterization techniques (such as microindentation and nanoindentation).<sup>129</sup>

The quartz crystal microbalance (QCM) technique was first introduced in Günter Sauerbrey's 1959 thesis on the use of the harmonic acceleration field of quartz for mass measurement.<sup>130</sup> At the time, the main application of QCM was the measurement of mass deposition rates in vacuum deposition technology.<sup>131</sup>

Starting from the 80's, QCM has become a powerful analytical tool to characterize liquids in contact with a resonating surface thanks to Kanazawa and Gordon's work on the coupling between elastic and viscous shear waves.<sup>132</sup>

New QCMs in the 90's were developed based on impedance analysis in frequency domain. The advantages of this analysis are twofold: first, it supplies the frequency and bandwidth; second, different harmonics (overtones) can be sequentially analyzed.<sup>133</sup>

In the meantime, commercial QCMs based on the ring down principle were developed in 1995 at Chalmers University (Sweden).<sup>134</sup> The later ones are called Quartz Crystal Microbalance with Dissipation Monitoring, QCM-D because they provide the "dissipation factor" in time domain.

QCMs have been used for different *in situ* studies related to soft thin layers including swelling,<sup>135</sup> aging,<sup>136</sup> curing,<sup>137</sup> adsorption at the solid-liquid interface,<sup>138</sup> high frequency rheological study of glassy and rubbery polymers,<sup>139</sup> etc.

## 2.1.2 Quartz Crystal

The sensing part of the Quartz Crystal Microbalance is a single crystal quartz resonator disk cut at an angle of  $35^{\circ}15'$  from the Z-axis (called AT-cut) of the quartz crystal. This AT-cut is chosen to ensure that when an electric potential is applied, the deformation of the crystal generates a thickness shear mode.<sup>140</sup> This implies that the shear deformation can be excited into resonance when the crystal thickness is near an odd multiple of half the generated acoustic wavelength.

The typical thickness of the crystal is  $\sim 330\ \mu\text{m}$  while its active area is  $\sim 1.54\ \text{cm}^2$ . The disk is covered with two circular gold electrodes patterned on both sides as shown in Figure 2.1. The front electrode, which is exposed to the sample, is normally larger than the back electrode, guaranteeing that the whole active side is homogeneously covered by the front side. The front side is generally covered with a receptor layer such as gold, silicon dioxide, titanium oxide, polystyrene, etc. These layers are deposited via vapor deposition technique and they should have good interaction with the liquid sample.

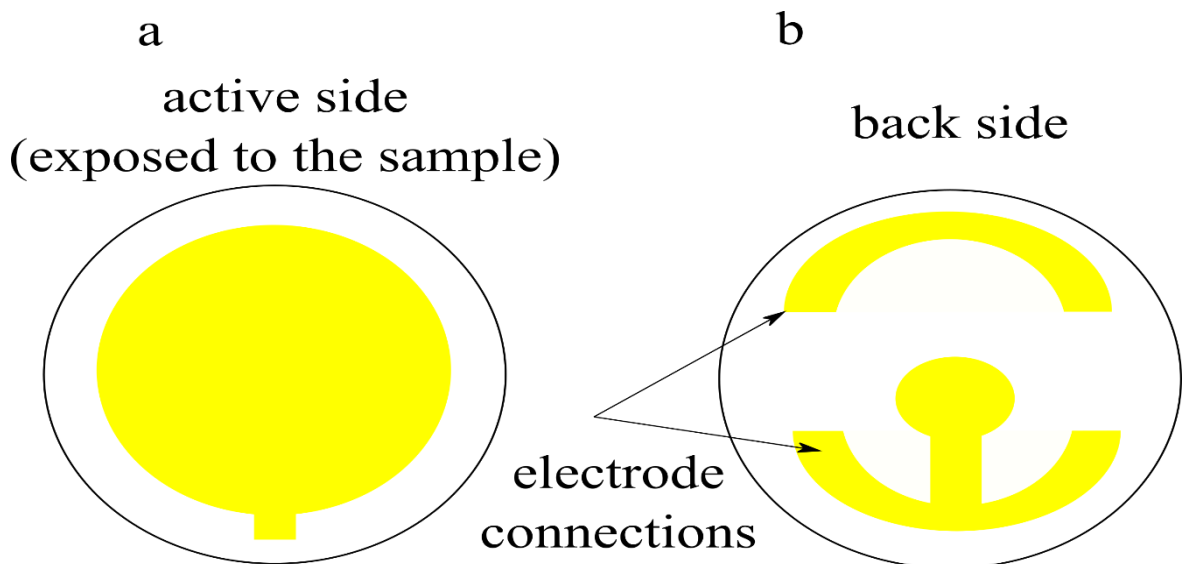


*Figure 2.1 Schematic representation of electrode patterns from the front (a) and from the back (b). Outer circles correspond to the size of the quartz crystal. The yellow filled area is the evaporated gold electrode. The front electrode is exposed to the sample. The back electrode is smaller than the front electrode to ensure the confinement of oscillations to the central region of the crystal. The quartz crystal has two electrode connections to electronics: the top connects to the back electrode and the bottom to the front electrode.*



### 2.1.3 Impedance analysis and ring down

When a voltage is applied to the electrodes, the inverse piezoelectric effect provokes a shear deformation as previously mentioned. In frequency domain experiments, whenever the frequency of the exciting alternating voltage matches one of the acoustic resonance frequencies of the quartz, the amplitude of the shear oscillation becomes maximum. Measuring the electrical conductance inside the electrodes therefore enables the determination of resonance frequencies. The resonance frequency is defined here as the frequency where the electrical conductance of the equivalent circuit is maximal (as shown in Figure 2.2).

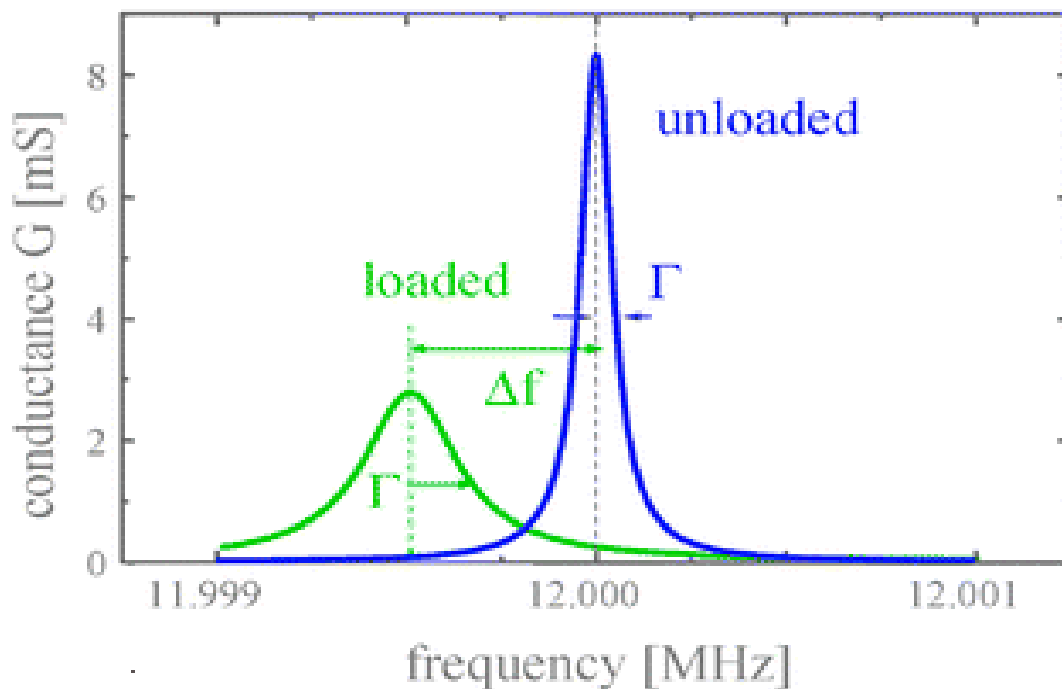


Figure 2.2 Impedance analysis based on the electrical conductance curves. The blue curve represents the resonance peak of an unloaded quartz crystal while the green curve represents the resonance peak of a loaded quartz crystal.  $\Gamma$  represents the bandwidth (half width at half height of the resonance peak) and  $\Delta f$  the resonance frequency shift which is the difference between the resonance frequency of the loaded and the unloaded quartz crystals. Reproduced/Adapted from reference<sup>143</sup> with permission from the PCCP Owner Societies.

If a Lorentzian peak function is fitted to the conductance curve, two parameters are obtained describing the complex resonance frequency  $f_n^*$ : the resonance frequency ( $f_n$ ) of the quartz as the

real part, and the half width at half maximum of the resonance peak ( $\Gamma_n$ ) representing the imaginary part.

A thin layer or load on the quartz crystal surface generates a complex resonance frequency shift  $\Delta f_n^*$  compared to the unloaded state, which can again be separated into  $\Delta f_n$  (the real part) and  $\Delta \Gamma_n$  (the imaginary part) according to equation (2.1)

$$\Delta f_n^* = \Delta f_n + i \Delta \Gamma_n \quad (2.1)$$

The fundamental resonance frequency of AT-cut quartz crystal resonators operated in shear mode is typically near 5 MHz.

It is worth noting that due to the small size of the quartz crystal, poor energy trapping can occur at the fundamental frequency, resulting in bad signal-to-noise ratio.<sup>134</sup>

More resonances are observed at the odd harmonics of this fundamental frequency, where the subscript  $n$  refers to the  $n^{\text{th}}$  harmonic (i.e.  $n = 1$  for the fundamental resonance frequency of 5 MHz, and  $n = 3$  for the third overtone at  $\sim 15$  MHz).

Under resonance conditions, the shear deformation of the resonator is associated to a standing sound wave at the surface. The wavelength of sound wave is twice the thickness of the quartz crystal  $d_q$ , as mentioned in the overview.

If a thin film is deposited on one surface of the quartz crystal and has the exact same acoustic properties as the resonator, then the acoustic thickness of the resonator increases by the film thickness  $d_f$ .<sup>141</sup> This results in an increase of the sound wavelength ( $\lambda$ ) and a decrease of the resonance frequency ( $f_n$ ) according to equation (2.2)

$$f_n = \frac{c_q}{\lambda} = \frac{c_q}{(d_q + d_f)} \quad (2.2)$$

where  $c_q$  is the speed of the sound wave.

The damping of shear waves can be quantified generally either by the half-width at half-height of the resonance peak in the frequency domain (half-bandwidth) or by the inverse of the quality factor also known as the dissipation factor ( $D_n$ ) in time domain. The dissipation factor is inversely proportional to the time needed for the current oscillation to decay completely. Moving from  $\Gamma_n$

found from the frequency data to  $D$  extracted from time data is done by Fourier Transformation (FT) as displayed in Figure 2.3

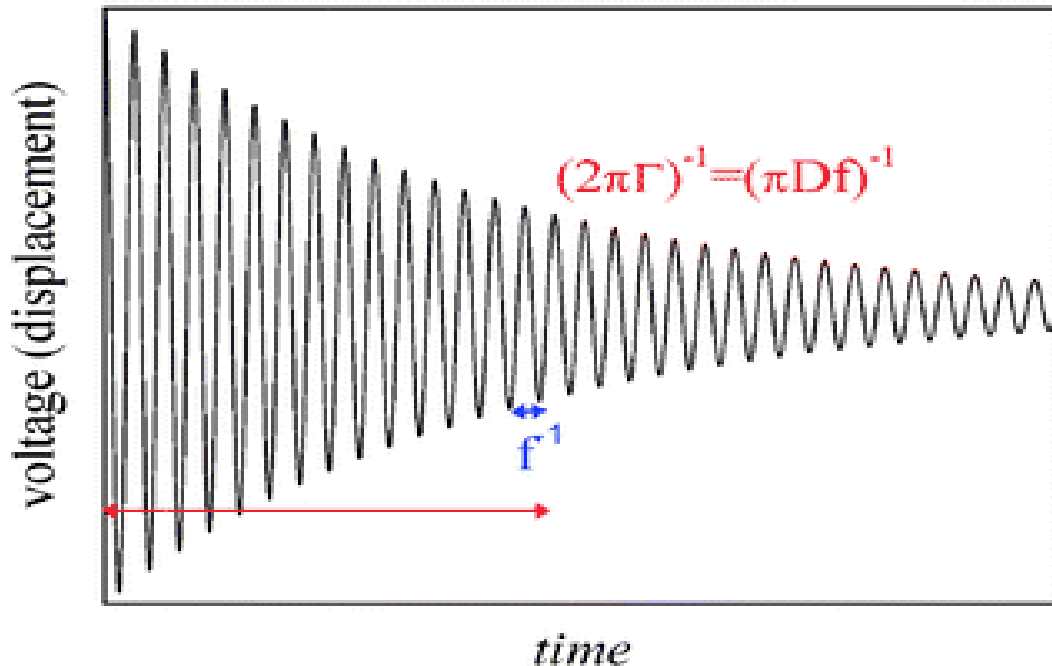


Figure 2.3 Ring down of voltage oscillation in the time domain. This signal can result from Fourier transform of the acquired data in the frequency domain. The main extracted parameter is the dissipation factor  $D_n$ . Reproduced/Adapted from reference<sup>143</sup> with permission with permission from the PCCP Owner Societies.

In this thesis, the measurements were carried out in time domain using the QCM-D technique, where “-D” stands for “with dissipation monitoring”. The QCM-technique used here is based on the principle of “ring down”: the excitation is induced with a radio frequency pulse corresponding to the resonance frequency of the quartz crystal. When the excitation is shut off, the current decays as an exponentially damped sinusoidal of a harmonic oscillator.<sup>142</sup> The dissipation factor  $D_n$  is inversely proportional to the time needed for the current oscillation to decay completely. The resonance frequency  $f_n$  and the dissipation factor  $D_n$  are acquired by periodically switching off the oscillating quartz crystal and recording then transferring the oscillations to a computer. The

information obtained from the ring down oscillations is linked to the information extracted from impedance analysis by equation (2.3)

$$D_n = \frac{2\Gamma}{f_n} \quad (2.3)$$

The software of QCM-D normally displays two outputs:  $\frac{\Delta f_n}{f_n}$  the normalized frequency shift and the shift in dissipation factor  $\Delta D_n$  in units of  $10^{-6}$ , where  $n$  is an odd integer related to the overtone order. With a 5 MHz crystal, the complex resonance frequency shift  $\Delta f_n^*$  is related to  $\Delta f_n$  and  $\Delta D_n$  by equation (2.4)

$$\Delta f_n^* = \Delta f_n (1 + i 2.5 \times 10^6 \times \Delta D_n) \quad (2.4)$$

### 2.1.4 Rigid and soft thin films

The adsorbed rigid mass can be quantified using the Sauerbrey equation,<sup>130</sup> where the adsorbed areal mass density  $m_f$  correlates with  $\Delta f_n^*$ <sup>143</sup> as shown in equation (2.5)

$$\frac{\Delta f_n^*}{f_1} = \frac{-2f_n}{Z_q} m_f \quad (2.5)$$

Here,  $f_1$  is the fundamental frequency and  $Z_q = 8.8 \times 10^6 \text{ kg.m}^{-2} \cdot \text{s}^{-1}$  is the acoustic impedance of quartz.

The areal mass density is usually expressed in  $\text{ng/cm}^2$  and sometimes in  $\mu\text{g/cm}^2$ . The maximum mass sensitivity of the technique in liquid is less than  $1 \text{ ng/cm}^2$ .

Getting the Sauerbrey thickness requires knowledge of the film density.

For instance, with a 5 MHz quartz crystal and a density of  $1 \text{ g/cm}^3$ , an areal mass density  $100 \text{ ng/cm}^2$  corresponds to a thickness of 1 nm. The deposition of a 1 nm film shifts the frequency by  $\sim 6 \text{ Hz}$ .

The Sauerbrey equation is strictly valid only for “rigid”, evenly distributed and thin adsorbed films exposed to air.

However, for sufficiently non-rigid adsorbed films, this will not be the case as the Sauerbrey equation fails to quantify the thickness of thicker films for two main reasons.<sup>144</sup>

The first reason is related to the propagation of the shear acoustic wave in a viscoelastic film or thicker film. Because the acoustic wave is reflected partially at the outer edge of the film and returns to the resonator surface,  $\Delta f_n^*$  is not directly proportional to  $m_f$ .

The second reason is connected to the definition of the areal mass density. In general,  $m_f$  is taken for dry areal mass of a the deposited layer without taking into account the hydrodynamic effects of the coupled solvent (e.g. adding supplementary mass *via* hydration).

For a viscoelastic film immersed in a liquid environment, a viscoelastic correction is required to account for viscous dissipation, whereby softness reduces the apparent rigid Sauerbrey thickness<sup>133</sup> as shown in equation (2.6) where  $\omega = 2\pi f$  is the angular speed,  $Z_{liq} = \sqrt{n \cdot 2\pi i \cdot f_1 \rho_{liq} \eta_{liq}}$ ,  $Z_{film} = \sqrt{\rho_{film} G_{film}}$ ,  $Z_{liq}$  is the acoustic impedance of the bulk liquid,  $Z_{film}$  the acoustic impedance of the film,  $\rho_{liq}$  is the density of the bulk liquid,  $\eta_{liq}$  the dynamic viscosity of the bulk liquid,  $\rho_{film}$  the density of the film and  $G_{film}$  the shear modulus of the film:

$$\frac{\Delta f_n^*}{f_1} = \frac{-\omega m_f}{\pi Z_q} \left( 1 - \frac{Z_{liq}^2}{Z_{film}^2} \right) \quad (2.6)$$

In this equation, the frequency shift can be seen as a combination of a viscoelastic contribution and an inertial contribution.

From the viscoelastic term, one can guess that QCM can be used to determine the viscosity-density product of the bulk liquid and that the shear modulus of the film is expected to depend on the overtone order (harmonics). This observation supports the study done by Kanazawa and Gordon of a quartz resonator response operating in contact with a semi-infinite Newtonian liquid.<sup>132</sup>

They estimated that the resonance frequency decreases proportionally to  $\sqrt{\rho_{liq} \eta_{liq}}$ . They also derived the distance needed by the shear wave to decay in the liquid, commonly called penetration

depth ( $\delta$ ).  $\delta$  is  $\sim 250$  nm at 5 MHz in water, and increases with increasing viscosity and decreases with increasing overtone order.

In general, the resonance frequency shift  $\Delta f_n$  is negative due to mass loading, which decreases the resonance frequency of the quartz crystal (in comparison to the unloaded/empty state) while the dissipation shift  $\Delta D_n$  is positive.

According to Krim and Widom, the dissipation shift could also be related to interfacial friction (in addition to viscoelasticity), due to adsorbates sliding against the substrate.<sup>145</sup> A small degree of slippage should occur even for very thin layers expressed by a partial decoupling between the resonator and the film.

Due to industrial processing, the surface of the quartz crystals can also be rough. Operating liquids when the surface is rough can make the interpretation of  $\Delta f_n$  complicated especially when the roughness of the receptor layer is on the same scale as the penetration depth  $\delta$ .<sup>146</sup> A rough surface can lead to the trapping of liquid molecules in cavities and pores and force them to oscillate with the quartz. It can also generate nonlaminar motion and compressional acoustic waves<sup>147</sup> which also contribute to the dissipation shift.<sup>148</sup>

According to the manufacturer of quartz crystals, the surface roughness of the electrode is less than 3 nm root mean square (RMS). Therefore, the effect of roughness will be neglected in this manuscript.

### **2.1.5 Temperature**

The temperature of QCM-D experiments can be controlled between 15 and 65°C with a temperature control of  $\pm 0.02$  °C. The temperature of the quartz crystals can be increased or decreased using a Peltier module. Consequently, this temperature control can allow to carry out temperature-dependent kinetic studies at the solid-liquid interface either in isothermal or non-isothermal mode.

Quartz crystals are piezoelectric materials which can be affected by temperature changes. This temperature effect can lead to variation in  $\Delta f_n$ . AT-cut quartz crystals are characterized by temperature compensation, which minimizes the dependence of  $\Delta f_n$  on temperature (frequency-temperature coupling) in the range -60°C to 100°C.<sup>149</sup> Despite the temperature compensation, there

is a remaining temperature-frequency coupling that can be described approximately by a cubic polynomial.

Additionally, upon heating the crystal and cooling it down again to the same temperature, the resonator does not return to the exact same frequency. This hysteresis is most probably induced by the migration of crystalline defects due to temperature variation.

When operating QCM-D for kinetic studies and thus temperature becomes an important variable, the effect of temperature on the quartz crystal and also on the physical properties of the liquid (viscosity, density) should be taken into account.

Before an experiment, it is better to run the QCM in both air and liquid while varying the temperature. The frequency shift and dissipation shift values obtained for these background runs will then be subtracted from the one of the studied system. This subtraction has the advantage of giving the changes in frequency and dissipation shifts corresponding to the studied material rather than to the instrumental artefacts.

### **2.1.6 Light**

Shining light on the top of quartz crystals is possible through the window module conceived by Biolin Scientific company (Västra Frölunda, Sweden). This module has a sapphire window with an optical transmittance > 80% in the 300 to 400 nm wavelength range.

Light with different wavelengths was used on top of quartz crystals for the *in situ* study of different physical phenomena happening on the surface, such as polymer film degradation,<sup>150</sup> growth of polymer brushes,<sup>151</sup> and desorption of photoactive compounds from membranes.<sup>152</sup>

In all these studies, unloaded substrates (bare quartz crystals with no polymer film) sensors exhibit a change in frequency and in dissipation (the change is more pronounced with the frequency than the dissipation) in response to different wavelengths in the UV-VIS range and light intensities upon illumination with a light source.

This frequency shift is most likely due to a possible localized heating (perpendicular to the electrode) which may cause stress in the sensor. The higher the light intensity, the higher the frequency shift due to a higher amount of induced stress.<sup>150</sup>

When studying the effect of light on material at the solid-liquid interface with QCM-D, it is recommended to first perform a reference experiment with the same illumination conditions on an unloaded sensor in order to subtract the light-induced frequency and dissipation shifts from the experimental data related to the investigation of light response of the studied material.

## **2.2 Dynamic Light Scattering (DLS)**

### **2.2.1 Overview**

Dynamic light scattering is a well-established technique to characterize sub-micrometric colloidal particles and macromolecules. This technique is based on a time-resolved measurement of the intensity of scattered light from a sample that contains particles dispersed in a solvent.<sup>153</sup>

When a monochromatic beam of light encounters the particles, light scatters in all directions depending on the size and shape of the analyzed particles as well as on temperature and solvent viscosity. Due to the random motions of particles, the intensity of scattered light fluctuates over time. The frequency of these temporal fluctuations provides information about the diffusion coefficient of the particles, which is related to particle size. Hence, a size profile distribution can be determined.<sup>154</sup>

In the context of thermosensitive polymer studies, DLS has been used to investigate the structural changes as a function of temperature in terms of polymer size, relationship between the size of the polymer and other parameters such as molecular weight, heating rate, concentration, etc.<sup>28,155–157</sup>

### **2.2.2 DLS instrument**

The sample analyzed with DLS is usually irradiated with a monochromatic light source.

Typically, lasers with vertical polarization are used (He-Ne with 632.8 nm or Ar-ion with 592 nm). The scattered light from the particles is collected by a detector under the scattering angle  $\theta$ . The detector contains a photomultiplier which counts the scattered photons and processes them to obtain an image projected onto a screen (also called a Speckle pattern).<sup>153</sup>

### **2.2.3 Brownian motion**

Colloidal particles are always in motion due to non-compensated collision of the solvent molecules. This small and random motion is called Brownian motion.<sup>158,159</sup>



The constant collisions between colloidal particles and solvent molecules lead to a random walk of the particles. Einstein theorized that the mean squared displacement (MSD) is proportional to time as shown in equation (2.7)

$$\text{MSD} = 6 D_t t \quad (2.7)$$

where  $D_t$  is the transitional diffusion coefficient.

In this equation, the motion of particles is assumed to happen in a three dimensional space. However, Einstein considered a one-dimension space in which the particle moves on a line to the left or to the right. Later, a relationship between  $D_t$  and the particle size measured *via* the hydrodynamic radius  $r_h$  was established, giving the famous Stokes-Einstein equation (see equation (2.8))

$$D_t = \frac{k_b T}{3\pi\eta r_h} \quad (2.8)$$

This equation infers that the friction exerted by a moving particle is proportional to its radius and the viscosity of the surrounding solvent.<sup>158</sup> Since DLS measurements are based on this fundamental equation, an accurate temperature reading is important to measure particle size.

### **2.2.4 The dynamic light scattering principle**

When a laser beam encounters colloidal particles or macromolecules, the incident light scatters in all directions and the scattered light is recorded by a detector of the DLS instrument. The fundamental assumption in the theory of dynamic light scattering is that the scattered light has the same frequency as the incident beam.

Nevertheless, due to different velocities of the moving particles in solution, the light undergoes a “Doppler Broadening” leading to its frequency shifting.<sup>160</sup> Consequently, the scattered light intensity is not constant but fluctuates around a mean value. The digital autocorrelator associated with the DLS instrument correlates intensity fluctuations of scattered light ( $I$ ) with respect to time (ns- $\mu$ s) to determine how rapidly the intensity fluctuates, which is connected to the diffusion behavior of particles.

Large particles are characterized by slow intensity fluctuations while small particles display rapid intensity fluctuations.

### 2.2.5 Data analysis

In a dynamic light-scattering experiment, the signal can be interpreted in terms of an autocorrelation function describing the motion of the particles under investigation.

The principle of autocorrelation is to measure the degree of similarity between two signals or one signal with itself at different time intervals. The digital autocorrelator previously mentioned processes incoming data and provides an outgoing autocorrelation function  $G(\tau)$  of the scattered intensity  $I$  characterized by a lag time  $\tau_{lag}$  between two points (delay time), as shown in equation (2.9)

$$G(\tau) = \langle I(t) \cdot I(t + \tau) \rangle \quad (2.9)$$

For a large number of monodispersed particles, the autocorrelation function decays following an exponential decay as a function of the delay time according to equation (2.10)

$$G(\tau) = A_{DLS} [1 + B_{DLS} \exp(-2\Gamma\tau)] \quad (2.10)$$

where  $A_{DLS}$  is the baseline of the autocorrelation function,  $B_{DLS}$  is the intercept of the autocorrelation function and  $\Gamma$  is the decay constant related to the diffusion behavior of colloidal particles,

$$\Gamma = D_t q^2 \quad (2.11)$$

$\Gamma$  is expressed in equation (2.11) where  $q$  is the Bragg wave vector, while

$$q = \frac{4\pi n_{refr}}{\lambda_{beam}} \sin\left(\frac{\theta}{2}\right) \quad (2.12)$$

$q$  is proportional to the refractive index of the solvent ( $n_{refr}$ ) as shown in equation (2.12), where  $\lambda_{beam}$  is the wavelength of the incident beam and  $\theta$  is the scattering angle at which the detector is placed.

$$G(\tau) = A[1 + B g_1(\tau)^2] \quad (2.13)$$

For polydisperse systems,  $G(\tau)$  cannot be represented by a single exponential function decay but should contain another function  $g_1$  expressing the sum of exponential decays contained in the autocorrelation function (see equation (2.13)).

The size of the studied particles is extracted from the autocorrelation function by using diverse methods. These methods depend on the way the DLS data are fitted and provide different information.<sup>154</sup>

The first method is monomodal distribution which relies on the fit of the autocorrelation function with a single-exponential function (equation (2.10)). This method is employed to obtain the mean particle size (z-average diameter) and an estimate of the width of the distribution (polydispersity index).

The second method is non-monomodal distribution and is based on the fit of a multiple exponential function (equation 2.13) to the autocorrelation function to obtain the distribution of particles. This is made possible by using algorithms such as Non-Negative Least Squares (NNLS) and Constrained Regularization Method for Inverting Data (CONTIN).

This latter method is the standard method to plot the relative intensity of scattered light by particles and divide them into various classes. It has the particularity of using a regularizer parameter to merge particle distribution peaks which are close to each other, which results in narrower distributions.

The analysis of data in this thesis is done through the CONTIN method *via* the ALV- 7004/USB FAST correlator.

## 3. Deposition Study of Dual Light- and Temperature-Responsive Soft Layers

The major part of this chapter has been published:

A. Ben-Miled, A. Nabiyan, K. Wondraczek, F. H. Schacher, and L. Wondraczek, Controlling Growth of Poly (Triethylene Glycol Acrylate-Co-Spiropyran Acrylate) Copolymer Liquid Films on a Hydrophilic Surface by Light and Temperature, *Polymers (Basel)*. 13, (2021).

### 3.1 Summary

Quartz crystal microbalance with dissipation monitoring (QCM-D) was employed for *in situ* investigations of the effect of temperature and light on the conformational changes of a Poly (triethylene glycol acrylate-co-spiropyran acrylate) (P(TEGA-co-SPA)) copolymer containing 12%–14% of Spiropyran at the silica–water interface. By monitoring shifts in resonance frequency and in acoustic dissipation as a function of temperature and illumination conditions, we investigated the evolution of viscoelastic properties of the P(TEGA-co-SPA)-rich wetting layer growing on the sensor, from which we deduced the characteristic coil-to-globule transition temperature, corresponding to the lower critical solution temperature (LCST) of the PTEGA part.

We show that when exposed to visible or UV light, the temperature of the coil-to-globule transition as characterized by the LCST of the adsorbed copolymer shifts to lower values as compared to the bulk solution: the transition temperature determined acoustically on the surface is 4 to 8 K lower than the cloud point temperature reported by UV/VIS spectroscopy in aqueous solution. We attribute our findings to non-equilibrium effects caused by confinement of the copolymer chains on the surface. Thermal stimuli and light can be used to manipulate the film formation process and the conformational state of the film, which affects its subsequent response behavior.

### 3.2 Introduction

Polymer adsorption at the interface solid-liquid interfaces is a very important process, which is relevant in many technological applications and biological processes.

In the last two decades, attention has also been paid to the adsorption behavior of stimuli-responsive polymers at solid-liquid interfaces. Prominent techniques to characterize smart layers are Surface Plasmon Resonance (SPR) and Quartz Crystal Microbalance with Dissipation Monitoring (QCM-D). QCM-D is a highly sensitive technique for characterizing adsorption and desorption phenomena at the solid-liquid interface. As an exemplary case, the adsorption of P(NIPAAm) on modified gold and silica surfaces was studied due to its conveniently accessible LCST of  $\sim 32$  °C, and also for its potential relevance in biomedical applications.<sup>161</sup>

These studies showed different behaviors of the adsorbed polymer depending on its state of adsorption, e.g., whether chemisorbed<sup>162,163</sup> or physisorbed.<sup>164,165</sup> The adsorption of thermosensitive block copolymers based on P(NIPAAm) onto gold surface was also investigated by QCM-D.<sup>166</sup>

For example, the adsorption mechanism of a pentablock terpolymer Poly (N-isopropylacrylamide)<sub>x</sub>-block-poly (ethylene oxide)<sub>20</sub>-block-poly(propylene oxide)<sub>70</sub>-block-poly (ethylene oxide)<sub>20</sub>-block-poly(N-isopropylacrylamide)<sub>x</sub> (PNIPAAm<sub>x</sub>-b-PEO<sub>20</sub>-b-PPO<sub>70</sub>-b-PEO<sub>20</sub>-b-PNIPAAm<sub>x</sub>) on gold was found to be affected by several parameters including concentration, relative block length, temperature, and the physical properties of the substrate.

Furthermore, adsorption properties of pH-sensitive cationic polyelectrolytes, e.g., Poly(diallyl dimethyl ammonium chloride) (PolyDADMAC) or Poly(allyl amine hydro-chloride) (PAH) on gold and silica surfaces were studied using QCM-D.<sup>167</sup> It was found that the adsorption properties of the polyelectrolyte depend on the surface chemistry, solution concentration, and solution pH.

As another example, QCM-D was employed to study the adsorption of polyelectrolyte monolayers of anionic Poly(styrene sulfonate) (PSS) on amino-functionalized silica, as well as cationic PAH and Poly-L-lysine (PLL) on bare silica.<sup>54</sup> Interestingly, the light-induced swelling behavior of spin-coated thin layers of P (NIPAAm-co-SPA) dual light- and temperature-responsive copolymers was described on the basis of QCM-D investigations.<sup>168</sup>

However, although the employed deposition method is technologically important for the fabrication of thin films on solid surfaces, it also has the limitation of making the film prone to delamination once the solvent wets the substrate.<sup>169</sup> Nevertheless, studying the adsorption of such copolymers appears very interesting from a physical point of view as they can adopt different conformations which can be tuned by light irradiation and temperature.

In a recent work (2019) from Grimm, Maßmann and Schacher,<sup>38</sup> SP-incorporating poly (oligo (ethylene glycol) acrylate)-based copolymers have been synthesized by nitroxide mediated polymerization with varying amounts of SP (from 0 to 16 mol%). The visible light irradiation of the copolymer dissolved in pH 8 TRIS buffer resulted in a decrease in its cloud point temperature by 30 K at 16 mol% SP content, as previously detected by UV/Vis spectroscopy. This chapter is a study of the conformational change of the dual light and temperature responsive copolymer P (TEGA-co-SPA) in solution and confined at the silica-water interface using QCM-D measurements. The simultaneous effect of UV light irradiation and temperature changes on the adsorption behavior of the copolymer was monitored.

Optical irradiation of the copolymer solution while undergoing adsorption provides a direct access to the question of how light can be used to tailor the kinetics of film formation and film conformation below and above the LCST.

## **3.3 Materials and Methods**

### **3.3.1 Copolymer synthesis**

#### *3.3.1.1 Chemicals*

2-Bromoethanol (95.0%), 2,3,3-trimethyl-3*H*-indol (97.0%), 2-hydroxy-5-nitrobenzaldehyde (97.0%), and triethylene glycol acrylate (98.0%) were purchased from TCI (Zwijndrecht, Belgium) and used as received. Acryloyl chloride (97.0%) was purchased from Sigma-Aldrich (Munich, Germany) and used as received. All solvents were of analytical grade except 1,4-dioxane and THF, which were purchased from Carl Roth (HPLC grade, Karlsruhe, Germany).

#### *3.3.1.2 NMR*

Measurements were carried out on a 300 MHz Bruker NMR spectrometer (Karlsruhe, Germany). The spectra were referenced to the residual solvent signal.

#### *3.3.1.3 Size Exclusion Chromatography SEC*

Measurements were performed on an Agilent 1260 system equipped with a G1330B pump, a PSS TC6001 oven at 30 °C, a G1362A refractive index detector, and a G1315D UV detector at 365 nm. THF was used as eluent at a flow rate of 1 mL min<sup>-1</sup> on three PSS SDV guard columns (100/1000/100 000 Å). The system was calibrated with Polystyrene, Poly (methyl methacrylate),

Polyethylene glycol, and Polyisoprene standards from PSS (Mainz, Germany) with a molecular weight range of 200–2 000 000 g mol<sup>-1</sup>.

### 3.3.1.4 Nitro-benzo-Spiropyran Acrylate (SPA) monomer synthesis

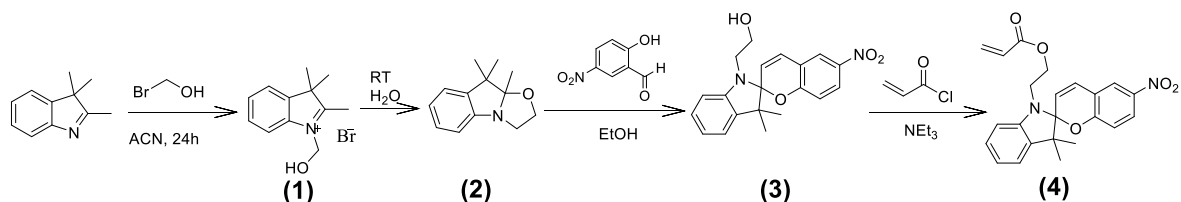


Figure 3.1 Synthetic route for 2-(3',3'-Dimethyl-6-nitrospiro[chromene-2,2'-indolin]-1'-yl) ethyl Acrylate (SPA)

#### 3.3.1.4.1 Synthesis of 1-(2-Hydroxyethyl)-2,3,3-trimethyl-3H-indolium Bromide

A mixture of 2,3,3-trimethyl-3H-indol (2.72 mL, 16 mmol) and 2-bromoethanol (1.48 mL, 20 mmol, 1.25 eq) in acetonitrile (20 mL) was reflux at 100 °C under Argon for 24 hours. The solvent was removed and resuspended in 25 mL hexane. The collected solid was recrystallized from chloroform and directly used in the following step.

#### 3.3.1.4.2 Synthesis of 9,9,9a-Trimethyl-2,3,9,9a-tetrahydro-oxazolo[2,3-a] indole

1-(2-Hydroxyethyl)-2,3,3-trimethyl-3H-indolium bromide was dissolved in aqueous solution (step1) mixed with KOH (0.66 g, 12 mmol). The mixture turned from pink to dark yellow within 10 min at room temperature. The mixture was then extracted with diethylether (3 × 20 mL), dried over MgSO<sub>4</sub>, filtered, and the solvent removed under reduced pressure. The yellow oil (0.8549 g, 33.5%) was analyzed *via* <sup>1</sup>H-NMR:

<sup>1</sup>H-NMR (300 MHz, CDCl<sub>3</sub>): δ = 1.89 (s, 3H, CH<sub>3</sub>), 1.31 (s, 3H, CH<sub>3</sub>), 1.42 (s, 3H, CH<sub>3</sub>), 3.44–3.86 (m, 4H, 2 × CH<sub>2</sub>), 6.76 (d, 1H, CH-arom.), 6.93 (t, 1H, CH-arom.), 7.14 (m, 2H) ppm.

#### 3.3.1.4.3 Synthesis of 2-(3',3'-Dimethyl-6-nitro-3'H-spiro[chromene-2,2'-indol]-1'-yl)-ethanol

9,9,9a-trimethyl-2,3,9,9a-tetrahydro-oxazolo[2,3-a] indole (0.85 g, 4,2 mmol, 1 eq) and 2-hydroxy-5-nitrobenzaldehyde (1.054 g, 6.3 mmol, 1.5 eq) were mixed in 10 mL of ethanol (step2) and heated under reflux for 3 h. After cooling to room temperature, the remaining solution was filtered and washed with ethanol. The red crystals (0.6319 g, 33%) were analyzed using <sup>1</sup>H-NMR:

<sup>1</sup>H-NMR (300 MHz, DMSO-d<sub>6</sub>): δ = 1.10 (s, 3H, CH<sub>3</sub>), 1.20 (s, 3H, CH<sub>3</sub>), 3.19 (dq, 2H, CH<sub>2</sub>), 3.44 (m, 2H, CH<sub>2</sub>), 4.72 (t, 1H, OH), 6.01 (d, 1H, CH-arom.), 6.64 (d, 1H, CH-arom.), 6.78 (t, 1H, CH-

arom.), 6.87 (d, 1H, CH-arom.), 7.11 (m, 3H, 3 × CH-arom.), 8.00 (dd, 1H, CH-arom.), 8.21 (d, 1H, CH-arom) ppm.

#### **3.3.1.4.4 Synthesis of 2-(3',3'-Dimethyl-6-nitrospiro[chromene-2,2'-indolin]-1'-yl) ethyl Acrylate (SPA)**

2-(3',3'-Dimethyl-6-nitro-3'H-spiro[chromene-2,2'-indol]-1'-yl)-ethanol (0.5 g, 1.42 mmol) and trimethylamine (0.197 mL, 1.42 mmol) were dissolved under Argon in dichloromethane (step3) and then the mixture was cooled to -35 °C. A solution of acryloyl chloride in dichloromethane was dropped slowly and the reaction mixture was heated up to room temperature overnight. The solution was extracted with saturated NaHCO<sub>3</sub> (2 × 20 mL) and water (2 × 20 mL), and the organic phases were combined, dried over MgSO<sub>4</sub>, filtered, and evacuated under reduced pressure. The product was purified using column chromatography with chloroform to yield 107.6 mg (0.265 mmol, 18.6%).

<sup>1</sup>H-NMR (300 MHz, DMSO-d<sub>6</sub>): δ = 1.06 (s, 3H, CH<sub>3</sub>), 1.19 (s, 3H, CH<sub>3</sub>), 3.36–3.51 (m, 2 × 1H, CH<sub>2</sub>), 4.16–4.35 (m, 2 × 1H, CH<sub>2</sub>), 5.90 (d, 1H, CH<sub>2</sub>) 5.96 (d, 1H, CH-arom.), 6.09 (dd, 1H, CH), 6.26 (d, 1H, CH<sub>2</sub>), 6.72 (d, 1H, CH-arom.), 6.80 (t, 1H, CH-arom.), 6.85 (d, 1H, CH-arom.), 7.12 (m, 2H, 2 × CH-arom.), 7.20 (d, 1H, CH-arom.), 7.99 (dd, 1H, CH-arom.), 8.21 (d, 1H, CH-arom.) ppm.

#### **3.3.1.4.5 Synthesis of P(TEGA-co-SPA)**

SPA (15 mol % SPA), triethylene glycol acrylate (TEGA) and azobisisobutyronitrile were dissolved in dioxane in a microwave vial. The solution was purged with argon for 30 min and heated to 110 °C for 48 h . The resulting red solution was precipitated twice into cold diethylether, resulting in a red powder. The copolymer was analyzed using SEC and <sup>1</sup>H NMR in CDCl<sub>3</sub> (step4).

The obtained copolymer was investigated via size exclusion chromatography with triple detection to obtain absolute molar masses and <sup>1</sup>H liquid NMR to determine the composition by comparing the signal of the SPA moiety (8.2 ppm, 2H) and the TEGA moiety (3.3 ppm, 3H). The fraction of SPA in the obtained copolymer was between 12–14 mol%, the molar mass M<sub>n</sub> was about 33,000 g/mol with a polydispersity index Đ = 1.7. An aqueous solution of 0.15 wt% P (TEGA-co-SPA) was obtained by diluting the copolymer in deionized water. Deionization was done using a Thermo Scientific Barnstead MicroPure water purification system to a resistivity of 18.2 MΩ cm<sup>-1</sup>.



### 3.3.2 Dynamic Light Scattering DLS

DLS measurements were performed using an ALV Laser CGS3 Goniometer (ALV GmbH, Germany) equipped with an He-Ne laser ( $\lambda = 633 \text{ nm}$ ) and an ALV-70027004/USB FAST correlator. All DLS measurements were performed at 25 to 77 °C. To determine the hydrodynamic radius, three measurements of 30 s each were performed at an angle of 90°. The analysis of the obtained correlation functions was performed using the correlator software (Correlator 3.2 beta 1).

### 3.3.3 QCM-D

QCM-D measurements were performed using a window module mounted on the QCM sensor (Q-sense E1 Biolin Scientific, Sweden). The employed sapphire window had an optical transmittance of >80% in the wavelength range 300 to 400 nm, in which UV irradiation was conducted.

AT-cut quartz crystal sensors coated with a 50 nm silicon dioxide layer (fundamental resonance frequency of typically  $\sim 4.95 \text{ MHz}$ , sensor area  $1.54 \text{ cm}^2$ ) were purchased from Biolin Scientific, Sweden. Prior to experiments, the quartz sensor was cleaned by soaking in a 2 vol% sodium dodecyl sulfate SDS solution for 30 min, rinsing with ultra-pure water, blow-drying with a gentle nitrogen flow and, finally, exposing to a UV/ozone cleaner for 15 min.

Several overtones were acquired, although the third overtone was generally selected for further analysis because of its sufficiently high level of energy trapping at this particular overtone when operated in liquids.<sup>143</sup>

To study the dual light and temperature induced conformational response of the P (TEGA-co-SPA) solutions, all experiments were performed in the liquid exchange mode by first purging with ultra-pure water for 30 min at 19 °C at a flow rate of 50  $\mu\text{L}/\text{min}$ . To avoid the formation of bubbles that can oscillate or migrate over the quartz crystal surface, all solutions were degassed in an ultrasonic bath (Elmasonic S 80) for 10 min prior to injection.

If not otherwise stated, irradiation of the sensor with the light source was started 20 min after equilibration and referencing under continuous water flow was completed. The diluted P (TEGA-co-SPA) aqueous solution was then introduced into the chamber at 30 min and at a temperature of  $20 \text{ }^\circ\text{C} \pm 0.02 \text{ }^\circ\text{C}$ . At this point, the flow rate was reduced to 20  $\mu\text{L}/\text{min}$ . Temperature ramping was conducted from the starting temperature of 20 °C up to a maximum of 47 °C, applying a constant heating rate of 0.2 K/min.

In the isothermal irradiation study, the P (TEGA-co-SPA) aqueous solution was fed for 25 min through the window module at a constant temperature prior to irradiation. Irradiation was done with a fluorescent lamp (visible light) or using an ultraviolet spotlight (365 nm, Opsytech, Germany). The power of the UV LED was fixed at 10% via an LED controller (with a maximum nominal power density of 25 W/cm<sup>2</sup>); the sample-to-LED distance was maintained at 75 mm.

During each run, changes in the resonance curves of the third overtone were continuously monitored and evaluated. The two resonance parameters under investigation were the change in dissipation factor  $\Delta D_3$ , and the shift in resonance frequency  $\Delta f_3/3$  being related to the mass of the adsorbate and the dynamically coupled liquid. While the resonance frequency shift  $\Delta f_3/3$  is more sensitive to the mass of the film, the variation of the dissipation factor  $\Delta D_3$  is related to viscous losses and interfacial sliding.<sup>170</sup> The acquired datasets were corrected for each sensor using a temperature sweep in pure water under continuous of visible or UV light for reference, see also Figure 3.2.

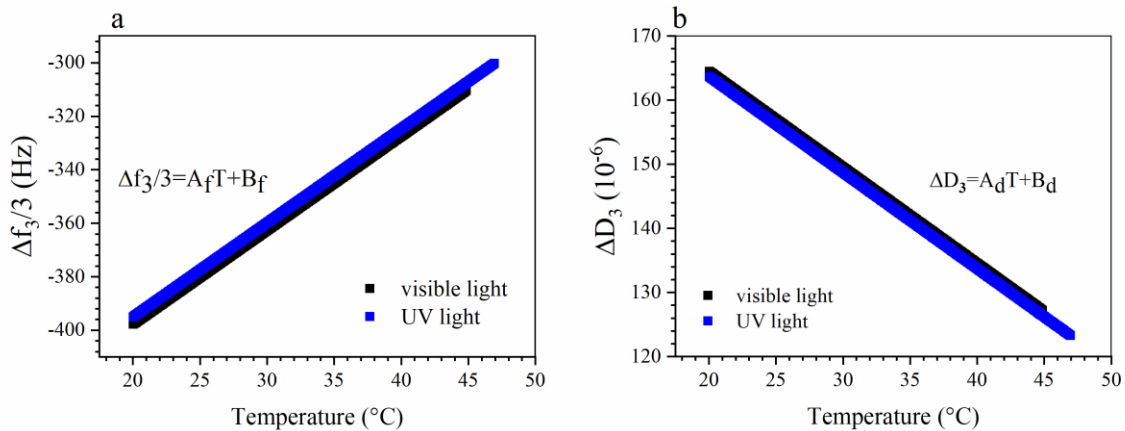


Figure 3.2 QCM-D temperature water sweep background used as a calibration curve to be subtracted from the data obtained in the presence of the dissolved copolymer to correct temperature dependency on the system for frequency shift (a) and dissipation shift (b).

This temperature correction was carried out by subtracting the calibration curve (pure water on sensor) from the one obtained in the presence of the dissolved copolymer. Table 3.1 provides the temperature dependent parameters obtained for the third overtone, each with the linear expression:  $\Delta f_3/3(T) = A_f T + B_f$ ,  $\Delta D_3(T) = A_d T + B_d$ .

It is worth noting that these parameters may also include some contributions specific to the electronics of the QCM-D, so these correction factors should ideally be determined for each QCM-D instrument.

Table 3.1 Fit parameters for the temperature correction as indicated in Figure 3.2

Irradiation	$A_f$ (Hz. °C <sup>-1</sup> )	$B_f$ (Hz. °C <sup>-1</sup> )	$A_d$ (10 <sup>-6</sup> . °C <sup>-1</sup> )	$B_d$ (10 <sup>-6</sup> . °C <sup>-1</sup> )
Visible light	3.52	-468.4	-1.5	194.5
UV light	3.52	-465.6	-1.5	193.7

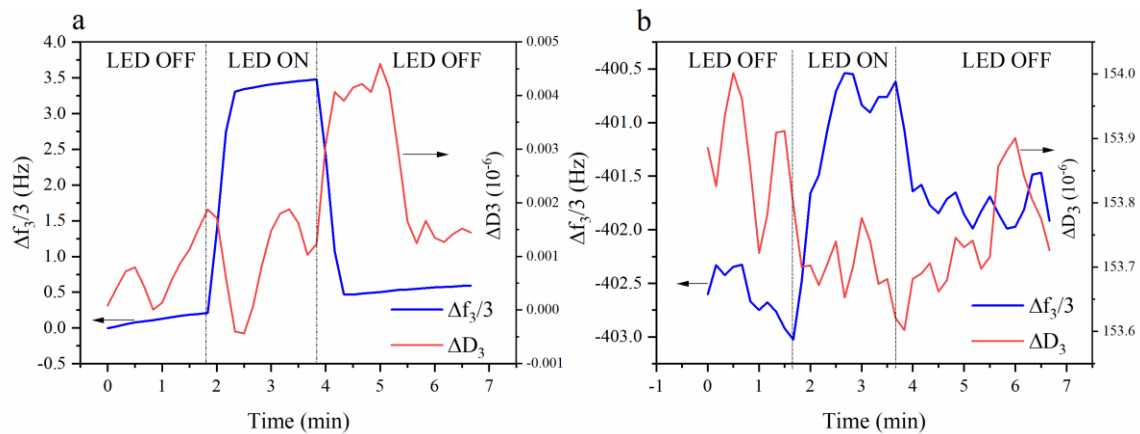


Figure 3.3 Effect of UV LED illumination at 20°C on bare silicon coated quartz crystal (a) and on the same quartz crystal totally wet with a water layer (b).

Furthermore, irradiation of the quartz crystal with UV light induced an increase in  $\Delta f_3/3$  by a few Hz. This behavior was previously attributed to photo-induced mechanical stress.<sup>151,152</sup> A further calibration was therefore done for UV-illumination by subtracting the effect of the UV light on the crystal for the non-isothermal measurements, see Figure 3.3.

As shown in Figure 3.3a, irradiation of a clean bare SiO<sub>2</sub>-coated sensor at 20°C results in an increase of  $\Delta f_3/3$  by ~3 Hz and little dissipation change  $< 0.1 \times 10^{-6}$  during the irradiation time and decreases again almost to the initial  $\Delta f_3/3$ . These results are in agreement with what was reported for the same type of crystal and they should have the same magnitude response in the temperature

range 19-50°C.<sup>150</sup> However, the same crystal shows a lower increase of  $\Delta f_3/3$  when the crystal is covered with a water film  $\sim 2.8$  Hz and dissipation shift  $>0.1 \times 10^{-6}$  (see Figure 3.3b).

### 3.4 Results and Discussions

#### 3.4.1 Phase Separation of P(TEGA-co-SPA) in Dilute Aqueous Solution

DLS data shown in Figure 3.4 provide an initial view of the effect of temperature on aggregation in the P(TEGA-co-SPA) polymer solutions containing between 12 and 14 mol% of Spiropyran in terms of the hydrodynamic radius. In order to reduce the effect of particle aggregation, we chose to work with a dilute concentration of 0.06 wt% (optically clear at room temperature). This is below the concentration used for DLS studies of similar thermoresponsive copolymers.<sup>157</sup> The hydrodynamic radius observed by DLS shows a sudden transition at a temperature of  $\sim 66$  °C. Below this temperature, the polymer chains exist as individually dissolved polymer chains with a small hydrodynamic radius of approximately 4–6 nm. Above 66 °C, aggregates (mesoglobules) with larger hydrodynamic radius of around 100–200 nm are formed.

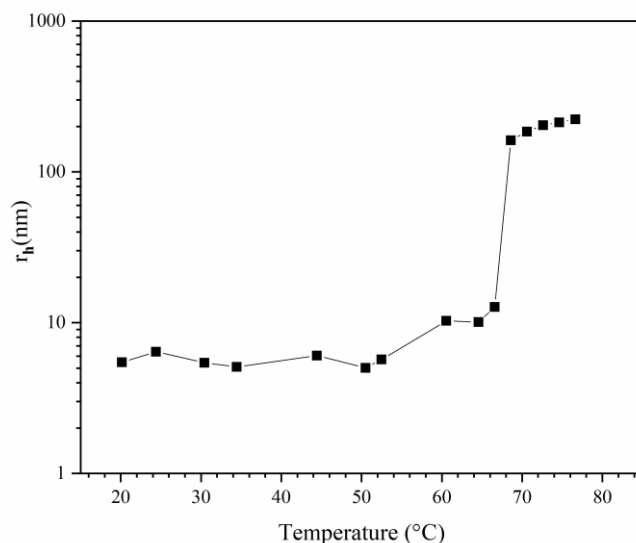


Figure 3.4 Hydrodynamic radius of a P(TEGA-co-SPA) copolymer in aqueous solution upon heating as determined from DLS measurements.

These values are comparable in size to other known polymers with a LCST.<sup>171,172</sup> At temperatures below the LCST, the copolymer chains are well solvated through hydrogen bonds.<sup>173,174</sup> Above the LCST, these exhibit van der Waals character, e.g., such as reported for P(NIPAAm).<sup>157,175</sup>

Interestingly, the observed transition temperature occurs  $\sim 23$  K above the reported cloud point for the same copolymer composition diluted in pH 8 TRIS buffer, as detected by UV/VIS spectroscopy.<sup>38</sup> This observation is attributed to the effect of salts contained in the buffer on the electrostatic interactions between the copolymer and water as reported recently for various thermoresponsive polymers.<sup>176</sup>

### 3.4.2 Effect of UV-Irradiation on the Hydration of P (TEGA-co-SPA) Films below and above the LCST

The P (TEGA-co-SPA) liquid thin film adsorbed onto silica appears almost transparent under visible light, but switches to deep purple upon UV irradiation (Figure 3.5, bottom part). The deep purple color of the liquid thin film upon UV irradiation originates from the absorption of the UV photons causing a breakage of C-O Spiro bonds in an excited singlet state, yielding the colored Merocyanine (MC) form.

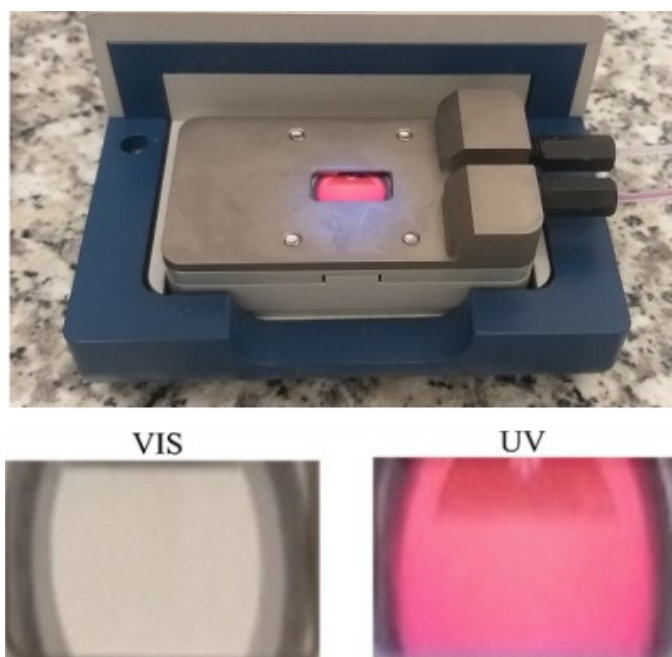


Figure 3.5 Photos taken by a normal camera of the experimental setup where the P (TEGA-co-SPA) solution is flowing on the SiO<sub>2</sub> sensor and UV light is applied through the QCM window module (top). Effect of illumination on the P(TEGA-co-SPA) liquid film color (bottom).

Due to the physisorption of the copolymer in our case, the chains of MC are made to rearrange in a way that the ethylene oxide groups point towards the solution. This may stabilize the Merocyanine form via hydrogen bonds.

To illustrate, we selected different temperatures for isothermal treatment with and without illumination below and above the LCST when investigating with QCM-D. Figure 3.6a shows the effect of switching from visible to UV light irradiation on  $\Delta f_3/3$  as a function of time at 19 °C, 35 °C, 45 °C, 50 °C; and 50 °C when the sensor was not irradiated with UV light, respectively.<sup>168</sup>

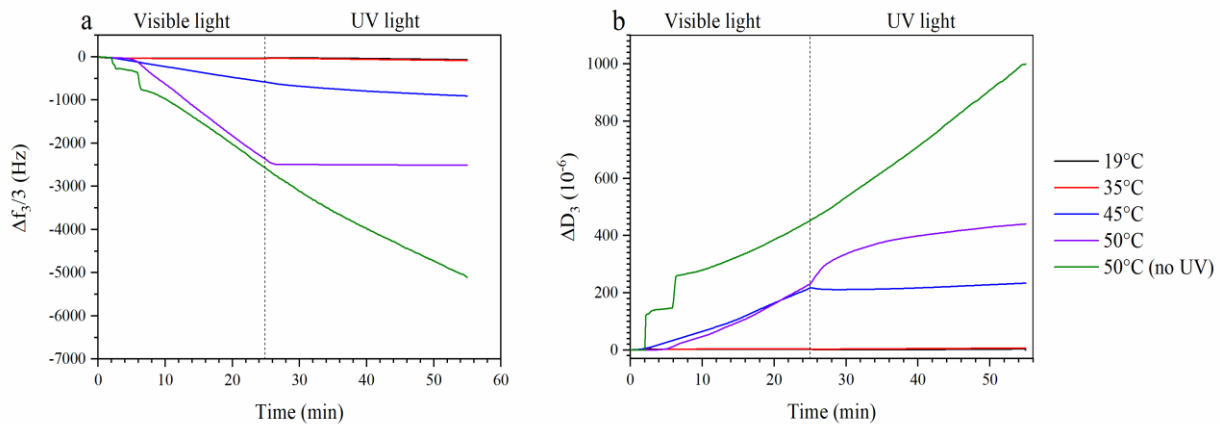


Figure 3.6 Variation of  $\Delta f_3/3$  (a) and  $\Delta D_3$  (b) versus time of *P(TEGA-co-SPA)* at the silica-water interface at a constant temperature.

At 19 °C and 35 °C, the introduction of the copolymeric solution inside the window cell causes an initial frequency decrease (mass increase) followed by a slower frequency decrease as the system saturates at -31 Hz and -40 Hz, respectively. Starting at 25 min, the sensor surface was irradiated with UV light, what caused a marginal increase in  $\Delta f_3/3$  of a few Hz, followed by a linear decrease in the frequency in the next several minutes, see Figure 3.7a.

In comparison, when there is no light switch at 19 °C,  $\Delta f_3/3$  and  $\Delta D_3$  signals do not show any significant change, (see Figure 3.7a). The spike of  $\Delta f_3/3$  occurring immediately after illumination was attributed to the effect of UV light on the crystal (see section 2.1.6). The shallow linear decrease in the frequency shift is probably due to an increase in acoustic thickness as the

copolymer chains swell. A similar result was observed in a previous study,<sup>168</sup> where P(NIPAAm-co-SPA) thin films were illuminated with a UV lamp at 19 °C.

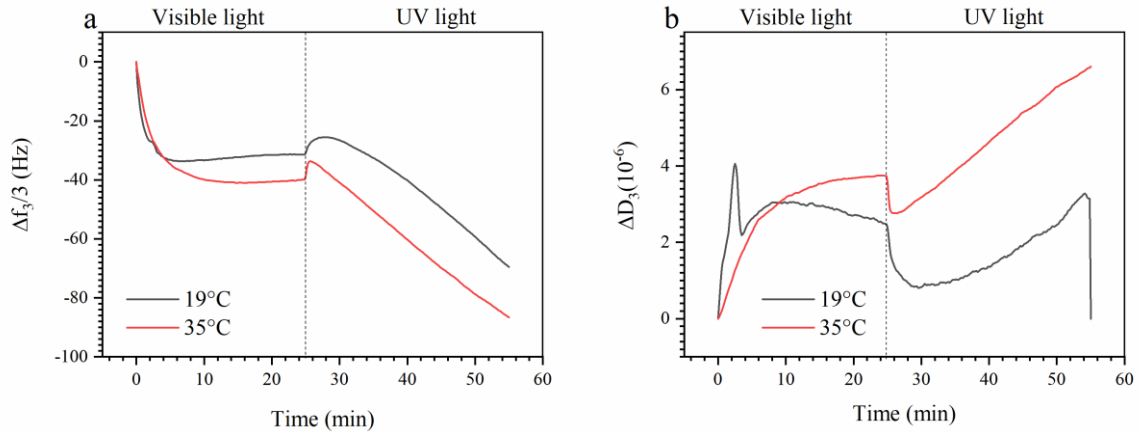


Figure 3.7 Variation of  $\Delta f_3/3$  (a) and  $\Delta D_3$  (b) versus time of P(TEGA-co-SPA) at the silica-water interface at 19 and 35 °C. This figure is a zoom at  $\Delta f_3/3$  in the range of 19 °C to 35 °C shown in figure 3.6.

In this material, the behavior was explained by photoinduced hydration due to the photoisomerization of the rather hydrophobic Spiropyran into the distinctly more hydrophilic Merocyanine when the thermo-responsive part of the copolymer is sufficiently hydrophilic.

At 45 °C and 50 °C,  $\Delta f_3/3$  decreases linearly once the copolymer solution is in contact with the sensor. This decrease in  $\Delta f_3/3$  is high in magnitude, reaching 0.58 and 2.38 kHz respectively after 25 min of continuous solution feed and visible light irradiation.

Interestingly, UV light illumination affects  $\Delta f_3/3$  differently at 45 °C and 50 °C. Although at 45 °C the rate of the observed decrease in  $\Delta f_3/3$  slows down and causes a deviation from linearity, it stabilizes at a constant (but very low) value at 50 °C.

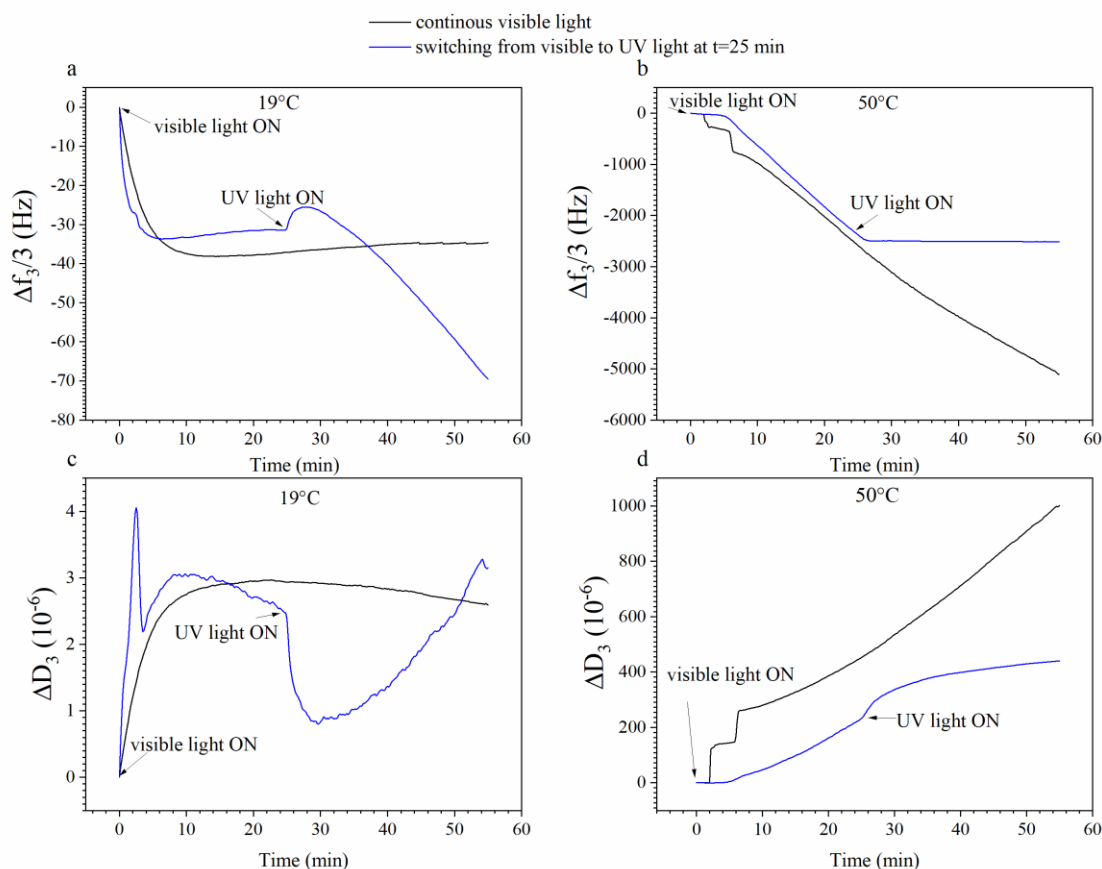


Figure 3.8 Effect of continuous visible and UV light irradiation on the resonance frequency shift  $\Delta f_3/3$  (a,b) and dissipation shift  $\Delta D_3$  (c,d) on the copolymer liquid film at 19 and 50°C, respectively. Blue curves: continuous visible illumination for 25 min then UV-light switching, black curves: continuous visible illumination during the whole experiment.

Note that when continuing visible illumination and turning UV off beyond 25 min, the observed strong decrease in  $\Delta f_3/3$  continues unaffected, indicating that UV illumination (versus, e.g., some saturation effect) does indeed play a role in the phenomenon observed at 50 °C (see also Figures 3.8b and 3.8d). We attribute this observation to a competition between PTEGA globule adsorption on the sensor surface and photoconversion of Spiropyran to Merocyanine.

When there is no UV irradiation, surface adsorption is facilitated and the observed Sauerbrey thickness increases during prolonged solution injection. This process is interrupted by the conversion of the non-polar Spiropyran to the polar Merocyanine, which enhances the stability of the solution and thereby reduces the adsorption rate. Similar observations have been made for azobenzene surfactant adsorption and desorption at the air–water interface under UV irradiation.<sup>177</sup>



Figure 3.6b shows the evolution of  $\Delta D_3$  corresponding to Figure 3.6a. At 19 °C and 35 °C,  $\Delta D_3$  shows low values in the first 25 min, suggesting that the film is forming a monolayer at the silica surface. Once the surface is irradiated with UV light,  $\Delta D_3$  increases linearly at both temperatures and reaches  $\sim 3 \times 10^{-6}$  and  $6 \times 10^{-6}$ , respectively, at 19 °C and 35 °C after around 55 min.

At the higher temperatures of 45 °C and 50 °C,  $\Delta D_3$  increases similarly (although at a much higher rate) for as long as the sensor is irradiated with visible light. Once UV illumination is switched on at these temperatures, there is a very significant effect on dissipation: at 45 °C,  $\Delta D_3$  decreases slightly and subsequently reaches a plateau, while at 50 °C,  $\Delta D_3$  apparently evolves with a square root dependence on time, which could indicate some kind of diffusive process.

Interestingly, this processes extends far beyond the time at which surface adsorption is interrupted (Figure 3.6a); we note that dissipation evolves as a convolution of swelling effects within the film, as well as adsorption from the solution, which are both affected by the two stimuli of temperature and light. When adsorption stops, conformational changes can still proceed within the film, but these would be significantly slower in their response rate due to the reduced film mobility as compared to the polymer in solution. The observed square root dependence on time corroborates this interpretation.

### **3.4.3 Dual Temperature and Light Effect on the Build-Up of P (TEGA-Co-SPA) Layers on Silica Surfaces**

Temperature ramping was carried out in order to investigate the concomitant effect of temperature and light on the conformational change of the P(TEGA-co-SPA) diluted solution during adsorption. We started by analyzing the behavior of a P(TEGA-co-SPA) thin film being formed on the QCM-D sensor surface.

Figure 3.9a shows the variation of the normalized resonance frequency shift  $\Delta f_3/3$  over a temperature range of 20 °C to 47 °C, comparing the effects of visible light irradiation and UV irradiation (365 nm). Under UV exposure, we observe an initial, slow decrease in  $\Delta f_3/3$  between 21 °C and 28 °C, which is less pronounced under visible light. This difference suggests that the sensed mass (load) increased with UV irradiation, which could be attributed to additional hydrodynamically coupled water inside the adsorbed film in this temperature range. Any masses retrieved by QCM-D are non-specific, that is, both polymer and water (or solvent in general) bound

in the adsorbed films are detected. For instance, in case of protein adsorption, an additional molecular weight increase of  $\sim 30\%$  was reported and attributed to water bound to a protein molecule in solution.<sup>138</sup>

In our present case, we believe that the photoisomerization of the Spiropyran with UV irradiation results in a higher trapped amount of water inside the layer of P (TEGA-co-SPA) when it is sufficiently hydrophilic. For visible light irradiation, we note a change in the slope of  $\Delta f_3/3$  over T at  $\sim 28^\circ\text{C}$ ; under UV irradiation, such a change is not observed until a much higher temperature of near  $\sim 47^\circ\text{C}$ . We attribute this change of the slope to a sudden increase in the amount of the adsorbed copolymer chains at the sensor surface.

As we approach the LCST, one should expect that the copolymer is gradually collapsing and releasing water. This dehydration should express as increased  $\Delta f_3/3$  values as reported, e.g., for PNIPAAm layers adsorbed on a hydrophobic gold surface.<sup>164</sup>

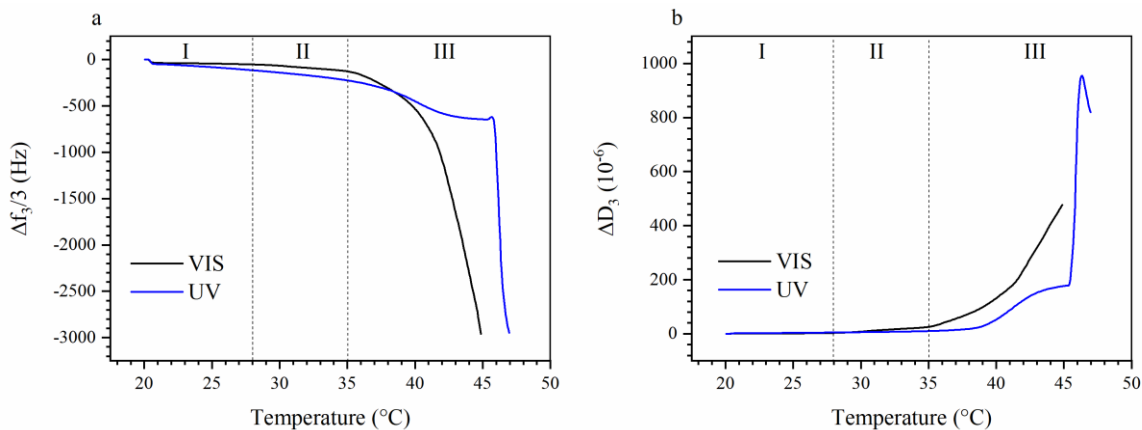


Figure 3.9 Variation of normalized  $\Delta f_3/3$  as a function of temperature upon irradiation of P(TEGA-co-SPA) copolymers at the silica-water interface, the copolymer was introduced at  $T=20^\circ\text{C}$  (a), variation of  $\Delta f_3/3$  as a function of temperature of the same solution. Blue curves, upon illumination with visible light (b). The labels (I-III) mark the regimes of adsorption and film response discussed in the text.

However, we must note again that we do not observe the properties of a preexisting film, but the process of a film being formed *in-situ* from a photo-thermoreponsive solution. Thus, we argue that the observed decrease in  $\Delta f_3/3$  (despite water release) is a result of polymer adsorption and film growth, which dominates over any water release in particular, as the hydrophilic coil to

hydrophobic globule transition already occurs in solution, and only to a smaller extent within the film.

At 35 °C,  $\Delta f_3/3$  of the visible light irradiated sensor decreases drastically which we relate to the liquid–liquid phase separation. Interestingly, this large decrease in  $\Delta f_3/3$  occurs at about 4–8 K lower than the reported cloud point temperature of the same copolymer in TRIS buffer solution when irradiated with 540 nm visible light.<sup>38</sup> This difference between the cloud point temperature detected by UV/Vis spectroscopy and the phase transition temperature determined acoustically on a surface suggests that the confinement affects the coil-to-globule transition of the copolymer at the interface.

At 38.3 °C, we note a change in the feature of  $\Delta f_3/3$  over T of the UV irradiated solution, with an initial acceleration (higher negative slope) of adsorption, followed by a deceleration and a plateau reaching up to ~45 °C.

This is in line with our isothermal observations summarized in Figure 3.6a, where UV irradiation at higher temperature decelerates film adsorption up to a certain extent. Here, the deceleration sets in just before LCST as would be the case under visible illumination.

At 45.7 °C, we observe a sudden, strong acceleration of the adsorption rate, with a sharp decrease in  $\Delta f_3/3$ . This is attributed to the delayed P (TEGA-co-SPA) LCST in the aqueous solution, shifted to a higher temperature due to the increase in the hydrophilicity of the polymer induced by the 365 nm UV light irradiation. A similar temperature shift was also observed for the bulk material using UV-Vis spectroscopy, although the transition temperature happening at the silica-water interface was lowered by 2–3K.<sup>38</sup>

The dissipation data corresponding to the observed cases of  $\Delta f_3/3$  is displayed in Figure 3.9b. Here, too, we distinguish the three regions of (I)  $T < 28$  °C, (II)  $28$  °C  $< T < 35$  °C, and (III)  $T > 35$  °C (marked as I–III in Figure 3.9a and Figure 3.9b).

Again, an increase in dissipation correlates to the enhancement of coupling between water molecules and polymer chains due to the photo-induced hydration under UV illumination (region I). Moreover, there is a significant difference of the sensed masses on the sensor, depending on the type of irradiation.

In the temperature range of 21 °C to 28 °C,  $\Delta D_3$  increases by a factor of about two, that is, from  $1.6 \times 10^{-6}$  to  $3.3 \times 10^{-6}$  and from  $2.2 \times 10^{-6}$  to  $4.9 \times 10^{-6}$  for the visible and UV irradiated film, respectively.

In the temperature range of 28 °C to 35 °C,  $\Delta D_3$  shows a stronger increase for the solution exposed to visible light as compared to the one irradiated with UV light. This observation corroborates our interpretation that the competition between dehydration and adsorption already started several degrees below the commonly reported LCST.

At 35 °C,  $\Delta D_3$  increases dramatically, in agreement with the resonance frequency data. According to the change of slope at  $\sim 38$  °C, the dehydration also happens gradually under UV light. In this case, the delayed phase transition reflects in the over-damping of the layer happening at  $\sim 46$  °C, where the magnitude of  $\Delta D_3$  reaches  $953 \times 10^{-6}$ .

Examining the change of the energy dissipation as a function of the negative frequency shift allows us to eliminate the temperature as a variable and to focus on the effect of the light irradiation on the viscoelastic properties during layer build-up.<sup>178</sup>

Figure 3.10a and Figure 3.10b show the evolution of  $\Delta D_3$  as a function of  $-\Delta f_3/3$ , respectively, for visible and UV irradiated P (TEGA-co-SPA) at the silica–water interface. Interestingly, both properties are not directly proportional to the surface coverage and the adsorbed film does not evolve in the same way whether it is irradiated with visible or UV light.

Under visible light illumination, the change in dissipation is smaller than the change in resonance frequency whereas under UV light, it strongly exceeds the frequency change. A linear correlation between both properties is found only in the onset region of film formation, i.e., within 0 to 550 Hz (Vis) and 0–320 Hz (UV), where surface coverage of the layer is still low

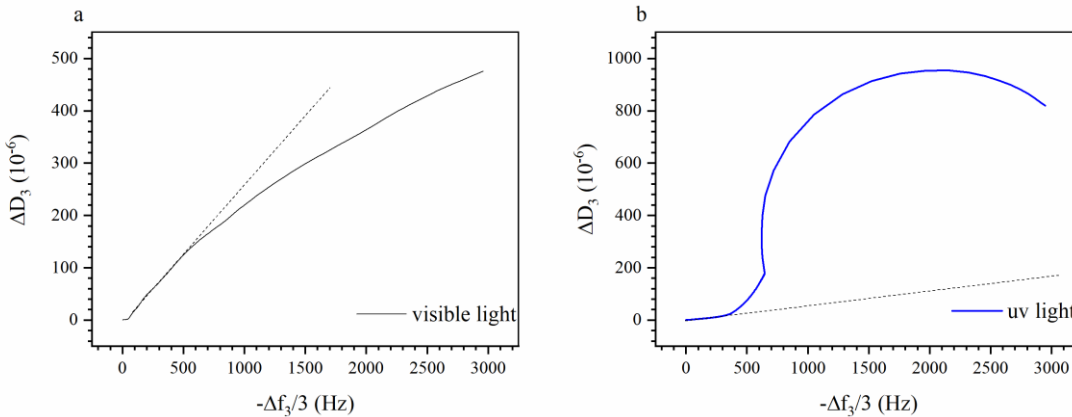


Figure 3.10 Variation of  $\Delta D_3$  as a function of  $-\Delta f_3/3$  when the sensor is continuously exposed to visible light (a), (b) variation of  $\Delta D_3$  as a function of  $-\Delta f_3/3$  when the sensor is irradiated with UV light (b). Blue curves: upon UV illumination, black curves: upon visible illumination.

In this range, the hydrodynamic thickness is expected to be small, and the number of polymer molecules adsorbed physically through trains, loops, and tails is negligible.<sup>179</sup> So long as the dissipation values are low and  $\Delta D_3$  increases linearly with  $-\Delta f_3/3$ , we assume that the viscoelastic properties of the film remain unchanged and the parameter variations are solely due to continuous adsorption. The occurrence of such a region was similarly observed by QCM-D for different adsorbing systems, including polyelectrolytes,<sup>180</sup> and homopolymers on gold.<sup>164</sup>

Beyond the linear onset regime, there are pronounced effects of temperature and illumination. For the visibly irradiated surface, we observe a decrease in dissipation as the coverage of the surface is increasing. This evolution can be explained by the densification of the film once the surface is saturated.

For the UV irradiated layer, we observe a strong excess in dissipation which saturates at about 2000 Hz. The spiral shape is similar to previous observations made on polystyrene brushes in cyclohexane.<sup>181</sup> It indicates that the deposited film interacts more pronouncedly with the bulk solution, resulting in enhanced dissipation when the copolymer is in its polar (MC) state. In this case, we should expect a film with lower density as UV light leads to decelerated absorption and a polarity change, therefore the adsorbate has less time to rearrange itself as when its only irradiated with visible light.

The LCST of dilute P(TEGA-co-SPA) depends on illumination conditions. Adsorption kinetics and film growth at the silica–water interface can, therefore, be controlled through temperature and illumination conditions, relying on the thermally induced transition from hydrophilic coil arrangement to hydrophobic globules of the PTEGA components, and on the transition in polarity of the SPA-MC component controlled through illumination.

Similarly, the film itself responds to thermal as well as optical stimuli through variable dissipation of acoustic excitation. Our results show that the coil-to-globule transition temperature is lower in diluted samples exposed to an adsorbing surface as compared to the solution.

The conformational state of the adsorbed polymer chains is controlled by surface confinement and kinetics; whereby non-equilibrium conformational states could be frozen for long times after adsorption.<sup>182</sup>

A present assumption is that non-equilibrium effects originate from the polymer density and conformation at the interface of the adsorbing surface and the surrounding polymer solution or melt above its glass transition,<sup>183</sup> which are kinetically frozen as a result of adsorption. For example, the slow rejuvenation of compressed polyethylene oxide PEO adsorbed on mica was found to be caused by the low mobility of the polymer chains in their adsorbed state.<sup>184</sup>

Glassy dynamics of thermoresponsive, adsorbed polymers were investigated on solid substrates, e.g., latex particles in water. When the temperature was raised above the LCST temperature, PNIPAAm underwent a conformational transition from adsorbed loops to globules.<sup>185</sup> This transition process was slow: the relaxation time was found to vary between a few hundred to several thousand minutes.<sup>186</sup> Notwithstanding the difference in chemical structure between PNIPAAm and PTEGA, we assume that the difference between the bulk and surface LCST temperatures found here for P(TEGA-co-SPA) is likely due to similar kinetic considerations.

Another interesting aspect of the non-equilibrium nature of the adsorbed layer is related to the interplay between adsorption and wetting. The evolution of the frequency and dissipation shift as functions of temperature illustrate experimentally the surface-driven phase separation in polymer solutions, as predicted by Cahn.<sup>187</sup>

Water and the P(TEGA-co-SPA) copolymer form a single solution phase at low temperatures. When the temperature of the system is increasing and, at the same time, the interaction between the solvent and the polymer is altered via optical stimuli,<sup>188</sup> we expect the system to first approach the wetting point at which the mixed and the demixed states of the binary mixture coexist.

Further increase in temperature results in phase separation. Thereby, the phase with lower interfacial energy wets the silica surface.<sup>189</sup> Our QCM data supports this hypothesis, similar to previous observations on the adsorption of P(NIPAAm) on hydrophobic gold surfaces.<sup>164</sup>

Although it is often claimed that thin hydrogel films are hydrophobic above their LCST, we show that SPA-copolymerization provides a means to circumvent this issue. For example,<sup>168</sup> UV light exposure was found to have no effect on the hydration of P(NIPAAm) containing 2.5 mol% SPA when the temperature was above the LCST. This was explained by confinement of the chromophore within isopropyl groups and the hydrophobic backbone of P(NIPAAm).

In our case, we found that UV light decelerated the growth of the wetting layer at 45 °C and 50 °C due to the competition between copolymer globule adsorption and photoconversion of Spiropyran to Merocyanine facilitating desorption (see the expected mechanism in Figure 3.11).

In the absence of UV irradiation, the copolymer escapes from the solvent toward the silica surface, and thickness of the wetting layer increases as long as the feeding solution is continuously injected. However, when illuminating with UV light, Spiropyran rapidly converts to the polar Merocyanine, leading to layer swelling and, eventually, globule desorption. The further difference between our observations and previous studies on P(NIPAAm-co-SPA) are attributed to different deposition techniques, major differences in the amount of the chromophore and even the difference in molar mass of the employed copolymer, which sets variable constraint on polymer conformation and deposition kinetics.

A hydrogel film of P(NIPAAm) deposited by spin coating may delaminate from the surface due to osmotic stress caused by interaction with water molecules,<sup>190</sup> even above LCST. On the other hand, P(TEGA-co-SPA) surface rearrange both below and above the LCST; the isopropyl groups

concentrate near air or other hydrophobic phases, whereas ethylene oxide groups rather orient towards water.<sup>191</sup>

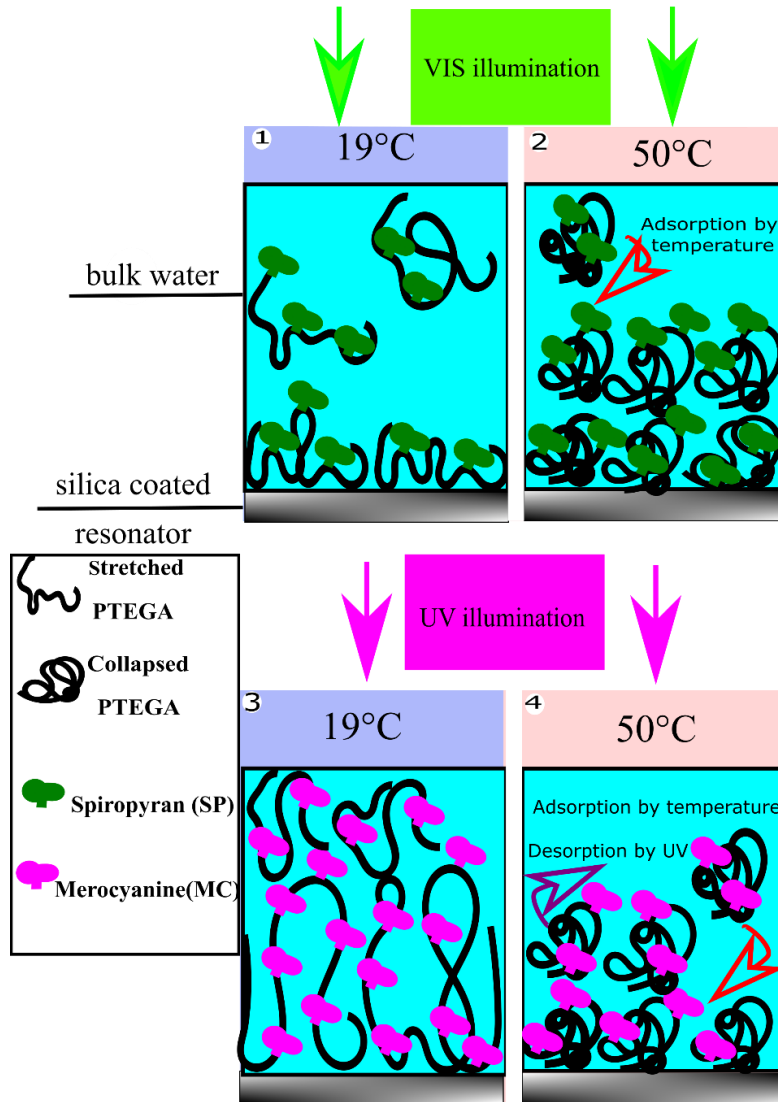


Figure 3.11 Schematic description of dual-responsive copolymer behavior of  $P(\text{TEGA-co-SP/MC})$  at the silica-water interface during in-situ observation of adsorption with QCM-D. Four possible states can be obtained under the effect of switching from visible light illumination to UV light illumination below LCST (top) and above LCST (bottom).



### **3.5 Conclusion**

The conformational change of a thermal and light responsive copolymer layer of P (TEGA-co-SPA) on silica surfaces was investigated using quartz crystal microbalance with dissipation monitoring (QCM-D).

First, we elucidated the effect of isothermal UV light illumination on the hydration state of the liquid film below and above its LCST.

Second, we showed that the phase separation temperature of the confined copolymer at the interface shifts to lower temperatures, namely 4–8 K lower compared to the cloud point temperatures as reported by UV/VIS spectroscopy in dilute aqueous solution. We attribute this difference to the formation of non-equilibrium adsorbed multilayers on the silica surface.

Finally, we demonstrated that the built-up wetting layer displays variation of its viscoelastic properties with temperature and illumination conditions.

## 4. Kinetic Study of Poly(N-isopropylacrylamide) Glassy Layers

### 4.1 Summary

Liquid-liquid phase separation of polymer solutions can be a route to obtain glasses when critical conditions of temperature and concentration are reached.

In this work, we studied the isothermal deposition kinetics of poly(*N*-isopropylacrylamide) P(NIPAAm) layers *in situ* in contact with a silica-coated resonator, using Quartz Crystal Microbalance with dissipation monitoring, QCM-D.

We found that the film formation follows a two-stage kinetic model, where the first stage is a slow process fitting a stretched exponential function with the exponent  $\beta$  always larger than 1 (indicating superdiffusion whereas, the second stage is a fast process and fits a normal exponential function (revealing simple diffusion).

The associated relaxation times of these two processes show anomalous dependence on temperature and concentration below and above the lower critical solution temperature (LCST), inferring a possible glasslike feature of the collapsed polymer globules forming the adsorbed film.

Moreover, the viscoelastic analysis of the polymer adsorption isotherms as functions of the overtone order shows a dramatic increase of the resonance frequency and energy dissipation shifts around the LCST.

Through this analysis we showed that the change of the viscoelastic properties of the layer is possibly related to the diffusion anomaly.

Finally, we corroborate the results of our isothermal analysis by showing that P(NIPAAm) layers undergo a colloidal glass transition on silica surfaces upon non-isothermal treatment.

Our findings show that QCM-D is a useful tool to study the anomalous dynamics of glassy materials in liquid phases.

## 4.2 Introduction

Poly(N-isopropylacrylamide) P(NIPAAm) is a thermosensitive polymer which displays a conformational change as a function of temperature when the quality of solvent is changed from good to poor.

This polymer is soluble in water as an expanded coil but collapses to globule or phase separates when the temperature of the medium is raised above its lower critical solution temperature (LCST), that is above  $\sim 32$  °C.<sup>24</sup>

Several studies show that the material could be used as a model to study glassy dynamics in colloidal suspensions due to its ability to change the particle volume fractions and the interparticle interactions from repulsive to attractive by temperature.

Previously, Mattson *et al.* showed that P(NIPAAm) microgel suspensions could be employed to explore the fragility/strength of glass formers.<sup>192</sup>

Using dynamic light scattering (DLS), it has been found that these materials could be classified as “strong” glass formers when they are sufficiently compressible. This classification has been assumed due to the exponential increase of their relaxation times together with their volume fraction in analogy to “strong” temperature-dependent glasses.

Furthermore, this comparison was correlated with the ability of soft particles to adjust their volume by swelling-deswelling transition.<sup>193</sup> Another interesting feature of P(NIPAAm) microgel suspensions (as compared to hard spheres and other soft particles) is their capacity for overpacking, leading to an effective volume fraction  $\phi_{\text{eff}}$  that is higher than unity in addition to dramatic changes in elastic properties.<sup>192,194</sup>

More recently, the dynamical behavior of microgels of interpenetrated P(NIPAAm) and Poly(acrylic acid) (PAAc) networks in deuterated solvent (D<sub>2</sub>O) have been investigated through the same technique as a function of temperature, pH and concentration across the volume phase transition (VPT) happening at 32°C.<sup>195</sup>

It was found that the dynamics of these microgels above the VPT slowed down in D<sub>2</sub>O, especially for the highest concentration at pH 7 when compared to water. The application of the fragility

universal framework for the same studied system reveals that increasing the temperature across the VPT results in a transition from soft-strong to stiff-fragile behavior.

The slow dynamics of P(NIPAAm) particles was not only investigated in concentrated microgels suspensions but also in densely packed nanogels.<sup>196</sup> In particular, the behavior of concentrated core-shell nanoparticles composed of a silica core and a P(NIPAAm) shell suspended in water was investigated by X-ray photon correlation spectroscopy (XPCS).

The studied system shows dependence on temperature associated with anomalous diffusion regimes: one subdiffusive regime up to 32°C where the relaxation time of the particles decreases monotonously with temperature, one intermediate regime between 32 and 36°C with strong relaxation time decrease and one superdiffusive regime where the relaxation time increases with temperature by several orders of magnitude when temperatures are higher than 37°C.

Binary solutions of P(NIPAAm) linear chains in water can also show slow dynamics similarly to microgels and nanogels. It is believed that the kinetic slowdown of a phase separating solution is due to the interference of the glass transition of the polymer-solvent system with the liquid-liquid phase separation, in particular for common amorphous glassy polymers such as polystyrene.<sup>8</sup>

When the system is quenched to a temperature that provokes a liquid-liquid phase separation, two distinct phases are formed: a polymer-rich and a polymer-poor phase. If the concentration of the formed polymer-rich phase reaches the critical conditions to form a glass, the demixion process becomes; slow, hindering the further coalescence of the resulting globules.

The kinetic arrest of P(NIPAAm) above the LCST was attributed to the effect of temperature rather than to the concentration, as Afroze *et al.* claim that the dehydration of the P(NIPAAm)-rich phase is stopped when the concentration reaches a limiting value at certain temperatures, which does not allow further densification of this phase.<sup>197</sup> However, as of this writing it is uncertain whether LCST phase separation is dependent on concentration in the case of P(NIPAAm).

For a P(NIPAAm)/water system in contact with a surface, one expects that liquid-liquid phase separation creates wetting layers which may form glass on the surface at certain temperatures and concentrations.

Quartz crystal microbalance with dissipation monitoring (QCM-D) is one of the emergent techniques employed to characterize thermosensitive soft layers. To date, QCM-D has been used

to determine the LCST values of P(NIPAAm) thin films depending on the deposition method, whether *via* “grafting on”<sup>162,198</sup> or initiated chemical vapor deposition (iCVD).<sup>135</sup>

The same surface sensitive technique has been employed to investigate the kinetics of adsorption of P(NIPAAm) on different modified and unmodified surfaces. The physisorption of this material on hydrophobic gold at 31°C (just below the LCST) suggests that the deposition of P(NIPAAm) layers happens *via* growth in thickness rather than by densification.<sup>164</sup>

In another adsorption study on unmodified gold surface, the kinetics of P(NIPAAm) adsorption showed dependence with temperature and concentration below LCST but no dependence on these two parameters above LCST.<sup>199</sup>

The growth mechanism of monolayers ( $T < \text{LCST}$ ) and multilayers ( $T > \text{LCST}$ ) in this case was attributed to densification. As the dissipated energy can be monitored *in situ* using QCM-D, most of the aforementioned studies have emphasized the effect of temperature on the viscoelastic properties and the approximate thickness of the adsorbed layers, but investigate neither the dynamic of the system nor the deswelling kinetics.

However, it has previously been shown that QCM-D can be used to give an additional thermodynamic insight of surface-bound P(NIPAAm) film using a two-state coil-to-globule model.<sup>200</sup> The model considers solely the equilibrium between the swollen coil and collapsed globule states without “intermediates” to determine the enthalpy of the collapse of the coils into globules.

In our study, we claim that the formation of physically adsorbed P(NIPAAm) layers on silica may be studied from a non-equilibrium perspective. We argue that our system is more likely to involve a transient metastable state in addition to the coil and globule states (deswelling).

This hypothesis stems from two considerations: the deposition method and the thermal treatment.

First, physisorption has fewer confinement constraints on the polymer chains to collapse stepwise (step-by-step rather than continuously).<sup>92</sup>

Second, it is widely accepted that upon quenching a binary system such as P(NIPAAm)/water by a sudden temperature change, the system is out of equilibrium.

In order to reach a new equilibrium state, the system may progress through metastable intermediate states,<sup>201</sup> though our two-step model only considers a single intermediate state. This intermediate state is a trapped structure that has a local free energy minimum and is separated from the global free energy minimum conformation by an energy barrier. The presence of metastable states is theoretically associated with slow diffusion and glasslike feature of collapsed polymers.<sup>202</sup>

To gain a better insight into formation of glassy layers in a wet medium, we present our recent kinetic study in the formation of P(NIPAAm) thin films using Quartz Crystal Microbalance with Dissipation Monitoring (QCM-D).

We present a study of the anomalous dynamics of polymeric systems in thin films using QCM-D, shed more light on the step-wise nature of layer formation and investigate the dependency of temperature induced transition and concentration on the dynamics of the system.

In addition, we study the effect of the overtone order on the viscoelastic properties of the adsorbed layers as a function of temperature and concentration below and above the LCST.

Finally, we corroborate the results of the isothermal study with the effects of non-isothermal treatment on the glassy dynamics of the adsorbed layers.

## **4.3 Materials and Methods**

### **4.3.1 Materials**

Poly-N-isopropylacrylamide (P(NIPAAm); Merck, Darmstadt, Germany) was used, with an average molar mass of  $M_n=19.000$  g/mol with a polydispersity index of  $\mathcal{D}=3.6$ , as determined by size exclusion chromatography with triple detection. Three aqueous solutions of P(NIPAAm) with a concentration of 0.04, 0.009 and 0.0004 wt.% respectively were prepared by diluting the polymer in deionized water. Deionization was done using a Thermo Scientific Barnstead MicroPure water purification system to a resistivity of  $18.2 \text{ M}\Omega \text{ cm}^{-1}$ .

### **4.3.2 X-Ray Diffraction**

To characterize the P(NIPAAm) powder, diffraction measurements were performed using MiniFlex XRD (Rigaku, Neu-Isenberg, Germany) which has a  $\text{Cu K}\alpha$  X-ray source with a wavelength of  $1.54059 \text{ \AA}$  and equipped with a D/tex Ultra detector. The voltage and current of the

X-ray tube were set to 40 kV and 50 mA, respectively. The diffraction signal was collected in the  $2\theta$  range of  $5^\circ$ – $75^\circ$  with a step size of  $0.02^\circ$ .

### 4.3.3 Differential Scanning Calorimetry

DSC analysis was performed using an STA 449 F1 instrument (Netzsch, Selb, Germany). The measurement was made under  $20 \mu\text{l}/\text{min}$  nitrogen flow with 11.1 mg of P(NIPAAm) powder heated between 25 and  $400^\circ\text{C}$  at a scanning rate  $1\text{K}/\text{min}$ .

### 4.3.4 Dynamic Light Scattering

DLS measurements of the 0.04 wt.% P(NIPAAm) solution were performed using an ALV Laser CGS3 Goniometer (ALV GmbH, Langen, Germany) equipped with a He-Ne laser ( $\lambda = 633 \text{ nm}$ ) and an ALV-7004/USB FAST correlator. All DLS measurements were performed between 25 to  $65^\circ\text{C}$ .

To determine the hydrodynamic radius, three measurements of 30 s each were performed at an angle of  $90^\circ$ . The analysis of the obtained correlation functions was performed using the correlator software (Correlator 3.2 beta 1). DLS measurements of the polymer solutions can be realized at different temperatures in order to study the LCST phase transition in the diluted regime

### 4.3.5 QCM-D Experiment

QCM-D measurements were performed using a flow module mounted on the QCM sensor (Q-sense E1, Biolin Scientific, Västra Frölunda, Sweden). AT-cut quartz crystal sensors coated with a 50 nm silicon dioxide layer (fundamental resonance frequency of typically  $\sim 4.95 \text{ MHz}$ , sensor area  $1.54 \text{ cm}^2$ ) were purchased from the same company.

Prior to experiments, the quartz sensor was cleaned by soaking in a 2 vol% sodium dodecyl sulfate SDS solution for 30 min, rinsing with ultra-pure water, blow-drying with a gentle nitrogen flow and, finally, exposing to a UV/ozone cleaner for 15 min.

To study the isothermal deposition of P(NIPAAm) on silica surface, all experiments were performed at constant temperature in the steady flow mode by first purging with ultra-pure water for 59 min then stopping the pump for 1 min and start flowing the P(NIPAAm) solution at  $150 \mu\text{l}/\text{min}$  for 1 hour.

However, to investigate the non-isothermal deposition, the temperature was ramped between 20 °C and 40 °C by applying heating-cooling processes at different rates ranging from 0.05 to 0.5 K/min. The polymer solution was introduced to the chamber at 10  $\mu$ l/min flow rate at a temperature of 20 °C  $\pm$  0.02 °C after 30 min of stabilization with ultra-pure water at 19 °C under same flow rate. Changes in the (acoustic) load of the sensor caused by changes in the P(NIPAAm) solution can be retraced from changes in the oscillation behavior monitored via frequency and dissipation shifts in comparison to a reference state.

As previously mentioned, several oscillation overtones of the quartz crystal sensor exposed to the P(NIPAAm) solutions were acquired, although the third overtone was generally selected for further analysis because of its level of energy trapping at this particular overtone when operating in liquids.<sup>143</sup>

During each run, changes in the resonance curves of the third, fifth and seventh overtone were continuously monitored and evaluated each 10 seconds. The main resonance parameter under investigation was the change in the shift in resonance frequency normalized to the overtone  $\Delta f_n/n$  being related to the mass of the adsorbate and the dynamically coupled liquid.<sup>144</sup>

The acquired datasets were corrected for each sensor using a temperature sweep in pure water for reference as in the previous chapter. This temperature correction was carried out by subtracting the calibration curve (pure water on sensor) from the one obtained in the presence of the dissolved polymer. In case of non-isothermal deposition measurements, 20 °C was considered as the state where the areal mass density is 0.

## **4.4 Results and discussions**

### **4.4.1 P(NIPAAm) characterization in powder and in solution**

Structural characterization of P(NIPAAm) has been carried out in order to determine the initial structure of the polymer prior to deposition. Figure 4.1a and 1.b show the different structural and thermal characteristics of P(NIPAAm) powder. We observe from the XRD diffractogram two wide diffraction peaks, one at  $2\theta=7.2^\circ$  and another at  $2\theta=19.2^\circ$ . The observed broad bands suggest that this material is amorphous.

Moreover, the DSC curve of the P(NIPAAm) powder correlates the expected disordered structure by the presence of two steps in the baseline in the endothermic direction, occurring at 137.6 °C and



160.7 °C. This phenomenon assumed in general to be the signature of a temperature dependent glass transition,<sup>203</sup> and even multiple glass transitions were reported for P(NIPAAm) homopolymer, being explained by irregularities of polymer network or retention of unreacted monomers.<sup>204</sup> Such irregularities of polymer network can be accessed via DLS.

Figure 4.1c shows the evolution of the hydrodynamic radius  $r_h$  of the P(NIPAAm) chains dissolved in water at a concentration of 0.04 wt% as a function of the temperature between 20 °C and 65 °C at 0.4 K/min heating rate.

Between 20 °C and 32.4 °C, the thermosensitive polymer chains exhibit a small hydrodynamic fluctuation averaging around 3 nm. However, when the temperature reaches 32.4 °C, we see a dramatic increase of  $r_h$ . At higher temperatures, we note that the hydrodynamic radius reaches 268 nm at 34.4 °C and decreases slightly at higher temperatures to 194 nm at 65.5 °C.

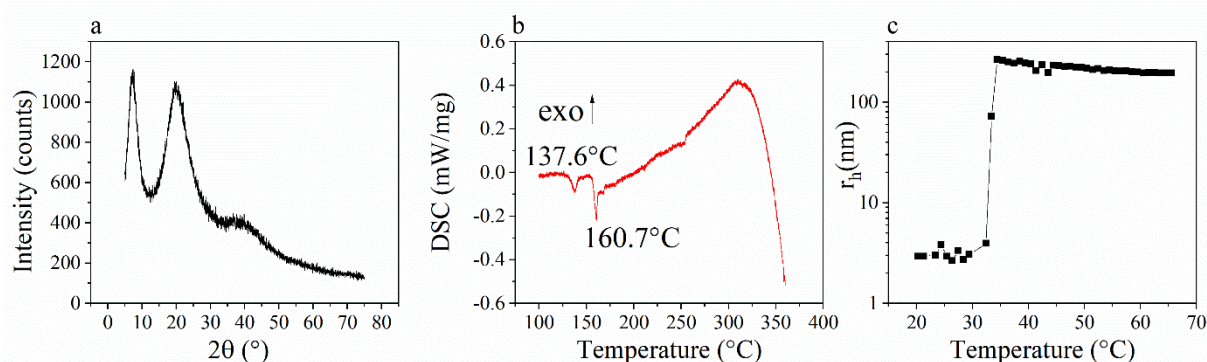


Figure 4.1 XRD diffractogram of P(NIPAAm) powder at room temperature (a). DSC curve of P(NIPAAm) powder of heating scan between 100 °C and 370 °C at 1K/min (b). DLS measurement of 0.04 wt% P(NIPAAm) aqueous solution during temperature increase between 20 °C and 65 °C (c).

A comparison between our DLS results and those reported in literature<sup>155,205</sup> shows both similarities (appearance of mesoglobules) and differences (the hydrodynamic radius shrinks instead of remaining stable or increasing between 25 and 33°C).

A decrease in hydrodynamic radius by 30% taking place between 25 °C and 33 °C with no observed aggregation has been reported.<sup>155</sup> for highly diluted aqueous solution of P(NIPAAm) of  $10^{-4}$ - $10^{-5}$  wt%,  $\bar{M}_w=2\times 10^6 \dots 9\times 10^6$  g/mol and  $\bar{D}\leq 1.2$ . At temperatures above 33.5 °C,

mesoglobules have been observed originating from chains aggregating into dense, long lived, spherical particles.<sup>16</sup>

It is commonly believed that the mesoglobules' formation in dilute solutions results from a competition between polymer chain intermolecular association and chains contraction (loss of translational entropy) and therefore corresponding at least to one local minimum of the free energy.<sup>206</sup>

In our study conducted in 25 °C-65 °C temperature range, the size of these mesoglobules initially increases upon reaching LCST and decreases to a stable level which can be assumedly observed above 60 °C in our investigation using a much higher concentration and different  $M_n$  (at 0.04 wt%). The formerly reported stability was interpreted as a result of low collision frequency between the formed spherical particles in dilute solutions.<sup>207</sup>

Table 4.1 shows several mesoglobule sizes from different works as a function of heating rate, concentration and molecular weight which indicate a large variation.

*Table 4.1 Comparison between the size dependence reported in literature of mesoglobules with heating rate, temperature, concentration and our own results of P(NIPAAm) aqueous solutions measured with DLS*

	Literature						This Work		
<b>Heating rate (K/min)</b>	0.05	0.1	0.5	0.04	0.001	0.001	0.4	0.4	0.4
<b>Size mesoglobule (nm)</b>	~46	~39	~31	~128	~86	~26.5	~2.9	~268	~194
<b>Temperature °C</b>	37	37	37	20	30.6	35.9	20	34.4	65.5
<b>Concentration g/cm<sup>3</sup></b>	$1.2 \cdot 10^{-4}$			$6.7 \cdot 10^{-7}$			$4 \cdot 10^{-3}$		
<b>Reference</b>	155			208					

We believe that in our study the stable conditions were not completely reached due to a much higher concentration of P(NIPAAm) polymer chains. Based on another work<sup>205</sup> where extremely diluted P(NIPAAm) solution was tested, the initial decrease in  $r_H$  was found to take place at two temperature ramps: between 20 and 30.6 °C, and then between 30.6 and 32.4 °C followed by stable values at temperatures than 35 °C. While several authors claimed that the mesoglobule size above LCST is not affected by temperature<sup>155,172</sup> others suggested that it depends on concentration and heating rate,<sup>209</sup> which is supported by our observations.

#### **4.4.2 Isothermal kinetic study of glassy wet layers on P(NIPAAm) on silica surface**

After showing the initial characterization in powder and solution, we are now interested in studying the isothermal deposition of P(NIPAAm) as thin film.

Figure 4.2 displays the evolution of the negative frequency shift  $-\Delta f_3/3$  as a function of time upon flowing P(NIPAAm) aqueous solution at different temperatures ranging from 24 °C to 36 °C. However, viscoelastic properties expressed in term of dissipation changes are nonlinear with water content which may make the kinetic study more complex at this stage.

In this part, we will focus on the frequency shifts (acquired at the third harmonic) because the fraction of collapsed polymer chains scales linearly with the amount of released water during the dehydration process, and can therefore be considered as a rigid mass load.<sup>210</sup>

At temperatures below the LCST~32 °C, we note an increase of  $-\Delta f_3/3$  in a sigmoidal shape as well as growth of the final values proportionally to temperature, in particular between 24 °C and 30 °C. The estimated equivalent Sauerbrey thickness from equation (2.5) increases from 1.8 nm to 3.1 nm at 24 °C and 30 °C respectively, assuming a temperature-independent density of P(NIPAAm) of 1.1 g/cm<sup>3</sup>. This observation supports that the equivalent polymer layer thickness increases as the solvent quality becomes poorer with temperature and more collapsed particles escape towards the silica surface.<sup>211</sup>

By contrast,  $-\Delta f_3/3$  shows a steeper increase and diverges instead of showing a plateau at 32 °C and 34 °C. This behavior points out the effect of the phase separation on the film formation kinetics.

Interestingly, the deposition of P(NIPAAm) thin film monitored at 36 °C resembles the one observed for temperatures below LCST, and the estimated equivalent layer thickness is 2.2 nm which is in between the value calculated between 24 °C and 30 °C. This similarity could be explained by the effect of the mesoglobules' formation of P(NIPAAm) in solution occurring at higher temperatures: most of the globules are aggregating instead of diffusing and adsorbing at the interface water-solid. Such behavior has already been reported for diphasic solutions composed of oppositely charged polyelectrolytes adsorbing at air-water interface.<sup>212</sup>

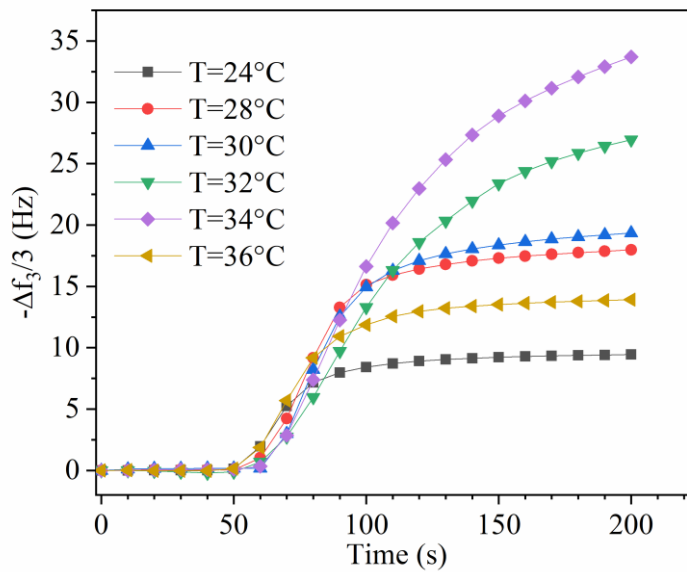


Figure 4.2 Evolution of the negative frequency shift as a function of time upon injecting P(NIPAAm) aqueous solution on SiO<sub>2</sub> surface.

To better understand the effect of constant temperature on the film formation kinetics, the negative resonance frequency shift  $-\Delta f_3/3$  was first normalized to the values at beginning and infinity of film formation using equation (4.1):

$$\varphi(t) = \frac{\frac{\Delta f_3}{3}(t) - \frac{\Delta f_3}{3}(\infty)}{\frac{\Delta f_3}{3}(0) - \frac{\Delta f_3}{3}(\infty)} \quad (4.1)$$

Where  $\varphi(t)$  is the polymeric film formation progress (the conversion of P(NIPAAm) coils into globules also known as the collapse process),  $\frac{\Delta f_3}{3}(t)$ ,  $\frac{\Delta f_3}{3}(\infty)$ ,  $\frac{\Delta f_3}{3}(0)$  are the resonance frequencies at time  $t$ , extrapolated to infinite time and at the start of the film formation, respectively.

Figure 4.3a displays this normalization as a function of temperature. We can see distinct normalized curves as the temperature increases from 24 °C to 32 °C, however we also observe an overlap of the data at 34 °C and 36 °C. Due to this overlap, we considered diluting the solution ten times to deconvolute the film formation progress.

In order to better quantify the polymeric film progress as a function of time, we define  $\tau_{\text{off}}$  (the observed time) as the time required for P(NIPAAm) coils to decrease their numbers by  $1/e$  at the silica surface. Graphically, we represent this extracted time as the intersection between the horizontal line  $1/e$  and the  $\varphi(t)$  curve.

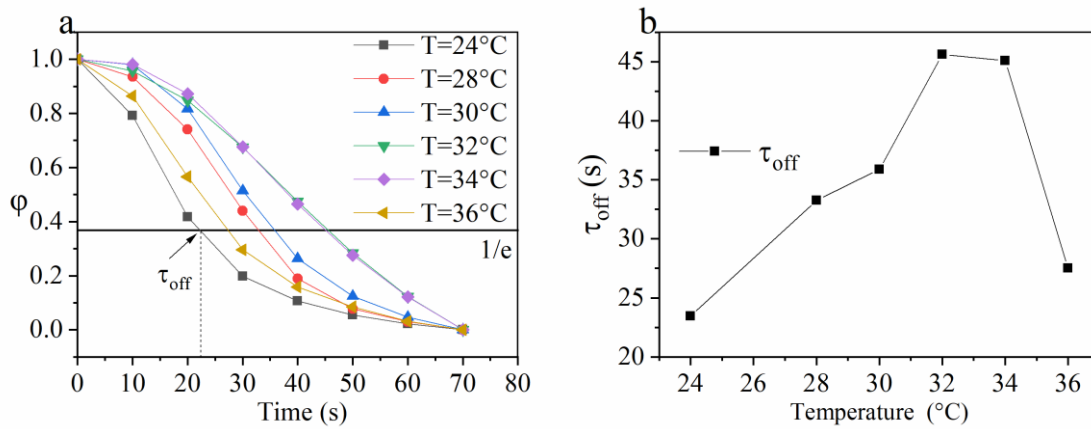


Figure 4.3 Normalization of the polymeric film formation progress  $\varphi$  as a function of time for different temperatures below and above the critical transition temperature (a). Plot of the extracted observed time as a function of time (b).

Figure 4.3b shows that the increase of temperature from 24 °C to 32 °C results in a deceleration of the conversion coil to globule as  $\tau_{\text{off}}$  increases from 22.6 s to 45.6 s. Meanwhile, we note a stepwise acceleration of this process: first between 32 °C and 34 °C and second between 34 °C and 36 °C.

In order to investigate the relaxation behavior of P(NIPAAm) formed layers, we employed the empirical *Kohlrausch-Williams-Watts* relaxation function (previously presented in chapter 1) to directly represent the polymeric film formation progress.

$$\varphi(t) = \exp \left[ -\left(\frac{t}{\tau}\right)^\beta \right] \quad (4.2)$$

where  $\tau$  presents the film formation time scale and  $\beta$  the KWW exponent having characteristic values for certain dynamic processes.

Stretched KWW fit curves with  $\beta < 1$  were once again used to describe the dynamics of systems showing subdiffusive behavior whereas compressed KWW fit curves with  $\beta > 1$  were attributed to the dynamics of “soft glassy materials”.

Fitting our experimental data into equation (4.2) using  $\tau$  such that  $\varphi(t) = e^{-1}$  revealed that better fits are obtained when  $\beta > 1$  compared to simple exponential  $\beta = 1$  and stretched fit  $\beta = 0.7$ , as shown in Figure 4.4a.

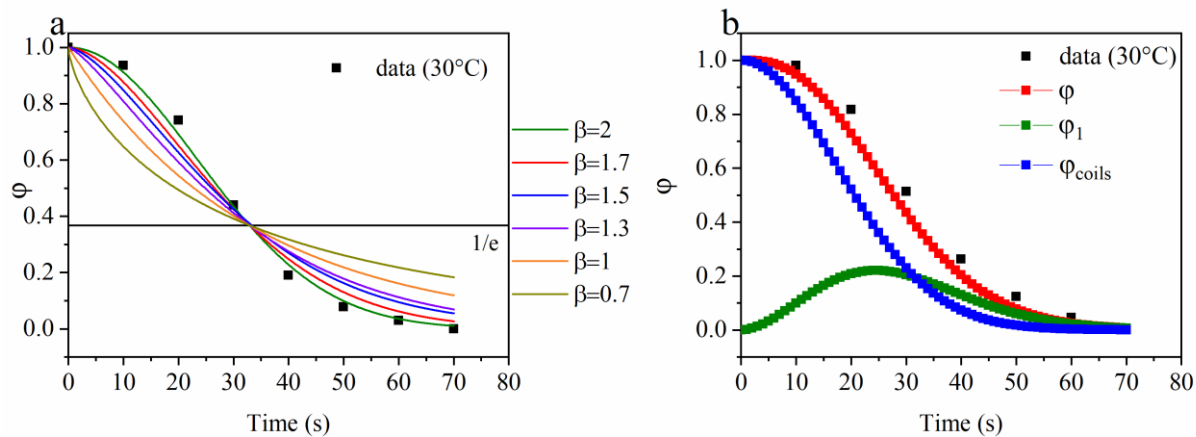


Figure 4.4 Normalized evolution of P(NIPAAm) film formation progress as a function of time at 30 °C as observed during isothermal formation of P(NIPAAm) film. Black: Normalized QCM-data, see text for details. Colored lines: KWW fit curves using different values for  $\beta$  (a). Fit of normalized data at 30°C according to two-step kinetic model. Black: Normalized data. Colored lines: fractions of polymer species during the film formation process as given by equation (4.3).

This compressed exponential function implies that the formation process of P(NIPAAM) layer(s) on silica surface relaxes faster than following a simple exponential. While one should expect slower decay as reported for glassy systems, the unusual compressed exponential behavior has been attributed recently to deformation of soft colloids at high packing density.<sup>213</sup>

Moreover, the microscopic origin of the higher  $\beta$  exponent was claimed to be due to an interplay between dynamical heterogeneities (collective motions of portions of particles) and particle deformations including deswelling,<sup>214</sup> interpenetration,<sup>215</sup> and isotropic compression.<sup>216</sup>

Interestingly,  $\beta > 1$  was also used to describe different systems being out of equilibrium by sufficiently time-resolved and ensemble-averaged methods, including X-ray photon spectroscopy,<sup>217</sup> diffusion wave spectroscopy,<sup>218</sup> static light scattering in highly packed system.<sup>90</sup>

These studies were mainly dedicated to bulk colloidal glasses. However,  $\beta > 1$  was rarely found for soft colloidal particles under confinement, which is most probably due to the lack of techniques enabling the monitoring of structural evolution of confined soft particles except with confocal microscopy.<sup>123</sup> To the best of our knowledge, this is the first study of the anomalous dynamics of colloidal particles in thin films using the quartz crystal microbalance with dissipation monitoring QCM-D.

### 4.4.3 Two-Step Model Hypothesis

To understand the experimental observation of compressed exponential kinetics, we used a two-step kinetic model developed in a previous investigation of decelerated melting<sup>219</sup> of crystalline materials where their solid-liquid transition exhibits slow kinetics and can also be fit by equation (4.2).

The application of this two-step model in the current case suggests a competition between two processes. We assume that the first process is governed by superdiffusive dynamic (non-Fickian diffusion) due to random local instabilities. For the current assumption, the KWW exponent was chosen to be  $\beta=2$ . For this value of  $\beta$ , the fit corresponds to a Gaussian function, and thus the probability density of local random instability shows a Gaussian distribution.

However, the second process is assumed to result from diffusive motions as particles displacement should increase as the square root of time (Fickian diffusion). This assumption implies that the decay function shows a simple exponential behavior (reflecting first or zero order kinetic) with a  $\beta=1$ .

The experimental data was modeled using this two-step model (see Figure 4.4b). The obtained film formation progress (fraction of polymer particles  $\varphi(t)$ ) follows the function.

$$\varphi(t) = \varphi_{\text{coils}}(t) + \varphi_1(t) = \left\{ \frac{\sqrt{\pi} \tau_1}{2 \tau_2} \exp\left(-\frac{t}{\tau_2}\right) \exp\left(\left(\frac{\tau_1}{2\tau_2}\right)^2\right) \left[ \operatorname{erf}\left(\frac{\tau_1}{2\tau_2}\right) - \operatorname{erf}\left(\frac{\tau_1}{2\tau_2} - \frac{t}{\tau_1}\right) \right] \right\} + \exp\left(-\frac{t}{\tau_2}\right) \quad (4.3)$$

Here  $\varphi_{\text{coils}}$  represents the fraction of polymer coils on the surface,  $\varphi_1$  represents the fraction of an intermediate phase before transformation into a packed film on the surface and the indices 1 and 2 refer to the step number, respectively.

Considering that the formation of the P(NIPAAm) film is the result of the deswelling and collapse of the coils, one can think that the extracted transformation times  $\tau_1$  and  $\tau_2$  are related to the diffusion time scale of the system's particles on the film's thickness, while  $\tau_{\text{off}}$  is related to the viscoelastic structural relaxation rate due to the coil-globule transformation.

To investigate the temperature induced transition on the dynamics of P(NIPAAm) film deposition on silica surface, we scaled the logarithm of the observed characteristic transformation times  $\tau_1$  and  $\tau_2$  extracted from equation (4.3) as well as  $\tau_{\text{off}}$  as a function of the inverse of temperature for two different concentrations (see Figure 4.5a).

As expected from the previously normalized data in Figure 4.3b, the film transformation at 0.04 wt% concentration shows two competing kinetic regimes depending on whether the temperature is lower or higher than 30 °C. The first kinetic regime is rather slow as the logarithm of the observed experimental time  $\tau_{\text{off}}$  increases from 24 to 30°C while the second regime is fast as  $\ln \tau_{\text{off}}$  decreases from 30 to 36°C.



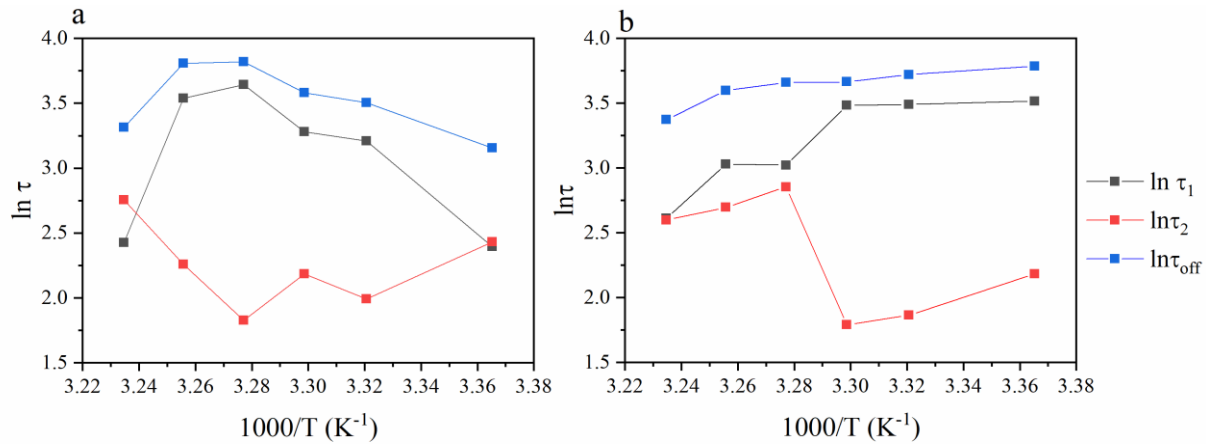


Figure 4.5 Arrhenius plot of characteristic transformation times extracted from the two-step model at 0.04 wt% P(NIPAAm) aqueous solution (a), at 0.0004 wt% P(NIPAAm) aqueous solution (b).

Below 30°C, the increase of temperature results in an increase of the logarithm of  $\tau_1$ , while  $\tau_2$  decreases in the same considered temperature range. We note a change in the slope of the extracted times and the offset time as the temperature increases between 24 °C and 28 °C, suggesting that the collapse transition is happening below the LCST and could be considered as a thermally activated process.

When the temperature is higher than 30 °C, we observe that the evolution trend of  $\tau_1$ ,  $\tau_2$  and  $\tau_{\text{off}}$  is reversed. The parallel evolution of  $\tau_{\text{off}}$  and  $\tau_1$  below and above 30°C reveals that the superdiffusion dominating the first process has a link with the viscoelastic nature of P(NIPAAm).

In addition, we notice that the sum of  $\tau_1$  and  $\tau_2$  gives almost the same value as  $\tau_{\text{off}}$ . This observation infers that during P(NIPAAm) film formation, the whole diffusion process (non Fickian and Fickian) is in the same order of system structural relaxation.

*Table 4.2 Comparison between different relaxation times extracted from the normalized and modeled data at (0.04 wt% and 0.0004 wt%)*

Concentration	0.04 wt%			0.0004 wt%		
Temperature (°C)	$\tau_1$ (s)	$\tau_2$ (s)	$\tau_{\text{off}}$ (s)	$\tau_1$ (s)	$\tau_2$ (s)	$\tau_{\text{off}}$ (s)
24	10.95	11.39	23.44	33.65	8.87	44.07
28	24.78	7.33	33.26	32.79	6.45	41.28
30	26.57	8.89	35.87	32.57	6	39.07
32	38.19	6.21	45.60	20.52	17.35	38.85
34	34.39	9.57	45.08	20.70	14.83	36.49
36	11.3	15.73	27.50	13.62	13.43	29.17

To investigate the effect of concentration on the P(NIPAAm) film formation kinetics, we studied a ten times diluted solution via QCM and presented the two-step model extracted times and the offset time in table 4.2.

For temperatures between 24 °C and 30 °C, we note that  $\tau_1$  and  $\tau_{\text{off}}$  values are lower at higher solution concentration while  $\tau_2$  values are higher.

In the temperature range 32 °C - 34 °C, we observe that  $\tau_1$  and  $\tau_{\text{off}}$  values become higher at higher concentration whereas  $\tau_2$  is lower. In this temperature range, the effect of the concentration on the viscoelastic relaxation time and the superdiffusive process is clear as  $\tau_1$  and  $\tau_{\text{off}}$  are higher for the highest tested concentration.

At 36°C, the extracted times are qualitatively similar to the ones in 24 -30 °C.

When we look at the logarithm of the extracted times as a function of the inversed temperature at ten times diluted concentration (see Figure 4.5b), we observe almost no temperature dependence in 24 °C - 30 °C of the process associated with  $\tau_1$  whereas the process associated with  $\tau_2$  shows a little temperature dependence as compared to the more concentrated solution in the same temperature range. This observation suggests that the increase of concentration slows the deswelling kinetics below LCST due to higher particle packing.

When the temperature reaches 30 °C, a clear transition from a first to a second kinetic regime takes place, both and decrease in parallel and it seems both processes dominate the activation energy in 30-36 °C temperature range.

As we mentioned earlier, the two step model was used to study the kinetics of melting of materials with large free volume such as zeolites.<sup>220</sup> The high free volume of these materials leads to the collapse of their structure at a temperature close to the glass transition of the molten liquid. In our study, the studied material is a glassy polymer and the temperature range 24-36°C.

It is widely accepted that in contrast to highly porous materials, glassy polymers such as P(NIPAAm) have less free volume below  $T_g$ . Their polymer chains are not sufficiently mobile to allow the solvent to penetrate the polymer core easily.<sup>221</sup>

This restriction of polymer chains in glassy state results in fixed holes that hinders the solvent molecules' diffusion during the swelling-deswelling process.<sup>222</sup>

Moreover, our results illustrate that the formation process of P(NIPAAm) polymer film due to deswelling phenomenon results mainly from two steps, both dependent on temperature and concentration. This two-step diffusion model is in agreement with Long and Reichman model related to diffusion of vapors in glassy polymers.<sup>223</sup>

They proposed that the swelling process happens stepwise as the concentration of vapor does not instantaneously reach its equilibrium value at the polymer surface. In the first step, the sorption shows characteristics of Fickian diffusion. The second step is slow and shows diffusion anomalies

due to the slow relaxation of polymer segments. The formation of P(NIPAAm) film in our case is due to deswelling, this is why the order of the processes is inverted.

The observed diffusion anomaly expressed in our model is also in agreement with Thomas and Windle's model.<sup>224</sup> The kinetic controlling process for transport in glassy polymer is considered to be diffusion of solvent coupled with time-dependent mechanical deformation of the polymer glass in response to the swelling stress. In our study, we show that the extracted times for diffusion process via the two-step model are in the same order of time as the observed P(NIPAAm) relaxation time provided by QCM experiment.

It is worth noting to mention that the evolution of  $\tau_{\text{off}}$  as a function of concentration below and above LCST is partially in agreement with recent results of colloidal silica-P(NIPAAm) core – shell nanogels.<sup>196</sup>

Diluted concentrations show decrease of relaxation times (fast dynamics) from 20 °C to 36 °C from but slow dynamics at high concentration. Moreover, the estimated structural relaxation at 36 °C is in the same order of magnitude for the observed transformation time of our system, although we are investigating a thin film with a non-time resolved technique.

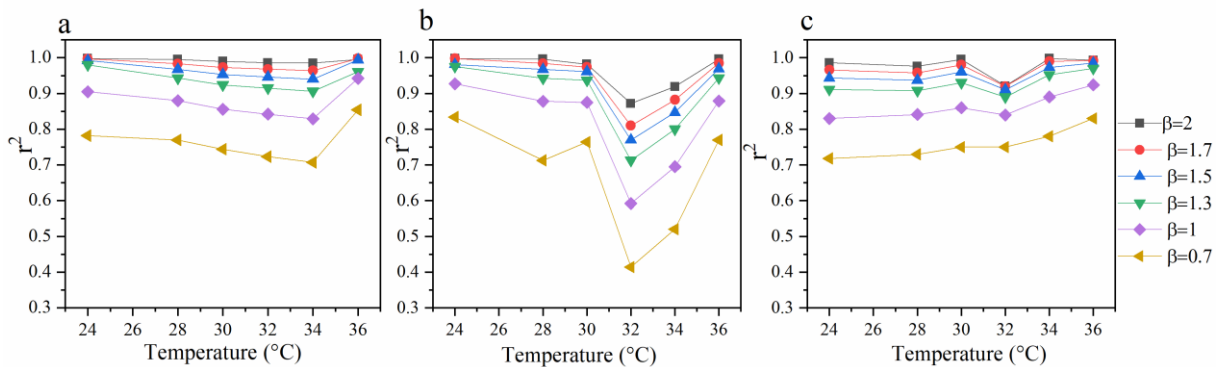


Figure 4.6 Quality fit of KWW equation applied to P(NIPAAm) film formation normalized data as a function of temperature at three different concentration: at 0.04 wt% P(NIPAAm) aqueous solution (a) at 0.009 wt% P(NIPAAm) aqueous solution (b) at 0.004 wt% P(NIPAAm) aqueous solution (c).

The difference in the evolution of  $\tau_1$  and  $\tau_2$  with concentration below and above 30 °C suggests that superdiffusion and diffusion regimes dominate the film formation depending on temperature and concentration.

In order to gain better insight about the interplay between these two mechanisms, we fitted our data according to equation (4.2) by fixing  $\tau = \tau_{\text{off}}$  and change of  $\beta$  between 0.7 and 2 for three different concentrations 0.04 (most concentrated), 0.0009 (semi diluted) and 0.0004 wt% (diluted) (see Figure 4.6).

For all concentrations and for a temperature below 30 °C, we observe that the best fit is mainly represented by compressed exponential functions with  $\beta = \{1.3; 1.5; 1.7; 2\}$  as compared to simple and stretched functions. The discrete values of  $\beta$  were chosen on the basis of different values reported in the literature for highly packed disordered systems: 1.3 for metallic glasses below  $T_g$ <sup>225</sup> and 1.5 for shrinking colloidal gels.<sup>226</sup>

For the most concentrated and semi-diluted solutions, the quality fit decreases with temperature from 24 °C to 30 °C.

However, for the most diluted solution  $\beta$  decreases in same fashion then increases suddenly between 28 °C and 30 °C.

From 30 °C to 32 °C, we observe a decrease in the fit quality for all different  $\beta$  values at all concentrations. This decrease confirms that dynamic of the film formation changes near to the LCST and could imply other mechanisms along with diffusion, including changing between repulsive and attractive forces.

At temperatures between 32 °C and 34 °C, we observe that the quality fit is stable for the more concentrated solution and an increase of the fit quality for the semi-diluted and diluted solutions.

Finally, between 34 °C and 36 °C, we observe a good quality fit for the compressed exponential with  $\beta = \{1.3; 1.5; 1.7; 2\}$ . Again, we emphasize here that the first process (superdiffusion) dominates the film formation of P(NIPAAm) on silica surface in particular at high concentration.

Although the compressed exponential with  $\beta = 1.5$  was observed for many aging colloidal systems and was explained microscopically by relaxation of internal stresses associated with deswelling,<sup>227</sup>

more theoretical work is required to determine the microscopic picture of why the best fit is observed for P(NIPAAm) chains at  $\beta = 2$ .

In conclusion, the difference in the evolution of  $\tau_1$  and  $\tau_2$  below and above 30 °C suggests that we have two different steps associated with the formation of P(NIPAAm) thin film on silica surface, the steps being a superposition of concentration and temperature driven effects.

#### **4.4.4 Variation of viscoelastic properties of P(NIPAAm) layers upon isothermal deposition**

After focusing on the kinetic dependence of P(NIPAAm) layers with temperature on the frequency shift during isothermal deposition, we would like to investigate if the stepwise character of the kinetic has a direct link with the viscoelasticity of P(NIPAAm) layers. It is widely accepted that polymer chains often relax on the time scale (the oscillation's period of QCM-D experiment) leading to dependence of the viscoelastic properties with frequency. QCM-D offers the possibility to investigate this dependence by comparing the material response to different overtones.

Figure 4.7a, Figure 4.7b and Figure 4.7c show the evolution of the negative frequency shift as a function of the overtone order at  $n = \{3,5,7\}$  corresponding to 15, 25, 35 MHz respectively, for different temperatures below LCST (24 °C), around LCST (32 °C) and above LCST (36 °C). In the two first cases (24 °C and 32 °C), we observe an overlap of  $-\Delta f_n/n$  at the three studied overtones between 0 and 70 s followed by a dispersion and consistent decrease of  $-\Delta f_n/n$  values with the overtone number between 70 and 200s.

While the  $n$ -independent values for  $-\Delta f_n/n$  reflect the rigid nature of the adsorbed film, the divergence of those values reveals its rather viscoelastic nature,<sup>124</sup> below and around LCST. Above LCST we see a continuous overlap of  $-\Delta f_n/n$  as a function of the overtones from 0s to 200 s, which again is the signature of rigid layers' formation.

Interestingly, the evolution of the isotherms follows different shapes. While we observe a Langmuir shaped curve (indicating monolayer adsorption) at 24 °C, the adsorption curve at 32°C shows similarity with BET sigmoidal isotherms (indicating multilayers adsorption). At 36 °C the isotherm of P(NIPAAm) shows a Langmuir like shape, although one expects multilayer adsorption of aggregates to happen at this temperature as previously shown in our DLS measurements.

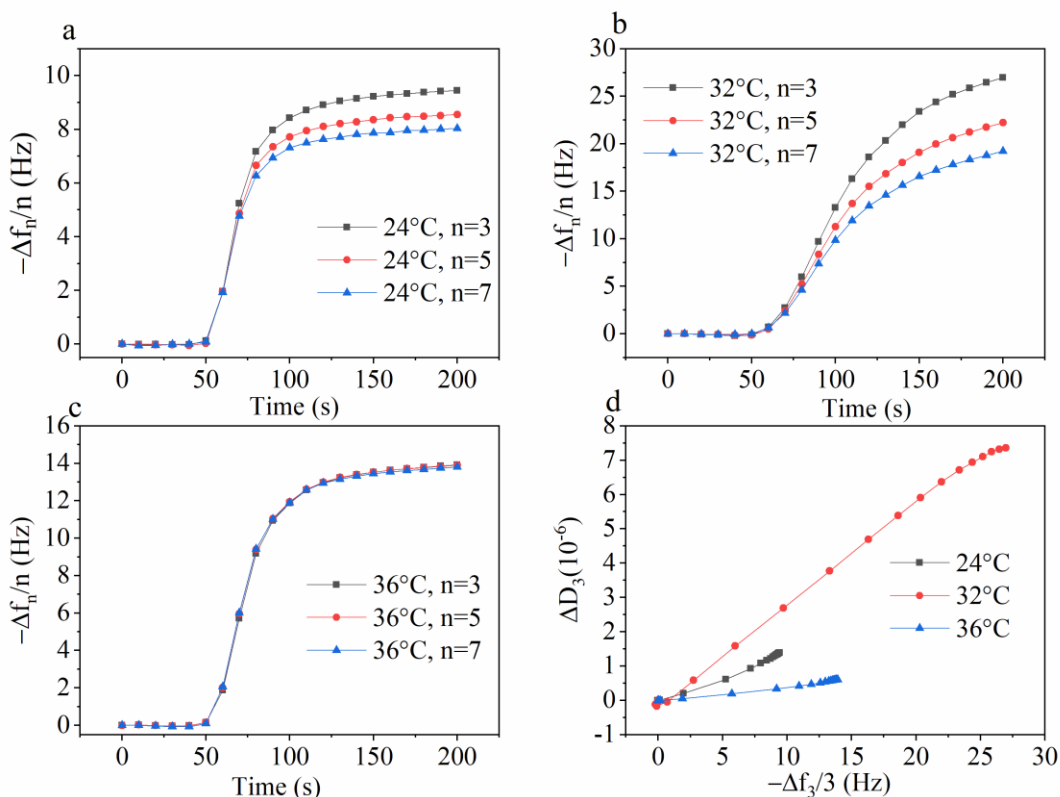


Figure 4.7 The evolution of the negative frequency shifts as a function of time upon injection 0.04wt% P(NIPAAm) aqueous solution on  $\text{SiO}_2$  surface. Data from third -, fifth- and seventh – order harmonics are included and are scaled according to equation (4.2) for direct comparison at different isothermal conditions below LCST (a), at LCST (b) and above LCST (c). Dissipation changes were plotted against the negative frequency shift for the same polymer solution below, during and above LCST (d).

Plotting dissipation  $\Delta D_3$  vs.  $-\Delta f_3/3$  (see Figure 4.7d, D-f plot) allowed us to eliminate the time as a variable and focus on the link between the surface coverage ( $-\Delta f_3/3$ ) and viscoelasticity ( $\Delta D_3$ ).<sup>164</sup>

First we note that the frequency shifts and the dissipation shifts increase in parallel, and they do so from the very beginning of the experiment for the 24 °C and 32 °C experiment, and with a little delay for the 36 °C. The linear increase indicates a layer-by-layer homogenous growth followed by a deviation from linearity which could be attributed to further rearrangement or conformational changes with higher surface coverage.<sup>180</sup>

Estimation of the slope of each D-f plot yields the highest slope  $\Delta D_3/(-\Delta f_3/3)$  at 32 °C while the lowest slope is attributed to 36 °C. In addition, the linear part corresponds to ~81.5% of the complete adsorption at 32 °C while it amounts to ~55% and ~66% at 24 °C and 36 °C, respectively.

Although our silica substrate is hydrophilic, we observe similarities of our D-f plot at different temperatures with a similar plot from isothermal deposition of P(NIPAAm) at 31 °C on hydrophobic gold<sup>164</sup> where the linear regime was reported to cover the first 70% of adsorption process.

However, the adsorption curve characteristics of cationic polyelectrolytes on gold differ slightly, the linear regime starting after 25% of the adsorption as the polyelectrolyte forms a rigid monolayer in the early stages of the adsorption, not causing any dissipation changes.<sup>228</sup>

This comparison shows that the viscoelasticity of the built up P(NIPAAm) layers as well as the surface coverage are a function of temperature in contrast to non-thermosensitive polymers. Although we observe the same growth mechanism (homogenous growth followed by densification), we expect different layer structure due to the effect of temperature on polymer conformation. Our results postulate that we have multilayers formation characterized by high viscoelasticity around the LCST (32 °C), swollen monolayer of coils below the LCST (24 °C) and rigid multilayers of globules above the LCST (36 °C).

#### **4.4.5 Non-isothermal kinetic study of glassy wet layers on P(NIPAAm) on silica surface**

In order to know more about the kinetics of formation P(NIPAAm) layers on silica surface we studied the evolution of the resonance frequency shift as a function of temperature during heating and cooling cycles as shown in Figure 4.8a where 0.05 K/min as an example of scanning rate.

Increasing values of  $-\Delta f_3/3$  indicate that the areal mass load of the QCM sensor increases. The increase of temperature from 20 °C results in a slight increase of  $-\Delta f_3/3$  which could be explained by slight adsorption of P(NIPAAm) at the silica-water interface. Once the temperature reaches 31.6 °C (corresponding to the intersection between the tangents of the curve when the signal changes its slope), we observe a sudden growth of  $-\Delta f_3/3$  which reaches a plateau at ~38 °C.



The sudden jump of  $-\Delta f_3/3$  is probably due to LCST as the water/P(NIPAAm) are expected to phase separate on silica surface leading to higher adsorption. Interestingly, this sharp LCST transition shows similarities to the one reported for P(NIPAAm-co-DEGDVE) layers deposited on nanostructured surfaces<sup>135</sup>, although the reported value of LCST is 3.1 K lower than our extracted value. The cooling of this solution shows a remarkable hysteresis and happens in two stages: one stage between 39.93 °C and 31.1 °C (corresponding to the breaking up of aggregates and hydrogen bonds),<sup>229</sup> the second stage between 31.1 °C and 20 °C (associated with the dissolution of the polymer and as a consequence desorption from the surface).

The asymmetry between the heating and cooling processes on P(NIPAAm) wet layers suggests that we may have a slow dynamic not only during heating (as corroborated by our isothermal deposition measurements) but also during cooling. In order to gain a better insight into the kinetic dependence of deposited P(NIPAAm) layers, we show in Figure 4.8b the effect of the cooling rate on the negative frequency shift between 39.93 °C and 20 °C. The increase of the cooling rate leads to the shift of the disaggregation and dissolution temperatures to lower values.

This behavior indicates that the deposited P(NIPAAm) layers behave like a supercooled liquid and may show a glass transition phenomenon upon cooling. Therefore, we normalized the data of the first cooling stage as a function of time for different cooling rates according between 39.9°C and the dissolution temperature (inflection point) according to equation (4.1). In this case  $\varphi(t)$  represents the evolution of the glassy film disaggregation,  $\frac{\Delta f_3}{3}(t)$ ,  $\frac{\Delta f_3}{3}(\infty)$ ,  $\frac{\Delta f_3}{3}(0)$  are the resonance frequencies at time  $t$ , extrapolated to infinite time corresponding to the inflection point of the cooling curve, and at the start of the glassy film disaggregation, respectively (see Figure 4.8c).

Interestingly, although we are working with a diluted P(NIPAAm) solution on a surface, we observe a clear hallmark of colloidal glass transition during cooling of P(NIPAAm) : First a fast decay attributed to  $\beta$ -relaxation, followed by an intermediate plateau then the slower  $\alpha$ -relaxation.<sup>90</sup> This observation suggests that when starting cooling, the concentration of polymer at the surface could be higher than in the bulk solution and we may have a formation of P(NIPAAm) glassy wet layers which have slow dynamics like concentrated colloidal suspension with high volume fraction.

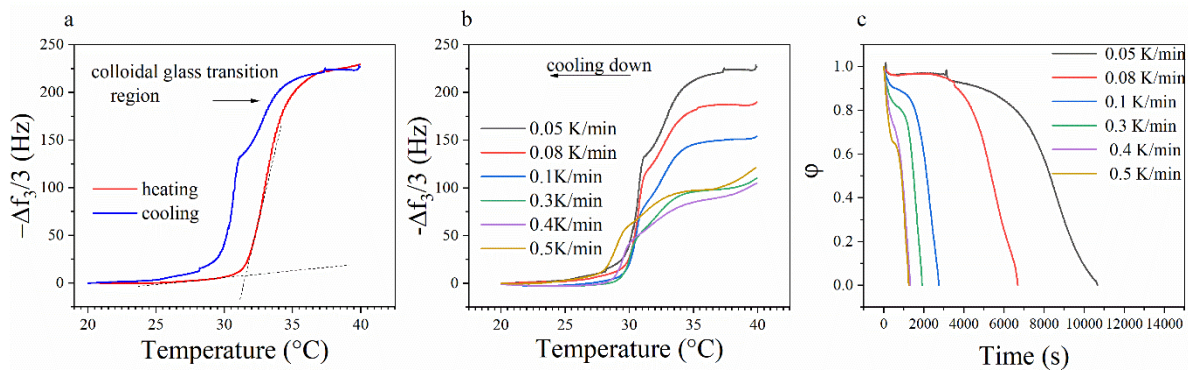


Figure 4.8 Non-isothermal scan of P(NIPAAm) flowing solution of 0.04wt% on silica surface at 0.05K/min heating and 0.05K/mn cooling (a). negative frequency shifts as a function of temperature as different cooling rates as indicated (b), normalization upon cooling the solution between 39.9°C and the dissolution temperature (inflection point) at different scanning rates. The investigated solution is 0.04 wt% P(NIPAAm) in water (c).

We have shown that non-isothermal treatment of P(NIPAAm) solution leads to the formation of glassy structures on silica surface due to coil collapse and water release. The glassy structure thus formed is also kinetically dependent.

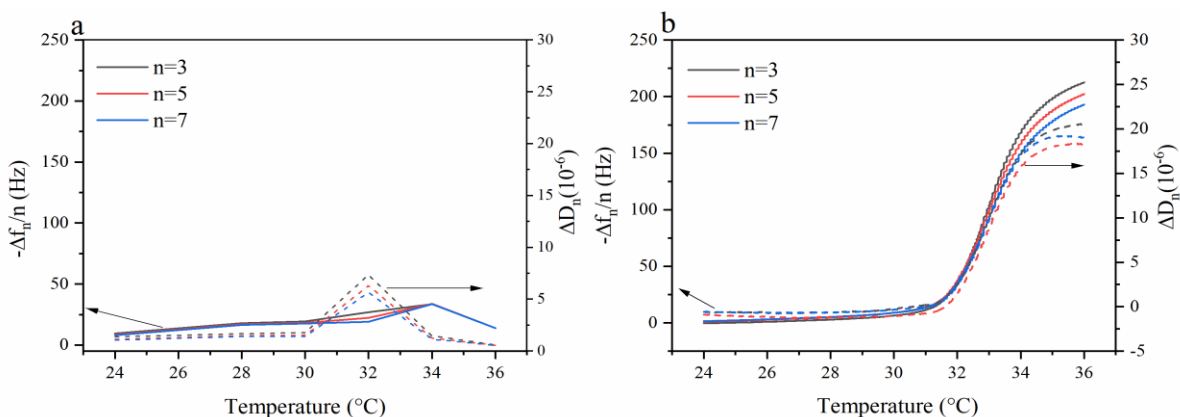
Moreover, we have elucidated in the previous sections that the isothermal deposition of P(NIPAAm) layers may involve formation of glass-like structures during the deswelling.

Figure 4.9a and Figure 4.9b show a comparison between a constructed non-isothermal scan from the resonance frequency and dissipation shifts at different overtones retrieved from the isothermal study (at 0K/min) and non-isothermal at 0.05 K/min heating rate of the same P(NIPAAm) solution 0.04 wt%.

We observe first through  $-\Delta f_n/n$  that the overall deposited mass of P(NIPAAm) is higher at 0.05K/min in the represented temperature range 24-36°C. However, we see that for both isothermal and non-isothermal graphs, the dissipation peaks happen around the LCST (at ~32°C and ~33.2°C). This jump is reminiscent of the increase of surface shear elasticity and viscosity already

reported for P(NIPAAm) photocrosslinked on gold surface<sup>230</sup> or adsorbed at the air-water interface<sup>231</sup> underlying a transition from a Newtonian liquidlike state to an elastic state.

However, a comparison between the data of the two figures between 34 and 36°C, reveals that while  $-\Delta f_n/n$  and  $\Delta D_n$  decrease in isothermal condition conjointly with an overlap of the overtones (rigidification/stiffening), the non-isothermal treatment leads to an increase of  $-\Delta f_n/n$  and spreading of the overtones (softening). This observation supports the idea that denser P(NIPAAm) layers could be produced isothermally as compared to the non-isothermal scan.



*Figure 4.9 Construction of a non-isothermal heating scan at an imaginary heating rate 0 K/min. The data points of the resonance frequency and dissipation shifts were retrieved at 200s from P(NIPAAm) isotherms at the previously studied temperatures and overtone (a), Non-isothermal scan of P(NIPAAm) flowing solution of 0.04wt% on silica surface at heating rate 0.05 K/mn (b). In this figure the resonance frequency and dissipation shifts at different overtones are represented.*

## 4.5 Conclusion

In this contribution we explored the formation of wet poly(N-isopropylacrylamide) layers on silica surface using the Quartz Crystal Microbalance with dissipation monitoring technique (QCM-D). Employing a simple two-step kinetic model revealed that the formation of polymer layers is governed by a two-stage model where the first stage is superdiffusive (slow process) while the second stage is diffusive (fast process).

The two-step model showed us that the formed film relaxes at the same time as the QCM experiment and the observed relaxation time is in the same order of magnitude of the extracted times from the employed model showing diffusion anomaly.

Thinking from a glass perspective, we supposed that this diffusion anomaly originates from the formation of a glassy-like structure of the film due to the collapse of the polymer. This glassy structure prevents a normal diffusion of polymer particles or water molecules as it is characterized by structural changes and maybe abnormal higher concentration gradient on the thickness.

Furthermore, it has slow relaxation times and shows dramatic increase of frequency and dissipation shifts, reminiscent of rheological changes of polymers during the glass transition.

Finally, we show that the glass-like behaviour of P(NIPAAm) layers can be studied by changing the heating rates and cooling rates upon non-isothermal scans. In addition, the normalization of our data in the cooling process showed that the formed layers undergo a colloidal glass transition similar to the one detected by ensemble averaged methods when investigating overpacked thermosensitive colloids.

Our findings should be of a great interest in the field of soft glassy thin films.

## Conclusion of the manuscript

In conclusion, this work investigated the isothermal deposition kinetics, structural complexity and mechanical properties of glass-forming soft layers using a high-frequency surface spectroscopy technique: a quartz crystal microbalance with dissipation monitoring (QCM-D).

The first motivation of this thesis was to simulate the glass transition under near ambient-temperature conditions (15-60°C). To carry out this simulation, thin films of stimuli-responsive polymers dissolved in aqueous solution were physically applied on a silica-coated substrate.

The materials studied in this manuscript are the dual light- and temperature-responsive poly (triethylene glycol acrylate-co-spiropyran acrylate) P(TEGA-co-SPA) and the temperature-responsive poly(N-isopropylacrylamide) P(NIPAAm). The choice of these two polymeric materials is based on several criteria.

- First, they offer the possibility of forming glasses when they undergo phase separation in solution. This property opens the way to obtaining novel glasses at low temperatures, compared to conventional silicate glasses often produced at high temperatures ( $T > 1000^\circ\text{C}$ ).
- Second, applying different stimuli to these confined materials enables the control of the particle size and the interactions between the particles and the solvent. Consequently, stimuli through heat or illumination can be used to manipulate the film formation kinetics and the conformational state of the film.
- Third, polymer particles are characterized by their deformability through shrinking, interpenetration and compression, in contrast to hard inorganic glass particles. These features allow us to simulate the formation of glasses with high particle-packing density. Our aim is to correlate this high particle-packing density to strong mechanical properties.

After introducing structure-property relationships of materials at interfaces (chapter 1) and fundamentals of shear elastic waves analysis (chapter 2), we dedicated chapter 3 and chapter 4 to elucidating the results of our study.

In chapter 3, we investigated the effect of temperature and light on the conformational changes of a Poly (triethylene glycol acrylate-co-spiropyran acrylate) (P(TEGA-co-SPA)) copolymer containing 12%–14% of Spiropyran in dilute aqueous solution by Dynamic Light Scattering (DLS)

and at the silica–water interface by Quartz Crystal Microbalance with Dissipation Monitoring (QCM-D). We showed that the hydrodynamic radius  $r_h$  of the studied copolymer solution increased suddenly at  $\sim 66^\circ\text{C}$  (339.15 K). This sudden increase of  $r_h$  characterizes the lower critical solubility temperature (LCST) of thermosensitive polymers. Here, the observed transition temperature occurred  $\sim 23$  K above the reported cloud point for the same copolymer composition diluted in pH 8 TRIS buffer and irradiated with 540 nm green light, as detected by UV/VIS spectroscopy. This temperature shift was discussed in the context of changed electrostatic interactions due to salts contained in the buffer.

Furthermore, we investigated the effect of UV-light on the hydration state of the isothermally deposited P (TEGA-co-SPA) layers below and above the LCST, by monitoring shifts in resonance frequency and in acoustic dissipation as a function of temperature and illumination conditions.

Below the lower critical temperature, the layer of P(TEGA-co-SPA) swells under UV-light due to the photoisomerization of the hydrophobic Spiropyran into the more hydrophilic Merocyanine. This photo-induced hydration is favoured when the thermoresponsive part of the copolymer P(TEGA) is sufficiently hydrophilic and results in the extension of the adsorbed copolymer coils towards the solution.

Above the LCST, we see a competition between PTEGA globule adsorption on the sensor surface and photoconversion of Spiropyran to Merocyanine, facilitating desorption. When the UV-light is switched on, the growth of the copolymer film is decelerated, and while the conformational changes of the copolymer can still proceed within the film, these would be significantly slower in their response rate due to reduced film mobility when compared to the polymer in solution.

Moreover, we show through non-isothermal scans that the coil-to-globule transition of the adsorbed copolymer being exposed to visible or UV light shifts to a lower LCST compared to the bulk solution: the transition temperature determined acoustically on the surface is 4 to 8 K lower than the cloud point temperature reported by UV/VIS spectroscopy in aqueous solution. We attribute this difference to the formation of non-equilibrium adsorbed multilayers on the silica surface.

Last but not least, we demonstrated that the built-up wetting layers display a variation of their viscoelastic properties with temperature and illumination conditions, which affects their densification. Under visible light, a dense film is formed once the surface is saturated. Under UV-

light, we expect a film with lower density as the adsorbates have less time to rearrange themselves due to the deceleration of adsorption and polarity change.

In chapter 4, we investigated the formation of soft poly(N-isopropylacrylamide) P(NIPAAm) layers on silica surface using the Quartz Crystal Microbalance with dissipation monitoring technique (QCM-D).

As a preliminary study, we have characterized this thermosensitive material in powder using X-Ray diffraction (XRD) and Differential Scanning Calorimetry (DSC) and in dilute aqueous solution using Dynamic Light Scattering (DLS).

We showed that in powdered form, this material is amorphous and has a glass transition temperature of  $\sim 137.6^{\circ}\text{C}$  (410.75 K). We also observed that the  $r_h$  of P(NIPAAm) in solution increases from 3 to 268 nm at  $T \sim 32.4^{\circ}\text{C}$ . We attributed this temperature to the LCST of our studied material in solution. The DLS measurement provided us with a direct information about the size of polymer aggregates (mesoglobules) as well as its dependence on concentration and heating rate.

Furthermore, we studied the isothermal deposition kinetics of P(NIPAAm) layers on silica-coated resonators in the temperature range of  $24\text{-}36^{\circ}\text{C}$ .

By applying a two-step kinetic model (used previously to characterize the amorphization of zeolitic crystalline materials), we found that the formation of thermoresponsive layers occurs in two stages: A superdiffusive (slow process) first stage fitting a compressed exponential function and a diffusive (fast process) second stage fitting a simple exponential function. We attributed the compressed exponential behavior to the deformation of polymer particles at high particle packing density during the deswelling (shrinkage) process.

This two-step model showed us that the formed film relaxes on the time scale (the oscillation period) of the QCM-experiment, the observed relaxation time has the same order of magnitude as the extracted characteristic times of the two processes. Furthermore, these extracted times showed anomalous dependence on temperature and concentration below and above the lower critical solution temperature (LCST), inferring a possible glasslike feature of the collapsed polymer globules.

Then, we investigated the variation of viscoelasticity of the isothermally-deposited layers below and above the LCST by monitoring the frequency dependence of elastic parameters (such as shear modulus) expressed in terms of the resonance frequency and dissipation shifts.

Our results postulated the formation of multilayers characterized by high viscoelasticity around the LCST (32 °C), a swollen monolayer of coils below the LCST (24 °C) and rigid multilayers of globules above the LCST (36 °C). Here we emphasize that the layers of highest density are formed above the LCST similarly to what we observed for P(TEGA-co-SPA) under visible light illumination.

At the end, we showed through non-isothermal scans that the formation of P(NIPAAm) layers is dependent on the heating and cooling rates. In addition, the normalization of our data in the cooling process showed that the formed layers undergo a colloidal glass transition. Lastly, we noticed an analogy between the dramatic increase of resonance frequency and dissipation shifts around LCST monitored with QCM-D and the elastic property changes of polymers during glass transition using lower frequency rheological methods (e.g, Dynamic Mechanical Analysis).

The present study extends the state of the art in two main disciplines.

The first discipline is fundamental research in glass sciences. We experimentally investigated the kinetic and dynamic aspects of the glass transition of soft glass forming materials under confinement. Our work therefore constitutes another attempt to test the validity of glass transition theories. Despite the usefulness of the shear elastic waves analysis in our study, dynamic heterogeneities of confined glasses have not been investigated here. A combination of QCM-D with Raman spectroscopy or Confocal Scanning Microscopy could be useful experimental approaches to extend our findings in this direction.

The second discipline is the research of multistimuli-responsive polymers, where our findings would be of great interest for applications that need a remote-controlled switching, especially in microfluidic chips and biomedical applications.



## Zusammenfassung der Arbeit

In dieser Arbeit wurden die isotherme Abscheidungskinetik, die strukturelle Komplexität und die mechanischen Eigenschaften Glas-bildender Polymerschichten mit Hilfe einer Hochfrequenz-Oberflächenspektroskopiemethode untersucht: einer Schwingquarz-Mikrowaage mit Dissipationssaufzeichnung (QCM-D).

Die erste Motivation dieser Arbeit war es, den Glasübergang unter Bedingungen nahe der Raumtemperatur (15-60°C) zu simulieren. Dazu wurden dünne Filme von Stimulus-responsiven Polymeren in wässriger Lösung auf ein mit Siliziumdioxid beschichtetes Substrat aufgebracht.

Bei den untersuchten Materialien handelte es sich um ein licht- und temperaturempfindliches Poly(triethylenglycolacrylat-co-spiropyranacrylat) P(TEGA-co-SPA) und ein temperaturempfindliches Poly(N-isopropylacrylamid) P(NIPAAm). Die Wahl dieser beiden Polymere beruht auf mehreren Kriterien:

- Erstens ermöglichen diese die Bildung von Gläsern, wenn sie in der Lösung eine Phasentrennung vollziehen. Diese Eigenschaft gewährt Zugang zu neuartigen Gläsern bei niedrigen Temperaturen, insbesondere im Vergleich zu herkömmlichen Silikat-basierten Glassystemen, die häufig bei hohen Temperaturen ( $T > 1000^\circ\text{C}$ ) hergestellt werden.
- Zweitens ermöglicht die gezielte Nutzung verschiedener Stimuli auf diese Materialien die Einflussnahme auf die Größe der Partikel und deren Wechselwirkungen mit dem Lösungsmittel. Folglich können Stimuli in Form von Wärmezufuhr oder Beleuchtung die Kinetik der Filmbildung und den Konformationszustand des Films beeinflussen.
- Drittens zeichnen sich Polymerpartikel im Gegensatz zu harten anorganischen Glaspartikeln durch ihre Verformbarkeit durch Schrumpfung, Interpenetration und Kompression aus. Diese Eigenschaften ermöglichen es, die Bildung von Gläsern mit hoher Teilchenpackungsdichte zu simulieren. Unser Ziel ist es, diese hohe Teilchenpackungsdichte mit starken mechanischen Eigenschaften zu korrelieren.

Nach einer Einführung in die Struktur-Eigenschafts-Beziehungen von Materialien an Grenzflächen (Kapitel 1) und in die Grundlagen der Analyse scher-elastischer Wellen (Kapitel 2) widmen wir uns in Kapitel 3 und 4 der Erläuterung der Ergebnisse unserer Studie.

In Kapitel 3 beschreiben wir die Auswirkungen von Temperatur und Licht auf die Konformationsänderungen eines Poly(triethylenglykolacrylat-co-spiropyranacrylat) (P(TEGA-co-SPA)) -Copolymers mit 12%-14% Spiropyran in verdünnter wässriger Lösung mittels dynamischer Lichtstreuung (DLS) und an der Siliziumdioxid-Wasser-Grenzfläche mittels QCM-D (Schwingquarzmikrowaage mit Dissipationsaufzeichnung). Wir zeigen, dass der hydrodynamische Radius  $r_h$  der untersuchten Copolymerlösung bei  $\sim 66^\circ\text{C}$  (339,15 K) plötzlich ansteigt. Dieser plötzliche Anstieg von  $r_h$  charakterisiert die untere kritische Lösungstemperatur (engl. lower critical solubility temperature - LCST) thermosensitiver Polymere. In unseren Studien lag die beobachtete Übergangstemperatur  $\sim 23$  K über dem in der Literatur berichteten Trübungspunkt für dieselbe Copolymerzusammensetzung, welche in TRIS-Puffer bei pH 8 verdünnt und mit grünem Licht von 540 nm bestrahlt wurde. Diese Temperaturverschiebung wurde im Hinblick auf veränderte elektrostatische Wechselwirkungen aufgrund der im Puffer enthaltenen Salze diskutiert.

Darüber hinaus untersuchten wir die Wirkung von UV-Licht auf den Hydratationszustand der isotherm abgeschiedenen P (TEGA-co-SPA)-Schichten unterhalb und oberhalb der LCST, indem wir Verschiebungen der Resonanzfrequenz und der akustischen Dissipation als Funktion der Temperatur und der Beleuchtungsbedingungen beobachteten.

Unterhalb der unteren kritischen Temperatur kommt es unter UV-Bestrahlung zum Aufquellen der P(TEGA-co-SPA) -Schicht aufgrund der Photoisomerisierung des hydrophoben Spiropyrans in das hydrophilere Merocyanin. Diese photo-induzierte Hydratation wird begünstigt, wenn der thermoresponsive Teil des Copolymers P(TEGA) ausreichend hydrophil ist, und führt zu einer Ausdehnung der adsorbierten Copolymerketten in Richtung der Lösung.

Oberhalb der LCST konkurriert die Adsorption der PTEGA-Kügelchen an der Sensoroberfläche mit der erleichterten Desorption aufgrund der photo-induzierten Konversion von Spiropyran zu Merocyanin. Unter UV-Bestrahlung verlangsamt sich daher das Wachstum des Copolymerfilms. Während die Konformationsänderungen des Copolymers innerhalb des Films weiterhin stattfinden können, würden diese aufgrund der reduzierten Filmmobilität im Vergleich zum Polymer in Lösung deutlich langsamer ablaufen.

Darüber hinaus zeigen wir durch nicht-isotherme Scans, dass sich der Übergang des adsorbierten Copolymers vom Knäuel zur Kugel unter Bestrahlung mit UV oder sichtbarem Licht zu einer niedrigeren LCST im Vergleich zur Lösung verschiebt: Die akustisch an der Oberfläche bestimmte Übergangstemperatur ist 4 bis 8 K niedriger als der durch UV/VIS-Spektroskopie in wässriger Lösung gemessene Trübungspunkt. Wir führen diesen Unterschied auf die Bildung von nicht im Gleichgewicht befindlichen adsorbierten Mehrfachschichten auf der Silica-Oberfläche zurück.

Nicht zuletzt haben wir gezeigt, dass die aufgebauten Benetzungsschichten eine Variation ihrer viskoelastischen Eigenschaften in Abhängigkeit der Temperatur und der Beleuchtungsbedingungen aufweisen, was sich auf ihre Verdichtung auswirkt. Unter sichtbarem Licht bildet sich ein dichter Film, sobald die Oberfläche gesättigt ist. Unter UV-Licht erwarten wir einen Film mit geringerer Dichte, da die Adsorbate aufgrund der Verlangsamung der Adsorption und des Polaritätswechsels weniger Zeit haben, sich neu anzuordnen.

In Kapitel 4 untersuchten wir die Bildung weicher Poly(N-Isopropylacrylamid) P(NIPAAm)-Schichten auf der Oberfläche von Siliziumdioxid mit Hilfe der Schwingquarzmikrowaage mit Dissipationsüberwachung (QCM-D).

In einer Vorstudie haben wir dieses wärmeempfindliche Material in Pulverform mittels Röntgenbeugung (XRD) und Dynamischer Differenzkalorimetrie (DSC) und in verdünnter wässriger Lösung mittels Dynamischer Lichtstreuung (DLS) charakterisiert.

Wir konnten zeigen, dass dieses Polymer in pulverisierter Form amorph ist und eine Glasübergangstemperatur von  $\sim 137,6^{\circ}\text{C}$  ( $410,75\text{ K}$ ) aufweist. Wir beobachteten auch, dass der  $r_h$  von P(NIPAAm) in Lösung von 3 auf 268 nm bei  $T \sim 32,4^{\circ}\text{C}$  ansteigt. Wir führten dies auf die LCST unseres untersuchten Materials in Lösung zurück. Die DLS-Messung lieferte direkte Informationen über die Größe der Polymeraggregate (Mesoglobuli) sowie über die Abhängigkeit von der Konzentration und der Heizrate.

Außerdem untersuchten wir die isotherme Abscheidungskinetik von P(NIPAAm)-Schichten auf Siliziumdioxid-beschichteten Resonatoren im Temperaturbereich von  $24\text{-}36^{\circ}\text{C}$ .

Durch Anwendung eines zweistufigen Kinetik-Modells (das zuvor zur Charakterisierung des Kollapses (Amorphisierung) von Zeolithen – kristalliner Gerüststruktur-Materialien – verwendet

wurde) fanden wir heraus, dass die Bildung thermoresponsiver Schichten in zwei Phasen erfolgt: Ein superdiffusiver, langsamer Prozess in der ersten Stufe, die einer komprimierten Exponentialfunktion entspricht, und ein diffusiver, schneller Prozess in der zweiten Stufe, die einer einfachen Exponentialfunktion entspricht. Wir führten das komprimierte exponentielle Verhalten auf die Verformung der Polymerpartikel bei hoher Partikelpackungsdichte während des Entquellungsvorgangs (Schrumpfung) zurück.

Dieses zweistufige Modell zeigte uns, dass der gebildete Film innerhalb der Messzeitskalen (also der Schwingungsperiode) des QCM-Experiments relaxiert; die beobachtete Relaxationszeit liegt in der gleichen Größenordnung wie die extrahierten Zeiten der beiden Prozesse. Darüber hinaus zeigen diese extrahierten Zeiten eine anomale Abhängigkeit von Temperatur und Konzentration unterhalb und oberhalb der unteren kritischen Lösungstemperatur (LCST), was auf eine mögliche glasartige Eigenschaft der kollabierten Polymerkügelchen schließen lässt.

Anschließend untersuchten wir die Variation der Viskoelastizität der isotherm abgeschiedenen Schichten unterhalb und oberhalb der LCST, indem wir die Frequenzabhängigkeit der elastischen Parameter (z. B. Schermodul), in Form der Resonanzfrequenz und Dissipationsverschiebungen, beobachteten.

Unsere Ergebnisse lassen auf die Bildung von Mehrfachsichten schließen, die sich durch eine hohe Viskoelastizität im Bereich der LCST (32 °C), eine gequollene Monoschicht aus Polymer-Knäueln unterhalb der LCST (24 °C) und starre Multischichten aus Kügelchen oberhalb der LCST (36 °C) auszeichnen. Hier betonen wir, dass sich die Schichten mit der höchsten Dichte oberhalb der LCST bilden, ähnlich wie wir es bei P(TEGA-co-SPA) unter Beleuchtung mit sichtbarem Licht beobachtet haben.

Am Ende zeigen wir durch nicht-isotherme Scans, dass die Bildung von P(NIPAAm)-Schichten von den Heiz- und Kühlraten abhängig ist. Darüber hinaus zeigt die Normalisierung unserer Daten im Abkühlprozess, dass die gebildeten Schichten einen kolloidalen Glasübergang durchlaufen. Schließlich stellen wir Ähnlichkeiten zwischen dem mit QCM-D beobachteten dramatischen Anstieg der Resonanzfrequenz und den Dissipationsverschiebungen in der Nähe der LCST und den Änderungen der elastischen Eigenschaften von Polymeren während des Glasübergangs fest, die

mit rheologischen Methoden bei niedrigeren Frequenzen (z. B. Dynamisch-Mechanischer Analyse) ermittelt wurden.

Die vorliegende Studie erweitert den Stand der Technik in zwei Hauptdisziplinen.

Die erste Disziplin ist die Grundlagenforschung in den Glaswissenschaften. Wir haben experimentell die kinetischen und dynamischen Aspekte des Glasübergangs von weichen, glasbildenden Materialien unter räumlicher Beschränkung untersucht. Unsere Arbeit stellt somit einen weiteren Versuch dar, die Gültigkeit der Theorien zum Glasübergang zu prüfen. Trotz der Nützlichkeit der Analyse scherelastischen Wellen in unserer Studie, wurden dynamische Heterogenitäten von räumlich beschränkten Gläsern hier nicht untersucht. Eine Kombination von QCM-D mit Raman-Spektroskopie oder konfokaler Mikroskopie könnte ein experimenteller Ansatz sein, um unsere Erkenntnisse in diese Richtung zu erweitern.

Die zweite Disziplin ist die Erforschung auf Mehrfachstimuli ansprechende Polymere. Unsere Ergebnisse wären von großem Interesse für Anwendungen, die ein ferngesteuertes Schalten benötigen, insbesondere in mikrofluidischen Chips und biomedizinischen Anwendungen.

## Bibliography

- (1) Gilbert, R. G.; Hess, M.; Jenkins, A. D.; Jones, R. G.; Kratochvíl, P.; Stepto, R. F. T. Dispersity in Polymer Science (IUPAC Recommendations 2009). *Pure Appl. Chem.* **2009**, *81* (2), 351–353.
- (2) Hadjichristidis, N.; Pitsikalis, M.; Pispas, S.; Iatrou, H. Polymers with Complex Architecture by Living Anionic Polymerization. *Chemical Reviews.* 2001, pp 3747–3792.
- (3) Kamigaito, M.; Sawamoto, M. Synergistic Advances in Living Cationic and Radical Polymerizations. *Macromolecules.* 2020, pp 6749–6753.
- (4) Chiefari, J.; Chong, Y. K.; Ercole, F.; Krstina, J.; Jeffery, J.; Le, T. P. T.; Mayadunne, R. T. A.; Meijs, G. F.; Moad, C. L.; Moad, G.; Rizzardo, E.; Thang, S. H. Living Free-Radical Polymerization by Reversible Addition - Fragmentation Chain Transfer: The RAFT Process. *Macromolecules* **1998**, *31* (16), 5559–5562.
- (5) Hawker, C. J.; Bosman, A. W.; Harth, E. New Polymer Synthesis by Nitroxide Mediated Living Radical Polymerizations. **2001**.
- (6) Flory, P. J. Thermodynamics of High Polymer Solutions. *J. Chem. Phys.* **1942**, *10* (1), 51–61.
- (7) Huggins, M. L. THERMODYNAMIC PROPERTIES OF SOLUTIONS OF LONG-CHAIN COMPOUNDS. *Ann. N. Y. Acad. Sci.* **1942**, *43* (1), 1–32.
- (8) Arnauts, J.; Berghmans, H.; Koningsveld, R. Structure Formation in Solutions of Atactic Polystyrene in Trans-decalin. *Die Makromol. Chemie* **1993**, *194* (1), 77–85.
- (9) Fox, T. G.; Flory, P. J. Second-Order Transition Temperatures and Related Properties of Polystyrene. I. Influence of Molecular Weight. *J. Appl. Phys.* **2004**, *21* (6), 581.
- (10) Swislow, G.; Sun, S. T.; Nishio, I.; Tanaka, T. Coil-Globule Phase Transition in a Single Polystyrene Chain in Cyclohexane. *Phys. Rev. Lett.* **1980**, *44* (12), 796–798.
- (11) Pfohl, O.; Hino, T.; Prausnitz, J. M. Solubilities of Styrene-Based Polymers and Copolymers in Common Solvents. *Polymer (Guildf).* **1995**, *36* (10), 2065–2073.
- (12) Karimi, M.; Sahandi Zangabad, P.; Ghasemi, A.; Amiri, M.; Bahrami, M.; Malekzad, H.; Ghahramanzadeh Asl, H.; Mahdieh, Z.; Bozorgomid, M.; Ghasemi, A.; Rahmani Taji Boyuk, M. R.; Hamblin, M. R. Temperature-

Responsive Smart Nanocarriers for Delivery of Therapeutic Agents: Applications and Recent Advances. *ACS Appl. Mater. Interfaces* **2016**, *8* (33), 21107–21133.

- (13) Choi, A.; Seo, K. D.; Yoon, H.; Han, S. J.; Kim, D. S. Bulk Poly(N-Isopropylacrylamide) (PNIPAAm) Thermoresponsive Cell Culture Platform: Toward a New Horizon in Cell Sheet Engineering. *Biomater. Sci.* **2019**, *7* (6), 2277–2287.
- (14) Chen, J. P.; Huffman, A. S. Polymer-Protein Conjugates. II. Affinity Precipitation Separation of Human Immunoglobulin by a Poly(N-Isopropylacrylamide)-Protein A Conjugate. *Biomaterials* **1990**, *11* (9), 631–634.
- (15) Zhang, Q.; Weber, C.; Schubert, U. S.; Hoogenboom, R. Thermoresponsive Polymers with Lower Critical Solution Temperature: From Fundamental Aspects and Measuring Techniques to Recommended Turbidimetry Conditions. *Mater. Horizons* **2017**, *4* (2), 109–116.
- (16) Halperin, A.; Kröger, M.; Winnik, F. M. Poly(N-Isopropylacrylamide) Phase Diagrams: Fifty Years of Research. *Angew. Chemie Int. Ed.* **2015**, *54* (51), 15342–15367.
- (17) Van Durme, K.; Van Assche, G.; Van Mele, B. Kinetics of Demixing and Remixing in Poly(N-Isopropylacrylamide)/Water Studied by Modulated Temperature DSC. *Macromolecules* **2004**, *37* (25), 9596–9605.
- (18) Meeussen, F.; Nies, E.; Berghmans, H.; Verbrugghe, S.; Goethals, E.; Du Prez, F. Phase Behaviour of Poly(N-Vinyl Caprolactam) in Water. *Polymer (Guildf)*. **2000**, *41* (24), 8597–8602.
- (19) Hoogenboom, R.; Schlaad, H. Thermoresponsive Poly(2-Oxazoline)s, Polypeptoids, and Polypeptides. *Polym. Chem* **2017**, *8*, 24.
- (20) Kubota, K.; Hamano, K.; Kuwahara, N.; Fujishige, S.; Ando, I. Characterization of Poly(N-Isopropylmethacrylamide) in Water. *Polym. J.* **1990**, *22* (12), 1051–1057.
- (21) Bae, Y. H.; Okano, T.; Kim, S. W. Temperature Dependence of Swelling of Crosslinked Poly(N,N'-alkyl Substituted Acrylamides) in Water. *J. Polym. Sci. Part B Polym. Phys.* **1990**, *28* (6), 923–936.
- (22) Skrabania, K.; Kristen, J.; Laschewsky, A.; Akdemir, Ö.; Hoth, A.; Lutz, J. F. Design, Synthesis, and Aqueous Aggregation Behavior of Nonionic Single and Multiple Thermoresponsive Polymers. *Langmuir* **2007**, *23* (1), 84–93.
- (23) Wang, X. S.; Lascelles, S. F.; Jackson, R. A.; Armes, S. P. Facile Synthesis of Well-Defined Water-Soluble Polymers via Atom Transfer Radical

- Polymerization in Aqueous Media at Ambient Temperature. *Chem. Commun.* **1999**, No. 18, 1817–1818.
- (24) Heskins, M.; Guillet, J. E. Solution Properties of Poly(N-Isopropylacrylamide). *J. Macromol. Sci. Part A - Chem.* **1968**, *2* (8), 1441–1455.
- (25) De Las Heras Alarcón, C.; Pennadam, S.; Alexander, C. Stimuli Responsive Polymers for Biomedical Applications. *Chem. Soc. Rev.* **2005**, *34* (3), 276–285.
- (26) Costa, M. C. M.; Silva, S. M. C.; Antunes, F. E. Adjusting the Low Critical Solution Temperature of Poly(N-Isopropyl Acrylamide) Solutions by Salts, Ionic Surfactants and Solvents: A Rheological Study. *J. Mol. Liq.* **2015**, *210*, 113–118.
- (27) Yamauchi, H.; Maeda, Y. LCST and UCST Behavior of Poly(N-Isopropylacrylamide) in DMSO/Water Mixed Solvents Studied by IR and Micro-Raman Spectroscopy. **2007**.
- (28) Mukherji, D.; Wagner, M.; Watson, M. D.; Winzen, S.; De Oliveira, T. E.; Marques, C. M.; Kremer, K. Relating Side Chain Organization of PNIPAm with Its Conformation in Aqueous Methanol. *Soft Matter* **2016**, *12* (38), 7995–8003.
- (29) Aseyev, V.; Tenhu, H.; Winnik, F. M. Non-Ionic Thermoresponsive Polymers in Water. *Advances in Polymer Science.* 2011, pp 29–89.
- (30) Boutris, C.; Chatzi, E. G.; Kiparissides, C. Characterization of the LCST Behaviour of Aqueous Poly(N-Isopropylacrylamide) Solutions by Thermal and Cloud Point Techniques. *Polymer (Guildf).* **1997**, *38* (10), 2567–2570.
- (31) Lutz, J. F. Polymerization of Oligo(Ethylene Glycol) (Meth)Acrylates: Toward New Generations of Smart Biocompatible Materials. *J. Polym. Sci. Part A Polym. Chem.* **2008**, *46* (11), 3459–3470.
- (32) Masson, P.; Beinert, G.; Franta, E.; Rempp, P. Synthesis of Polyethylene Oxide Macromers. *Polym. Bull.* **1982**, *7* (1), 17–22.
- (33) Hu, Z.; Cai, T.; Chi, C. Thermoresponsive Oligo(Ethylene Glycol)-Methacrylate- Based Polymers and Microgels. *Soft Matter* **2010**, *6* (10), 2115–2123.
- (34) Bergfelt, A.; Rubatat, L.; Brandell, D.; Bowden, T. Poly(Benzyl Methacrylate)-Poly[(Oligo Ethylene Glycol) Methyl Ether Methacrylate] Triblock-Copolymers as Solid Electrolyte for Lithium Batteries. *Solid State Ionics* **2018**, *321*, 55–61.
- (35) Xu, F.; Lam, A.; Pan, Z.; Randhawa, G.; Lamb, M.; Sheardown, H.; Hoare, T. Fast Thermoresponsive Poly(Oligoethylene Glycol Methacrylate) (POEGMA)-Based Nanostructured Hydrogels for Reversible Tuning of Cell



- Interactions. *ACS Biomater. Sci. Eng.* **2021**, 7 (9), 4258–4268.
- (36) Lutz, J. F.; Hoth, A. Preparation of Ideal PEG Analogues with a Tunable Thermosensitivity by Controlled Radical Copolymerization of 2-(2-Methoxyethoxy)Ethyl Methacrylate and Oligo(Ethylene Glycol) Methacrylate. *Macromolecules* **2006**, 39 (2), 893–896.
- (37) Hua, F.; Jiang, X.; Li, D.; Zhao, B. Well-Defined Thermosensitive, Water-Soluble Polyacrylates and Polystyrenics with Short Pendant Oligo (Ethylene Glycol) Groups Synthesized by Nitroxide-Mediated Radical Polymerization. *J. Polym. Sci. Part A Polym. Chem.* **2006**, 44 (8), 2454–2467.
- (38) Grimm, O.; Maßmann, S. C.; Schacher, F. H. Synthesis and Solution Behaviour of Dual Light- and Temperature-Responsive Poly(Triethylene Glycol-: Co - Spiropyran) Copolymers and Block Copolymers. *Polym. Chem.* **2019**, 10 (21), 2674–2685.
- (39) Mohammadzadeh, A.; Ghafouri Taleghani, H.; Lashkenari, M. S. Preparation and Comparative Study of Anticorrosion Nanocomposites of Polyaniline/Graphene Oxide/Clay Coating. *J. Mater. Res. Technol.* **2021**, 13, 2325–2335.
- (40) Mccook, N. L.; Burris, D. L.; Bourne, G. R.; Steffens, J.; Hanrahan, J. R.; Sawyer, W. G. Wear Resistant Solid Lubricant Coating Made from PTFE and Epoxy.
- (41) Lee, H.; Alcaraz, M. L.; Rubner, M. F.; Cohen, R. E. Zwitter-Wettability and Antifogging Coatings with Frost-Resisting Capabilities. *ACS Nano* **2013**, 7 (3), 2172–2185.
- (42) Bode, S.; Zedler, L.; Schacher, F. H.; Dietzek, B.; Schmitt, M.; Popp, J.; Hager, M. D.; Schubert, U. S.; Bode, S.; Schacher, F. H.; Hager, M. D.; Schubert, U. S.; Zedler, L.; Dietzek, B.; Schmitt, M.; Popp, J. Self-Healing Polymer Coatings Based on Crosslinked Metallosupramolecular Copolymers. *Adv. Mater.* **2013**, 25 (11), 1634–1638.
- (43) Das, S.; Kumar, S.; Samal, S. K.; Mohanty, S.; Nayak, S. K. A Review on Superhydrophobic Polymer Nanocoatings: Recent Development and Applications. *Industrial and Engineering Chemistry Research*. American Chemical Society February 28, 2018, pp 2727–2745.
- (44) Léger, L.; Raphaël, E.; Hervet, H. Surface-Anchored Polymer Chains: Their Role in Adhesion and Friction. *Adv. Polym. Sci.* **1999**, 138, 186–225.
- (45) Singh, M.; Kaur, N.; Comini, E. The Role of Self-Assembled Monolayers in Electronic Devices. *J. Mater. Chem. C* **2020**, 8 (12), 3938–3955.
- (46) Weinstein, S. J.; Ruschak, K. J. Coating Flows. *Annu. Rev. Fluid Mech.* **2004**,

36, 29–53.

- (47) Embs, F.; Funhoff, D.; Laschewsky, A.; Licht, U.; Ohst, H.; Prass, W.; Ringsdorf, H.; Wegner, G.; Wehrmann, R. Preformed Polymers for Langmuir–Blodgett Films– Molecular Concepts. *Adv. Mater.* **1991**, *3* (1), 25–31.
- (48) Chen, W.; McCarthy, T. J. Layer-by-Layer Deposition: A Tool for Polymer Surface Modification. *Macromolecules* **1997**, *30* (1), 78–86.
- (49) González, N.; Elvira, C.; San Román, J.; Cifuentes, A. New Physically Adsorbed Polymer Coating for Reproducible Separations of Basic and Acidic Proteins by Capillary Electrophoresis. *J. Chromatogr. A* **2003**, *1012* (1), 95–101.
- (50) Källrot, N.; Dahlqvist, M.; Linse, P. Dynamics of Polymer Adsorption from Bulk Solution onto Planar Surfaces. *Macromolecules* **2009**, *42* (10), 3641–3649.
- (51) Scheutjens, J. M. H. M.; Fleer, G. J. Statistical Theory of the Adsorption of Interacting Chain Molecules. 2. Train, Loop, and Tail Size Distribution. *J. Phys. Chem.* **1980**, *84* (2), 178–190.
- (52) O’Shaughnessy, B.; Vavylonis, D. Irreversible Adsorption from Dilute Polymer Solutions. *Eur. Phys. J. E* **2003**, *11* (3), 213–230.
- (53) Sims, R. A.; Harmer, S. L.; Quinton, J. S. The Role of Physisorption and Chemisorption in the Oscillatory Adsorption of Organosilanes on Aluminium Oxide. *Polymers (Basel)*. **2019**, *11* (3).
- (54) Porus, M.; Maroni, P.; Borkovec, M. Structure of Adsorbed Polyelectrolyte Monolayers Investigated by Combining Optical Reflectometry and Piezoelectric Techniques. *Langmuir* **2012**, *28* (13), 5642–5651.
- (55) Roach, P.; Farrar, D.; Perry, C. C. Interpretation of Protein Adsorption: Surface-Induced Conformational Changes. *J. Am. Chem. Soc.* **2005**, *127* (22), 8168–8173.
- (56) Wondraczek, L.; Pohnert, G.; Schacher, F. H.; Köhler, A.; Gottschaldt, M.; Schubert, U. S.; Küsel, K.; Brakhage, A. A. Artificial Microbial Arenas: Materials for Observing and Manipulating Microbial Consortia. *Adv. Mater.* **2019**, *31* (24).
- (57) Chollet, B.; Li, M.; Martwong, E.; Bresson, B.; Fretigny, C.; Tabeling, P.; Tran, Y. Multiscale Surface-Attached Hydrogel Thin Films with Tailored Architecture. *ACS Appl. Mater. Interfaces* **2016**, *8* (18), 11729–11738.
- (58) Yu, L.; Schlaich, C.; Hou, Y.; Zhang, J.; Noeske, P. L. M.; Haag, R. Photoregulating Antifouling and Bioadhesion Functional Coating Surface Based on Spiropyran. *Chem. - A Eur. J.* **2018**, *24* (30), 7742–7748.

- (59) Shi, X.; Ye, Y.; Wang, H.; Liu, F.; Wang, Z. Designing PH-Responsive Biodegradable Polymer Coatings for Controlled Drug Release via Vapor-Based Route. *ACS Appl. Mater. Interfaces* **2018**, *10* (44), 38449–38458.
- (60) Ahmed, S. T.; Madinya, J. J.; Leckband, D. E. Ionic Strength Dependent Forces between End-Grafted Poly(Sulfobetaine) Films and Mica. *J. Colloid Interface Sci.* **2022**, *606*, 298–306.
- (61) Schenning, S. A. P. H. J.; Esteves, A. C. C.; Schiphorst, J. Ter; Van Den Broek, M.; De Koning, T.; Murphy, J. N.; Schenning, A. P. H. J. As Featured in: Materials A Dual Light and Temperature Responsive Cotton Fabric Functionalized with a Surface-Grafted Spiropyran-NIPAAm-Hydrogel †. **2016**.
- (62) Osypova, A.; Magnin, D.; Sibret, P.; Aqil, A.; Jérôme, C.; Dupont-Gillain, C.; Pradier, C. M.; Demoustier-Champagne, S.; Landoulsi, J. Dual Stimuli-Responsive Coating Designed through Layer-by-Layer Assembly of PAA-b-PNIPAM Block Copolymers for the Control of Protein Adsorption. *Soft Matter* **2015**, *11* (41), 8154–8164.
- (63) Aguilar, M. R.; San Román, J. *Smart Polymers and Their Applications*, 2nd ed.; Aguilar, M. R., San Román, J., Eds.; Elsevier, 2019.
- (64) Löwenbein, A.; Katz, W. Über Substituierte *Spiro* -Dibenzopyrane. *Berichte der Dtsch. Chem. Gesellschaft (A B Ser.)* **1926**, *59* (7), 1377–1383.
- (65) Hartley, G. The Cis Form of Azobenene. *Nature* **1937**, *14*, 281.
- (66) Irie, M.; Mohri, M. Thermally Irreversible Photochromic Systems. Reversible Photocyclization of Diarylethene Derivatives. *J. Org. Chem.* **1988**, *53* (4), 803–808.
- (67) Klajn, R. Spiropyran-Based Dynamic Materials. *Chem. Soc. Rev.* **2014**, *43* (1), 148–184.
- (68) Levitus, M.; Glasser, G.; Neher, D.; Aramendía, P. F. Direct Measurement of the Dipole Moment of a Metastable Merocyanine by Electromechanical Interferometry. *Chem. Phys. Lett.* **1997**, *277* (1–3), 118–124.
- (69) Nezhadghaffar-Borhani, E.; Abdollahi, A.; Roghani-Mamaqani, H.; Salami-Kalajahi, M. Photoswitchable Surface Wettability of Ultrahydrophobic Nanofibrous Coatings Composed of Spiropyran-Acrylic Copolymers. *J. Colloid Interface Sci.* **2021**, *593*, 67–78..
- (70) Dübner, M.; Naoum, M. E.; Spencer, N. D.; Padeste, C. From PH- to Light-Response: Postpolymerization Modification of Polymer Brushes Grafted onto Microporous Polymeric Membranes. *ACS Omega* **2017**, *2* (2), 455–461.
- (71) Euchler, D.; Ehgartner, C. R.; Hü, N.; Feinle, A. Monolithic Spiropyran-Based

Porous Polysilsesquioxanes with Stimulus-Responsive Properties. *Cite This ACS Appl. Mater. Interfaces* **2020**, *12*, 47762.

- (72) Zachariasen, W. H. The Atomic Arrangement in Glass. *J. Am. Chem. Soc.* **1932**, *54* (10), 3841–3851.
- (73) Greaves, G. N.; Sen, S. Inorganic Glasses, Glass-Forming Liquids and Amorphizing Solids. *Advances in Physics*. Taylor & Francis Group January 2007, pp 1–166.
- (74) Hodge, I. M. Physical Aging in Polymer Glasses. *Science (80-. )*. **1995**, *267* (5206), 1945–1947.
- (75) Miracle, D. B. A Structural Model for Metallic Glasses. *Nat. Mater.* **2004**, *3* (10), 697–702.
- (76) Nozari, V.; Calahoo, C.; Tuffnell, J. M.; Keen, D. A.; Wondraczek, L.; Bennett, T. D. Ionic Liquid Facilitated Melting of the Metal-Organic Framework ZIF-8. *Nat. Commun.* **2021**, *12* (2021), 1–13.
- (77) Ediger, M. D. Perspective: Highly Stable Vapor-Deposited Glasses. *J. Chem. Phys.* **2017**, *147* (21).
- (78) Shames, A.; Lev, O.; Iosefzon-Kuyavskaya, B. Study of Sol-Gel Glass Formation and Properties by Paramagnetic Probes. *J. Non. Cryst. Solids* **1993**, *163* (2), 105–114.
- (79) Krätchmer, W.; Huffman, D. R. Infrared Extinction of Heavy Ion Irradiated and Amorphous Olivine, with Applications to Interstellar Dust. *Astrophys. Sp. Sci. 1979 611* **1979**, *61* (1), 195–203.
- (80) Palenta, T.; Fuhrmann, S.; Greaves, G. N.; Schwieger, W.; Wondraczek, L. Thermal Collapse and Hierarchy of Polymorphs in a Faujasite-Type Zeolite and Its Analogous Melt-Quenched Glass. *J. Chem. Phys.* **2015**, *142* (8).
- (81) Kotz, F.; Arnold, K.; Bauer, W.; Schild, D.; Keller, N.; Sachsenheimer, K.; Nargang, T. M.; Richter, C.; Helmer, D.; Rapp, B. E. Three-Dimensional Printing of Transparent Fused Silica Glass. *Nature* **2017**, *544* (7650), 337–339.
- (82) Gupta, P. K. Non-Crystalline Solids: Glasses and Amorphous Solids. *J. Non. Cryst. Solids* **1996**, *195* (1–2), 158–164.
- (83) Zachariasen, W. H. The Atomic Arrangement in Glass. *J. Am. Chem. Soc.* **1932**, *54* (10), 3841–3851.
- (84) Ediger, M. D.; Angell, C. A.; Nagel, S. R. Supercooled Liquids and Glasses. *J. Phys. Chem.* **1996**, *100* (31), 13200–13212.
- (85) Angell, C. A. Formation of Glasses from Liquids and Biopolymers. *Science (80-. )*. **1995**, *267* (5206), 1924–1935.

- (86) Kauzmann, W. The Nature of the Glassy State and the Behavior of Liquids at Low Temperatures. *Chem. Rev.* **1948**, *43* (2), 219–256.
- (87) Berthier, L.; Biroli, G. Theoretical Perspective on the Glass Transition and Amorphous Materials. *Rev. Mod. Phys.* **2011**, *83* (2), 587–645.
- (88) Mason, T. G.; Weitz, D. A. Linear Viscoelasticity of Colloidal Hard Sphere Suspensions near the Glass Transition. *Phys. Rev. Lett.* **1995**, *75* (14), 2770–2773.
- (89) Sarangapani, P. S.; Schofield, A. B.; Zhu, Y. Direct Experimental Evidence of Growing Dynamic Length Scales in Confined Colloidal Liquids. *Phys. Rev. E - Stat. Nonlinear, Soft Matter Phys.* **2011**, *83* (3), 2–5.
- (90) Philippe, A. M.; Truzzolillo, D.; Galvan-Myoshi, J.; Dieudonné-George, P.; Trappe, V.; Berthier, L.; Cipelletti, L. Glass Transition of Soft Colloids. *Phys. Rev. E* **2018**, *97* (4), 1–5.
- (91) Lindsay, H. M.; Chaikin, P. M. Elastic Properties of Colloidal Crystals and Glasses. *J. Chem. Phys.* **1998**, *76* (7), 3774.
- (92) Lappala, A.; Sefton, L.; Fenimore, P. W.; Terentjev, E. M. Connectivity and Free-Surface Effects in Polymer Glasses. *Sci. Rep.* **2019**, *9* (1), 1–10.
- (93) Weeks, E. R.; Crocker, J. C.; Levitt, A. C.; Schofield, A.; Weitz, D. A. Three-Dimensional Direct Imaging of Structural Relaxation near the Colloidal Glass Transition. *Science (80-. )*. **2000**, *287* (5453), 627–631.
- (94) Ghosh, A.; Chikkadi, V. K.; Schall, P.; Kurchan, J.; Bonn, D. Density of States of Colloidal Glasses. *Phys. Rev. Lett.* **2010**, *104* (24), 2–5.
- (95) Hunter, G. L.; Weeks, E. R. The Physics of the Colloidal Glass Transition. *Reports Prog. Phys.* **2012**, *75* (6).
- (96) Mason, J.; Bernal, J. Packing of Spheres: Co-Ordination of Randomly Packed Spheres. *Nature* **1960**, *188* (4754), 910–911.
- (97) P. N. Pusey; Mejen, W. van. Phase Behaviour of Concentrated Suspensions of Nearly Colloidal Spheres. *Nature* **1986**, 2–4.
- (98) Zaccarelli, E. Colloidal Gels: Equilibrium and Non-Equilibrium Routes. *J. Phys. Condens. Matter* **2007**, *19* (32).
- (99) Reichman, D. R.; Charbonneau, P. Mode-Coupling Theory. *J. Stat. Mech. Theory Exp.* **2005**, No. 5, 267–289.
- (100) Kohlrausch, R. Theorie Des Elektrischen Rückstandes in Der Leidener Flasche. *Ann. Phys.* **1854**, *167* (2), 179–214.
- (101) Williams, G.; Watts, D. C. Non-Symmetrical Dielectric Relaxation Behaviour Arising from a Simple Empirical Decay Function. *Trans. Faraday Soc.* **1970**,

66 (0), 80–85.

- (102) Phillips, J. C. Stretched Exponential Relaxation in Molecular and Electronic Glasses. *Reports Prog. Phys.* **1996**, *59* (9), 1133–1207.
- (103) Sastry, S.; Debenedetti, P. G.; Stillinger, F. H. Signatures of Distinct Dynamical Regimes in the Energy Landscape of a Glass-Forming Liquid. *Nature* **1998**, *393* (6685), 554–557.
- (104) Marcus, A. H.; Schofield, J.; Rice, S. A. Experimental Observations of Non-Gaussian Behavior and Stringlike Cooperative Dynamics in Concentrated Quasi-Two-Dimensional Colloidal Liquids. **1999**.
- (105) Weeks, E. R.; Weitz, D. A. Properties of Cage Rearrangements Observed near the Colloidal Glass Transition. *Phys. Rev. Lett.* **2002**, *89* (9), 1–4.
- (106) Caronna, C.; Chushkin, Y.; Madsen, A.; Cupane, A. Dynamics of Nanoparticles in a Supercooled Liquid. *Phys. Rev. Lett.* **2008**, *100* (5), 8–11.
- (107) Jang, W. S.; Koo, P.; Bryson, K.; Narayanan, S.; Sandy, A.; Russell, T. P.; Mochrie, S. G. Dynamics of Cadmium Sulfide Nanoparticles within Polystyrene Melts. *Macromolecules* **2014**, *47* (18), 6483–6490.
- (108) Guo, H.; Wilking, J. N.; Liang, D.; Mason, T. G.; Harden, J. L.; Leheny, R. L. Slow, Nondiffusive Dynamics in Concentrated Nanoemulsions. *Phys. Rev. E - Stat. Nonlinear, Soft Matter Phys.* **2007**, *75* (4), 1–8.
- (109) Bouchaud, J. P.; Pitard, E. Anomalous Dynamical Light Scattering in Soft Glassy Gels. *Eur. Phys. J. E* **2001**, *6* (3), 231–236.
- (110) Huang, Y.; Paul, D. R. Physical Aging of Thin Glassy Polymer Films Monitored by Gas Permeability. *Polymer (Guildf)*. **2004**, *45* (25), 8377–8393.
- (111) Ding, Y.; Wook Ro, H.; Germer, T. A.; Douglas, J. F.; Okerberg, B. C.; Karim, A.; Soles, C. L. Relaxation Behavior of Polymer Structures Fabricated by Nanoimprint Lithography. *ACS Nano* **2007**, *1* (2), 84–92.
- (112) Paul, D. R.; Robeson, L. M. Polymer Nanotechnology: Nanocomposites. *Polymer (Guildf)*. **2008**, *49* (15), 3187–3204.
- (113) Keddie, J. L.; Jones, R. A. L.; Cory, R. A. Size-Dependent Depression of the Glass Transition Temperature in Polymer Films. *Epl* **1994**, *27* (1), 59–64.
- (114) Fukao, K.; Miyamoto, Y. Glass Transition Temperature and Dynamics of  $\alpha$ -Process in Thin Polymer Films. *Europhys. Lett.* **1999**, *46* (5), 649–654. <https://doi.org/10.1209/epl/i1999-00309-6>.
- (115) Miyazaki, T.; Nishida, K.; Kanaya, T. Thermal Expansion Behavior of Ultrathin Polymer Films Supported on Silicon Substrate. *Phys. Rev. E - Stat. Physics, Plasmas, Fluids, Relat. Interdiscip. Top.* **2004**, *69* (6), 6.

- (116) Priestley, R. D.; Ellison, C. J.; Broadbelt, L. J.; Torkelson, J. M. Materials Science: Structural Relaxation of Polymer Glasses at Surfaces, Interfaces, and in Between. *Science* (80-. ). **2005**, *309* (5733), 456–459.
- (117) Ellison, C. J.; Torkelson, J. M. The Distribution of Glass-Transition Temperatures in Nanoscopically Confined Glass Formers. *Nat. Mater.* **2003**, *2* (10), 695–700.
- (118) Yang, C.; Takahashi, I. Broadening, No Broadening and Narrowing of Glass Transition of Supported Polystyrene Ultrathin Films Emerging under Ultraslow Temperature Variations. *Polym. J.* **2011**, *43* (4), 390–397.
- (119) Wallace, W. E.; Van Zanten, J. H.; Wu, W. L. Influence of an Impenetrable Interface on a Polymer Glass-Transition Temperature. *Phys. Rev. E* **1995**, *52* (4).
- (120) Reiter, G. Mobility of Polymers in Films Thinner than Their Unperturbed Size. *Epl* **1993**, *23* (8), 579–584.
- (121) Eral, H. B.; Oh, J. M.; Van Den Ende, D.; Mugele, F.; Duits, M. H. G. Anisotropic and Hindered Diffusion of Colloidal Particles in a Closed Cylinder. *Langmuir* **2010**, *26* (22), 16722–16729.
- (122) Edmond, K. V.; Nugent, C. R.; Weeks, E. R. Influence of Confinement on Dynamical Heterogeneities in Dense Colloidal Samples. *Phys. Rev. E - Stat. Nonlinear, Soft Matter Phys.* **2012**, *85* (4), 1–10.
- (123) Sarangapani, P. S.; Yu, Y.; Zhao, J.; Zhu, Y. Direct Visualization of Colloidal Gelation under Confinement. *Phys. Rev. E - Stat. Nonlinear, Soft Matter Phys.* **2008**, *77* (6), 1–7.
- (124) Johannsmann, D.; Mathauer, K.; Wegner, G.; Knoll, W. Viscoelastic Properties of Thin Films Probed with a Quartz-Crystal Resonator. *Phys. Rev. B* **1992**, *46* (12), 7808–7815.
- (125) Challis, R. E.; Wilkinson, G. P.; Freemantle, R. J. Errors and Uncertainties in the Ultrasonic Pulse-Echo Reflectometry Method for Measuring Acoustic Impedance. *Meas. Sci. Technol.* **1998**, *9* (4), 692–700.
- (126) Wang, P.; Fang, J.; Qin, S.; Kang, Y.; Zhu, D. M. Molecular Weight Dependence of Viscosity and Shear Modulus of Polyethylene Glycol (PEG) Solution Boundary Layers. *J. Phys. Chem. C* **2009**, *113* (31), 13793–13800.
- (127) Hossenlpp, J.; Jiang, L.; Cernosek, R.; Josse, F. Characterization of Epoxy Resin (SU-8) Film Using Thickness-Shear Mode (TSM) Resonator under Various Conditions. *J. Polym. Sci. Part B Polym. Phys.* **2004**, *42* (12), 2373–2384.
- (128) Szántó, L.; Vogt, R.; Meier, J.; Auhl, D.; Van Ruymbeke, E.; Friedrich, C.

Entanglement Relaxation Time of Polyethylene Melts from High-Frequency Rheometry in the Mega-Hertz Range. *J. Rheol. (N. Y. N. Y.)* **2017**, *61* (5), 1023–1033.

- (129) Denolf, G. C.; Sturdy, L. F.; Shull, K. R. High-Frequency Rheological Characterization of Homogeneous Polymer Films with the Quartz Crystal Microbalance. *Langmuir* **2014**, *30* (32), 9731–9740.
- (130) Sauerbrey, G. Verwendung von Schwingquarzen Zur Wägung Dünner Schichten Und Zur Mikrowägung. *Zeitschrift für Phys.* **1959**, *155* (2), 206–222.
- (131) Johnson, J. E. Aluminum Antimonide Thin Films by Coevaporation of the Elements. *J. Appl. Phys.* **1965**, *36* (10), 3193–3195.
- (132) Kanazawa, K. K.; Gordon, J. G. Frequency of a Quartz Microbalance in Contact with Liquid. *Anal. Chem.* **1985**.
- (133) Johannsmann, D. Viscoelastic Analysis of Organic Thin Films on Quartz Resonators. *Macromol. Chem. Phys.* **1999**, *200* (3), 501–516.
- (134) Rodahl, M.; Kasemo, B. A Simple Setup to Simultaneously Measure the Resonant Frequency and the Absolute Dissipation Factor of a Quartz Crystal Microbalance. *Rev. Sci. Instrum.* **1996**, *67* (9), 3238–3241.
- (135) Alf, M. E.; Godfrin, P. D.; Hatton, T. A.; Gleason, K. K. Sharp Hydrophilicity Switching and Conformality on Nanostructured Surfaces Prepared via Initiated Chemical Vapor Deposition (ICVD) of a Novel Thermally Responsive Copolymer. *Macromol. Rapid Commun.* **2010**, *31* (24), 2166–2172.
- (136) Kasai, N.; Sugimoto, I. Effects of Aging on Radiofrequency-Sputtered Polyethylene Film. *J Appl Polym Sci* **1999**, *73*, 1869–1877.
- (137) Sturdy, L. F.; Wright, M. S.; Yee, A.; Casadio, F.; Faber, K. T.; Shull, K. R. Effects of Zinc Oxide Filler on the Curing and Mechanical Response of Alkyd Coatings. *Polymer (Guildf)*. **2020**, *191*, 122222.
- (138) Höök, F.; Rodahl, M.; Brzezinski, P.; Kasemo, B. Energy Dissipation Kinetics for Protein and Antibody-Antigen Adsorption under Shear Oscillation on a Quartz Crystal Microbalance. *Langmuir* **1998**, *14* (4), 729–734.
- (139) Denolf, G. C.; Sturdy, L. F.; Shull, K. R. High-Frequency Rheological Characterization of Homogeneous Polymer Films with the Quartz Crystal Microbalance. **2014**.
- (140) Martin, S. J.; Frye, G. C.; Ricco, A. J.; Senturia, S. D. Effect of Surface Roughness on the Response of Thickness-Shear Mode Resonators in Liquids. *Anal. Chem.* **1993**, *65* (20), 2910–2922.



- (141) Johannsmann, D.; Langhoff, A.; Leppin, C. Studying Soft Interfaces with Shear Waves: Principles and Applications of the Quartz Crystal Microbalance (QCM). *Sensors (Basel)*. **2021**, *21* (10).
- (142) Rodahl, M.; Kasemo, B. On the Measurement of Thin Liquid Overlayers with the Quartz-Crystal Microbalance. *Int. Conf. Solid-State Sensors Actuators, Eurosensors IX, Proc.* **1995**, *2*, 743–746.
- (143) Johannsmann, D. Viscoelastic, Mechanical, and Dielectric Measurements on Complex Samples with the Quartz Crystal Microbalance. *Phys. Chem. Chem. Phys.* **2008**, *10* (31), 4516–4534.
- (144) Höök, F.; Kasemo, B.; Nylander, T.; Fant, C.; Sott, K.; Elwing, H. Variations in Coupled Water, Viscoelastic Properties, and Film Thickness of a Mefp-1 Protein Film during Adsorption and Cross-Linking: A Quartz Crystal Microbalance with Dissipation Monitoring, Ellipsometry, and Surface Plasmon Resonance Study. *Anal. Chem.* **2001**, *73* (24), 5796–5804.
- (145) Krim, J.; Widom, A. Damping of a Crystal Oscillator by an Adsorbed Monolayer and Its Relation to Interfacial Viscosity. *38*, 15–1988.
- (146) Wehner, S.; Wondraczek, K.; Johannsmann, D.; Bund, A. Roughness-Induced Acoustic Second-Harmonic Generation during Electrochemical Metal Deposition on the Quartz-Crystal Microbalance. *Langmuir* **2004**, *20* (6), 2356–2360.
- (147) Wondraczek, K.; Bund, A.; Johannsmann, D. Acoustic Second Harmonic Generation from Rough Surfaces under Shear Excitation in Liquids. *Langmuir* **2004**, *20* (23), 10346–10350.
- (148) Daikhin, L.; Gileadi, E.; Katz, G.; Tsionsky, V.; Urbakh, M.; Zagidulin, D. Influence of Roughness on the Admittance of the Quartz Crystal Microbalance Immersed in Liquids. *Anal. Chem.* **2002**, *74* (3), 554–561.
- (149) Lack, F. R.; Willard, G. W.; Fair, I. E. Some Improvements in Quartz Crystal Circuit Elements. *Bell Syst. Tech. J.* **1934**, *13* (3), 453–463.
- (150) Dixon, M.; Gormally, M.; Johal, M. Real-Time Characterization of Polymer Film Degradation with Quartz Crystal Microbalance with Dissipation Monitoring. *Nanotechnol. 2009 Fabr. Part. Charact. MEMS, Electron. Photonics - Tech. Proc. 2009 NSTI Nanotechnol. Conf. Expo, NSTI-Nanotech 2009* **2009**, *1*, 364–367.
- (151) Heeb, R.; Bielecki, R. M.; Lee, S.; Spencer, N. D. Room-Temperature, Aqueous-Phase Fabrication of Poly(Methacrylic Acid) Brushes by UV-LED-Induced, Controlled Radical Polymerization with High Selectivity for Surface-Bound Species. *Macromolecules* **2009**, *42* (22), 9124–9132.

- (152) Benkoski, J. J.; Jesorka, A.; Kasemo, B.; Höök, F. Light-Activated Desorption of Photoactive Polyelectrolytes from Supported Lipid Bilayers. *Macromolecules* **2005**, *38* (9), 3852–3860.
- (153) Goldberg, W. I. Dynamic Light Scattering Dynamic Light Scattering. *Am. J. Phys.* **1999**, *67* (12), 1152–1160.
- (154) Stetefeld, J.; McKenna, S. A.; Patel, T. R. Dynamic Light Scattering: A Practical Guide and Applications in Biomedical Sciences. *Biophys. Rev.* **2016**, *8* (4), 409–427.
- (155) Gorelov, A. V.; Du Chesne, A.; Dawson, K. A. Phase Separation in Dilute Solutions of Poly (N-Isopropylacrylamide). *Phys. A Stat. Mech. its Appl.* **1997**, *240* (3–4), 443–452.
- (156) Zhu, P. W.; Napper, D. H. The Longer Time Collapse Kinetics of Interfacial Poly(N-Isopropylacrylamide) in Water. *J. Chem. Phys.* **1997**, *106* (15), 6492–6498.
- (157) Lutz, J. F.; Weichenhan, K.; Akdemir, Ö.; Hoth, A. About the Phase Transitions in Aqueous Solutions of Thermoresponsive Copolymers and Hydrogels Based on 2-(2-Methoxyethoxy)Ethyl Methacrylate and Oligo(Ethylene Glycol) Methacrylate. *Macromolecules* **2007**, *40* (7), 2503–2508.
- (158) Einstein, A. Über Die von Der Molekularkinetischen Theorie Der Wärme Geforderte Bewegung von in Ruhenden Flüssigkeiten Suspendierten Teilchen. *Ann. d. Phys.* **1905**, *322* (8), 549–560.
- (159) Einstein, A. Zur Theorie Der Brownschen Bewegung. *Ann. Phys.* **1906**, *324* (2), 371–381.
- (160) Pecora, R. Doppler Shifts in Light Scattering from Pure Liquids and Polymer Solutions. *J. Chem. Phys.* **1964**, *40* (6), 1604–1614.
- (161) Peppas, N. A.; Hilt, J. Z.; Khademhosseini, A.; Langer, R. Hydrogels in Biology and Medicine: From Molecular Principles to Bionanotechnology. *Adv. Mater.* **2006**, *18* (11), 1345–1360.
- (162) Zhang, G. Study on Conformation Change of Thermally Sensitive Linear Grafted Poly(N-Isopropylacrylamide) Chains by Quartz Crystal Microbalance. *Macromolecules* **2004**, *37* (17), 6553–6557.
- (163) Liu, G.; Zhang, G. Collapse and Swelling of Thermally Sensitive Poly (N-Isopropylacrylamide) Brushes Monitored with a Quartz Crystal Microbalance. *J. Phys. Chem. B* **2005**, *109* (2), 743–747. <https://doi.org/10.1021/jp046903m>.
- (164) Plunkett, M. A.; Wang, Z.; Rutland, M. W.; Johannsmann, D. Adsorption of PNIPAM Layers on Hydrophobic Gold Surfaces, Measured in Situ by QCM

- and SPR. *Langmuir* **2003**, *19* (17), 6837–6844.
- (165) Wu, B.; Wu, K.; Wang, P.; Zhu, D. M. Adsorption Kinetics and Adsorption Isotherm of Poly(N-Isopropylacrylamide) on Gold Surfaces Studied Using QCM-D. *J. Phys. Chem. C* **2007**, *111* (3), 1131–1135..
- (166) Chen, T.; Lu, Y.; Chen, T.; Zhang, X.; Du, B. Adsorption of PNIPAmx-PEO20-PPO70-PEO 20-PNIPAmx Pentablock Terpolymer on Gold Surfaces: Effects of Concentration, Temperature, Block Length, and Surface Properties. *Phys. Chem. Chem. Phys.* **2014**, *16* (12), 5536–5544.
- (167) Guo, Y.; Wang, D.; Yang, L.; Liu, S. Nanoscale Monolayer Adsorption of Polyelectrolytes at the Solid/Liquid Interface Observed by Quartz Crystal Microbalance. *Polym. J.* **2017**, *49* (7), 543–548.
- (168) Edahiro, J. ichi; Sumaru, K.; Takagi, T.; Shinbo, T.; Kanamori, T.; Sudoh, M. Analysis of Photo-Induced Hydration of a Photochromic Poly(N-Isopropylacrylamide) - Spiropyran Copolymer Thin Layer by Quartz Crystal Microbalance. *Eur. Polym. J.* **2008**, *44* (2), 300–307.
- (169) Tay, A.; Bendejacq, D.; Monteux, C.; Lequeux, F. How Does Water Wet a Hydrosoluble Substrate? *Soft Matter* **2011**, *7* (15), 6953–6957.
- (170) Voinova, M. V.; Jonson, M.; Kasemo, B. On Dissipation of Quartz Crystal Microbalance as a Mechanical Spectroscopy Tool. *Spectroscopy* **2004**, *18* (4), 537–544.
- (171) Lessard, D. G.; Ousalem, M.; Zhu, X. X.; Eisenberg, A.; Carreau, P. J. Study of the Phase Transition of Poly(n,n-Diethylacrylamide) in Water by Rheology and Dynamic Light Scattering. *J. Polym. Sci. Part B Polym. Phys.* **2003**, *41* (14), 1627–1637.
- (172) Kujawa, P.; Aseyev, V.; Tenhu, H.; Winnik, F. M. Temperature-Sensitive Properties of Poly(N-Isopropylacrylamide) Mesoglobules Formed in Dilute Aqueous Solutions Heated above Their Demixing Point. *Macromolecules* **2006**, *39* (22), 7686–7693.
- (173) Israelachvili, J. Commentary The Different Faces of Poly ( Ethylene Glycol ). *Proc. Natl. Acad. Sci.* **1997**, *94* (August), 8378–8379.
- (174) Begum, R.; Matsuura, H. Conformational Properties of Short Poly(Oxyethylene) Chains in Water Studied by IR Spectroscopy. *J. Chem. Soc. - Faraday Trans.* **1997**, *93* (21), 3839–3848.
- (175) Lutz, J. F.; Akdemir, Ö.; Hoth, A. Point by Point Comparison of Two Thermosensitive Polymers Exhibiting a Similar LCST: Is the Age of Poly(NIPAM) Over? *J. Am. Chem. Soc.* **2006**, *128* (40), 13046–13047.
- (176) Judah, H. L.; Liu, P.; Zarbakhsh, A.; Resmini, M. Influence of Buffers, Ionic

- Strength, and Ph on the Volume Phase Transition Behavior of Acrylamide-Based Nanogels. *Polymers (Basel)*. **2020**, *12* (11), 1–14.
- (177) Chevallier, E.; Mamane, A.; Stone, H. A.; Tribet, C.; Lequeux, F.; Monteux, C. Pumping-out Photo-Surfactants from an Air-Water Interface Using Light. *Soft Matter* **2011**, *7* (17), 7866–7874.
- (178) Johannsmann, D.; Reviakine, I.; Richter, R. P. Dissipation in Films of Adsorbed Nanospheres Studied by Quartz Crystal Microbalance (QCM). *Anal. Chem.* **2009**, *81* (19), 8167–8176.
- (179) Cohen Stuart, M. A.; Waajen, F. H. W. H.; Cosgrove, T.; Vincent, B.; Crowley, T. L. Hydrodynamic Thickness of Adsorbed Polymer Layers. *Macromolecules* **1984**, *17* (9), 1825–1830.
- (180) Plunkett, M. A.; Claesson, P. M.; Rutland, M. W. Adsorption of a Cationic Polyelectrolyte Followed by Surfactant-Induced Swelling, Studied with a Quartz Crystal Microbalance. *Langmuir* **2002**, *18* (4), 1274–1280.
- (181) Domack, A.; Prucker, O.; Rhe, J.; Johannsmann, D. Swelling of a Polymer Brush Probed with a Quartz Crystal Resonator. *Phys. Rev. E - Stat. Physics, Plasmas, Fluids, Relat. Interdiscip. Top.* **1997**, *56* (1 SUPPL. B), 680–689.
- (182) Chakraborty, A. K.; Shaffer, J. S.; Adriani, P. M. On the Existence of Quasi-Two-Dimensional Glasslike Structures at Strongly Interacting Polymer-Solid Interfaces. *Macromolecules* **1991**, *24* (18), 5226–5229.
- (183) Kremer, K. Glassy States of Adsorbed Flexible Polymers and Spread Polymer “Monolayers.” *J. Phys.* **1986**.
- (184) Raviv, U.; Klein, J.; Witten, T. A. The Polymer Mat: Arrested Rebound of a Compressed Polymer Layer. *Eur. Phys. J. E* **2002**.
- (185) Zhu, P. W.; Napper, D. H. Conformational Transitions of Poly(N-Isopropylacrylamide) Chains Loopily Adsorbed at the Surfaces of Poly(N-Tert-Butylacrylamide) Latex Particles in Water. *J. Phys. Chem. B* **1997**, *101* (16), 3155–3160.
- (186) Zhu, P. W.; Napper, D. H. Effects of Thermal History on the Dynamics of Relaxation of Poly([Formula Presented]-Isopropylacrylamide) Adsorbed at Latex Interfaces in Water. *Phys. Rev. E - Stat. Physics, Plasmas, Fluids, Relat. Interdiscip. Top.* **1998**, *57* (3), 3101–3106.
- (187) Cahn, J. W. Critical Point Wetting. *J. Chem. Phys.* **1977**, *66* (8), 3667–3672.
- (188) Kawata, Y.; Yamamoto, T.; Kihara, H.; Yamamura, Y.; Saito, K.; Ohno, K. Unusual Photoresponses in the Upper Critical Solution Temperature of Polymer Solutions Mediated by Changes in Intermolecular Interactions in an Azo-Doped Liquid Crystalline Solvent. *Phys. Chem. Chem. Phys.* **2018**, *20* (8),

5850–5855.

- (189) Jones, R. A. L.; Richards, R. W. *Polymers at Surfaces and Interfaces*; Cambridge University Press: New York, USA, 1999.
- (190) Wiener, C. G.; Weiss, R. A.; Vogt, B. D. Overcoming Confinement Limited Swelling in Hydrogel Thin Films Using Supramolecular Interactions. *Soft Matter* **2014**.
- (191) Pelton, R. Poly(N-Isopropylacrylamide) (PNIPAM) Is Never Hydrophobic. *J. Colloid Interface Sci.* **2010**.
- (192) Mattsson, J.; Wyss, H. M.; Fernandez-Nieves, A.; Miyazaki, K.; Hu, Z.; Reichman, D. R.; Weitz, D. A. Soft Colloids Make Strong Glasses. *Nature* **2009**, *462* (7269), 83–86.
- (193) Van Der Scheer, P.; Van De Laar, T.; Van Der Gucht, J.; Vlassopoulos, D.; Sprakel, J. Fragility and Strength in Nanoparticle Glasses. *ACS Nano* **2017**, *11* (7), 6755–6763.
- (194) Senff, H.; Richtering, W. Temperature Sensitive Microgel Suspensions: Colloidal Phase Behavior and Rheology of Soft Spheres. *J. Chem. Phys.* **1999**, *111* (4), 1705–1711.
- (195) Nigro, V.; Angelini, R.; Bertoldo, M.; Bruni, F.; Ricci, M. A.; Ruzicka, B. Dynamical Behavior of Microgels of Interpenetrated Polymer Networks. *Soft Matter* **2017**, *13* (30), 5185–5193.
- (196) Frenzel, L.; Lehmkuhler, F.; Koof, M.; Lokteva, I.; Grubel, G. The Phase Diagram of Colloidal Silica-PNIPAm Core-Shell Nanogels. *Soft Matter* **2020**, *16* (2), 466–475.
- (197) Afroze, F.; Nies, E.; Berghmans, H. Phase Transitions in the System Poly(N-Isopropylacrylamide)/Water and Swelling Behaviour of the Corresponding Networks. *J. Mol. Struct.* **2000**, *554* (1), 55–68.
- (198) Ishida, N.; Biggs, S. Direct Observation of the Phase Transition for a Poly(N-Isopropylacrylamide) Layer Grafted onto a Solid Surface by AFM and QCM-D. *Langmuir* **2007**, *23* (22), 11083–11088. <https://doi.org/10.1021/la701461b>.
- (199) Zhu, D. M.; Wu, K.; Wu, B.; Wang, P.; Fang, J.; Hou, Y.; Zhang, G. Physisorption of Poly(N-Isopropylacrylamide) in Its Swollen and Collapsed States: Effects of Molecular Conformation and Substrate Interaction. *J. Phys. Chem. C* **2007**, *111* (50), 18679–18686. <https://doi.org/10.1021/jp0756808>.
- (200) Alf, M. E.; Hatton, T. A.; Gleason, K. K. Insights into Thin, Thermally Responsive Polymer Layers through Quartz Crystal Microbalance with Dissipation. *Langmuir* **2011**, *27* (17), 10691–10698.

- (201) Alert, R.; Tierno, P.; Casademunt, J. Formation of Metastable Phases by Spinodal Decomposition. *Nat. Commun.* **2016**, *7*, 1–7.
- (202) Milchev, A.; Binder, K. Anomalous Diffusion and Relaxation of Collapsed Polymer Chains. *Epl* **1994**, *26* (9), 671–676.
- (203) Biswas, C. S.; Patel, V. K.; Vishwakarma, N. K.; Tiwari, V. K.; Maiti, B.; Maiti, P.; Kamigaito, M.; Okamoto, Y.; Ray, B. Effects of Tacticity and Molecular Weight of Poly(N -Isopropylacrylamide) on Its Glass Transition Temperature. *Macromolecules* **2011**, *44* (14), 5822–5824.
- (204) Ilić-Stojanović, S.; Nikolić, L.; Nikolić, V.; Ristić, I.; Budinski-Simendić, J.; Kapor, A.; Nikolić, G. M. The Structure Characterization of Thermosensitive Poly(N-Isopropylacrylamide-Co-2-Hydroxypropyl Methacrylate) Hydrogel. *Polym. Int.* **2014**, *63* (6), 973–981.
- (205) Wu, C.; Wang, X. Globule-to-Coil Transition of a Single Homopolymer Chain in Solution. *Phys. Rev. Lett.* **1998**, *80* (18), 4092–4094.
- (206) Timoshenko, E. G.; Kuznetsov, Y. A. Aggregation Number Distributions and Mesoglobules in Dilute Solutions of Diblock and Triblock Copolymers. *Europhys. Lett.* **2001**, *53* (3), 322–327.
- (207) Chuang, J.; Grosberg, A. Y.; Tanaka, T. Topological Repulsion between Polymer Globules. *J. Chem. Phys.* **2000**, *112* (14), 6434–6442.
- (208) Wang, X.; Qiu, X.; Wu, C. Comparison of the Coil-to-Globule and the Globule-to-Coil Transitions of a Single Poly(N-Isopropylacrylamide) Homopolymer Chain in Water. *Macromolecules* **1998**, *31* (9), 2972–2976.
- (209) Aseyev, V.; Hietala, S.; Laukkanen, A.; Nuopponen, M.; Confortini, O.; Du Prez, F. E.; Tenhu, H. Mesoglobules of Thermoresponsive Polymers in Dilute Aqueous Solutions above the LCST. *Polymer (Guildf)*. **2005**, *46* (18), 7118–7131.
- (210) Alf, M. E.; Hatton, T. A.; Gleason, K. K. Insights into Thin, Thermally Responsive Polymer Layers through Quartz Crystal Microbalance with Dissipation. *Langmuir* **2011**, *27* (17), 10691–10698.
- (211) Linse, P. Effect of Solvent Quality on the Polymer Adsorption from Bulk Solution onto Planar Surfaces. *Soft Matter* **2012**, *8* (19), 5140–5150.
- (212) Monteux, C.; Fuller, G. G.; Bergeron, V. Shear and Dilational Surface Rheology of Oppositely Charged Polyelectrolyte/Surfactant Microgels Adsorbed at the Air-Water Interface. Influence on Foam Stability. *J. Phys. Chem. B* **2004**, *108* (42), 16473–16482.
- (213) Gnan, N.; Zaccarelli, E. The Microscopic Role of Deformation in the Dynamics of Soft Colloids. *Nat. Phys.* **2019**, *15* (7), 683–688.

- (214) Higler, R.; Sprakel, J. Apparent Strength versus Universality in Glasses of Soft Compressible Colloids. *Sci. Rep.* **2018**, *8* (1), 1–12.
- (215) Mohanty, P. S.; Nöjd, S.; Van Gruijthuijsen, K.; Crassous, J. J.; Obiols-Rabasa, M.; Schweins, R.; Stradner, A.; Schurtenberger, P. Interpenetration of Polymeric Microgels at Ultrahigh Densities. *Sci. Rep.* **2017**, *7* (1), 1–12.
- (216) Conley, G. M.; Aebischer, P.; Nöjd, S.; Schurtenberger, P.; Scheffold, F. Jamming and Overpacking Fuzzy Microgels: Deformation, Interpenetration, and Compression. *Sci. Adv.* **2017**, *3* (10), 1–8.
- (217) Czakkel, O.; Madsen, A. Evolution of Dynamics and Structure during Formation of a Cross-Linked Polymer Gel. *Epl* **2011**, *95* (2), 0–6.
- (218) Li, Q.; Peng, X.; McKenna, G. B. Physical Aging and Compressed Exponential Behaviors in a Model Soft Colloidal System. *Soft Matter* **2019**, *15* (11), 2336–2347.
- (219) Wondraczek, L.; Pan, Z.; Palenta, T.; Erlebach, A.; Misture, S. T.; Sierka, M.; Micoulaut, M.; Hoppe, U.; Deubener, J.; Greaves, G. N. Kinetics of Decelerated Melting. *Adv. Sci.* **2018**, *5* (5), 1–8.
- (220) Greaves, G. N.; Meneau, F.; Sapelkin, A.; Colyer, L. M.; Gwynn, I. ap; Wade, S.; Sankar, G. The Rheology of Collapsing Zeolites Amorphized by Temperature and Pressure. *Nat. Mater.* **2003**, *2* (9), 622–629.
- (221) Grinsted, R. A.; Clark, L.; Koenig, J. L. Study of Cyclic Sorption–Desorption into Poly(Methyl Methacrylate) Rods Using NMR Imaging. *Macromolecules* **1992**, *25* (4), 1235–1241.
- (222) Meares, P. The Diffusion of Gases Through Polyvinyl Acetate. *J. Am. Chem. Soc.* **1954**, *76* (13), 3415–3422.
- (223) Long, F. A.; Richman, D. Concentration Gradients for Diffusion of Vapors in Glassy Polymers and Their Relation to Time Dependent Diffusion Phenomena. *J. Am. Chem. Soc.* **1960**, *82* (3), 513–519.
- (224) Thomas, N. L.; Windle, A. H. A Theory of Case II Diffusion. *Polymer (Guildf)*. **1982**, *23* (4), 529–542.
- (225) Ruta, B.; Chushkin, Y.; Monaco, G.; Cipelletti, L.; Pineda, E.; Bruna, P.; Giordano, V. M.; Gonzalez-Silveira, M. Atomic-Scale Relaxation Dynamics and Aging in a Metallic Glass Probed by X-Ray Photon Correlation Spectroscopy. *Phys. Rev. Lett.* **2012**, *109* (16), 1–5. <https://doi.org/10.1103/PhysRevLett.109.165701>.
- (226) Cipelletti, L.; Manley, S.; Ball, R. C.; Weitz, D. A. Universal Aging Features in the Restructuring of Fractal Colloidal Gels. *Phys. Rev. Lett.* **2000**, *84* (10), 2275–2278.

- (227) Cipelletti, L.; Ramos, L.; Manley, S.; Pitard, E.; Weitz, D. A.; Pashkovski, E. E.; Johansson, M. Universal Non-Diffusive Slow Dynamics in Aging Soft Matter. *Faraday Discuss.* **2003**, *123* (1), 237–251.
- (228) Plunkett, M. A.; Claesson, P. M.; Ernstsson, M.; Rutland, M. W. Comparison of the Adsorption of Different Charge Density Polyelectrolytes: A Quartz Crystal Microbalance and X-Ray Photoelectron Spectroscopy Study. *Langmuir* **2003**, *19* (11), 4673–4681.
- (229) Ding, Y.; Ye, X.; Zhang, G. Microcalorimetric Investigation on Aggregation and Dissolution of Poly(N-Isopropylacrylamide) Chains in Water. *Macromolecules* **2005**, *38* (3), 904–908.
- (230) Patra, L.; Toomey, R. Viscoelastic Response of Photo-Cross-Linked Poly(N - Isopropylacrylamide) Coatings by QCM-D. *Langmuir* **2010**, *26* (7), 5202–5207.
- (231) Monteux, C.; Mangeret, R.; Laibe, G.; Freyssingeas, E.; Bergeron, V.; Fuller, G. Shear Surface Rheology of Poly(N-Isopropylacrylamide) Adsorbed Layers at the Air-Water Interface. *Macromolecules* **2006**, *39* (9), 3408–3414.





# Selbstständigkeitserklärung

Ich erkläre, dass ich die vorliegende Arbeit selbständig und unter Verwendung der angegebenen Hilfsmittel, persönlichen Mitteilungen und Quellen angefertigt habe.

---

Ort und Datum

---

Aziz Ben Miled

# Curriculum Vitae

The data on this page has been removed for reasons of personal privacy.

## List of Publications and Posters

A. Ben-Miled, A. Nabiyan, K. Wondraczek, F. H. Schacher, and L. Wondraczek, Controlling Growth of Poly (Triethylene Glycol Acrylate-Co-Spiropyran Acrylate) Copolymer Liquid Films on a Hydrophilic Surface by Light and Temperature, *Polymers (Basel)*. 13, (2021).

A. Ben-Miled, K. Wondraczek, F. H. Schacher, and L. Wondraczek, Kinetic Study of Poly(N-isopropylacrylamide) Glassy Soft Layers (to be submitted)

A. Ben-Miled, K. Wondraczek, F. H. Schacher, and L. Wondraczek, Kinetics of Thin-Thick Transition of Poly(-isopropylacrylamide) Wet Layers (Poster for the online event of the 94th Glastechnische Tagung 05.05.2021)

